NEW STRATEGIES OF DIODE LASER ABSORPTION SENSORS

By

Jian Wang

Report No. TSD-141

August 2001

NEW STRATEGIES OF DIODE LASER ABSORPTION SENSORS

By

Jian Wang

Report No. TSD 141

Work Sponsored By

AFOSR & EPA

High Temperature Gasdynamics Laboratory

Thermoscience Division

Department of Mechanical Engineering

Stanford University

Stanford, California 94305-3032

Abstract

Diode-laser absorption sensors are advantageous because of their non-invasive nature, fast time response, and *in situ* measurement capability. New diode lasers, e.g., GaSb-based longer-wavelength (> 2 μm) lasers and vertical-cavity surface-emitting lasers (VCSELs) have recently emerged. The objective of this thesis is to take advantage of these new diode lasers and develop new gas-sensing strategies.

CO is an important species both as an air pollutant and a key indicator of combustion efficiency. Using (Al)InGaAsSb/GaSb diode lasers operating near 2.3 μm, *in situ* measurements of CO concentration were recorded in both the exhaust (~470 K) and the immediate post-flame zone (1820—1975 K) of an atmospheric-pressure flat-flame burner. Using wavelength-modulation spectroscopy (WMS) techniques, a ~0.1 ppm-m detectivity of CO in the exhaust duct was achieved with a 0.4-s measurement time. For measurements in the immediate post-flame zone, quantitative measurements were obtained at fuel/air equivalence ratios down to 0.83 (366-ppm minimum CO concentration) with only an 11-cm beam path. These results enable many important applications, e.g., ambient air quality monitoring, *in situ* combustion emission monitoring, and engine diagnostics.

As much as 95% of urban CO emission may emanate from vehicle exhaust. The potential of the 2.3-μm CO sensors for on-road remote sensing of vehicle exhaust is examined. A 20-ppm detectivity for typical 5-cm vehicle tailpipes with a ~1.5-kHz detection bandwidth was demonstrated in laboratory experiments, implying the potential to monitor CO emissions from even the cleanest combustion-powered vehicles. Since the temperature profiles of vehicle exhaust are unknown, non-uniform and quickly varying, a new strategy is proposed to eliminate or mitigate the constraint of a known or uniform temperature profile along the light beampath. This new wavelength-multiplexing strategy can be applied to a wide variety of other traditional absorption spectroscopy-based sensors.

Diode laser absorption is for the first time extended to wavelength-scanning high-pressure gas detection by exploiting the fast and broad wavelength tunability of some VCSELs. Demonstration measurements of oxygen in a cell at pressures up to 10 bars are presented. The fast and broad tunability of laser frequency (>30 cm^{-1} at 100 kHz) results from the small thermal time constant associated with small VCSEL cavity volume and the strong resistive heating of distributed Bragg reflector mirrors. This new strategy is potentially more robust in hostile environments than the traditional wavelength-multiplexed strategies, and can be easily extended to other species in high-pressure environments.

Contents

List of Tables

Chapter 4

Chapter 5

Chapter 6

List of Figures

Chapter 1

Chapter 2

Chapter 3

Chapter 4

Chapter 1. *Introduction*

1.1 Motivation and objectives

Compared with some traditional sampling-based gas-sensing instruments, e.g., chemiluminescence-based analyzers, gas-sensing systems based on *in situ* laser absorption spectroscopy are non-invasive, exhibit fast time response, and can yield absolute measurements. Furthermore, the line-of-sight measurement principle inherently gives line-averaged measurements, which can be beneficial in elucidating the overall nature of a gas flow. However, for these systems to be widely deployed in industrial applications, rather than just delicate and expensive laboratory equipment, suitable laser sources are needed.

In contrast to other bulk lasers, semiconductor diode lasers are easy to use, free of maintenance, rugged, and low cost. They also have very low intensity noise, which is essential for achieving high sensitivity. In addition, their wavelength can be directly tuned by changing injection current to scan over the entire lineshape of an absorption transition. Therefore, they are attractive sources for industrial gas-sensing applications. However, not all diode lasers are suitable for high-resolution absorption spectroscopy.

First of all, diode lasers with the specific wavelength that can access the candidate spectroscopic transition of the species to be measured are required for absorption-spectroscopy sensors. To first order, the photon energy emitted by semiconductor diode lasers is equal to the bandgap energy of the semiconductor material. Therefore, to obtain a specific laser wavelength, a semiconductor material with the right bandgap energy needs to be selected. In addition, almost all diode lasers are based on heterostructures, and the lattice constants of semiconductor materials control the heterostructures that can be made. In most cases, to grow one crystalline material on another successfully, their lattice constants need to be very close. Otherwise, the grown material may have a large number of crystalline defects, which will often stop the devices from functioning as desired. Figure 1.1 illustrates the bandgap energies and lattice constants of some III-V semiconductor materials, which have made a significant scientific and technological impact (Woodall 1980; Razeghi 2000). III-V diode lasers can potentially cover a wavelength range from the deep ultraviolet (~200 nm) to the midinfrared (~5 μm). III-V based quantum-cascade (QC) semiconductor lasers (they are not diode lasers, see details in chapter 3) can even extend the wavelength range to bnger than 10 μm. III-nitrides (not shown in the figure 1.1) can potentially

allow a wide wavelength range from ~200 nm to ~600 nm, though only a very small range of 390-410 nm is commercially available. The AlGaAs/GaAs system has a very good lattice match, and is used to make, e.g., 780-nm lasers for compact-disk players and 850-nm lasers for short-distance data communications. The InGaAs/GaAs system can be used to make strained quantum well lasers at 980 nm for pumping erbium-doped amplifiers. The InGaAsP/GaAs system can be used to obtain Al-free laser diodes covering a wide wavelength range of 630-870 nm. One very important application of this system is to make the 808-nm pump lasers for Nd:YAG lasers. InGaAsP/InP and InGaAlAs/InP material systems can cover the 1.3-μm and 1.5-μm bands for fiber optical communications. The above material systems are relatively mature and lasers from these materials are usually very reliable.

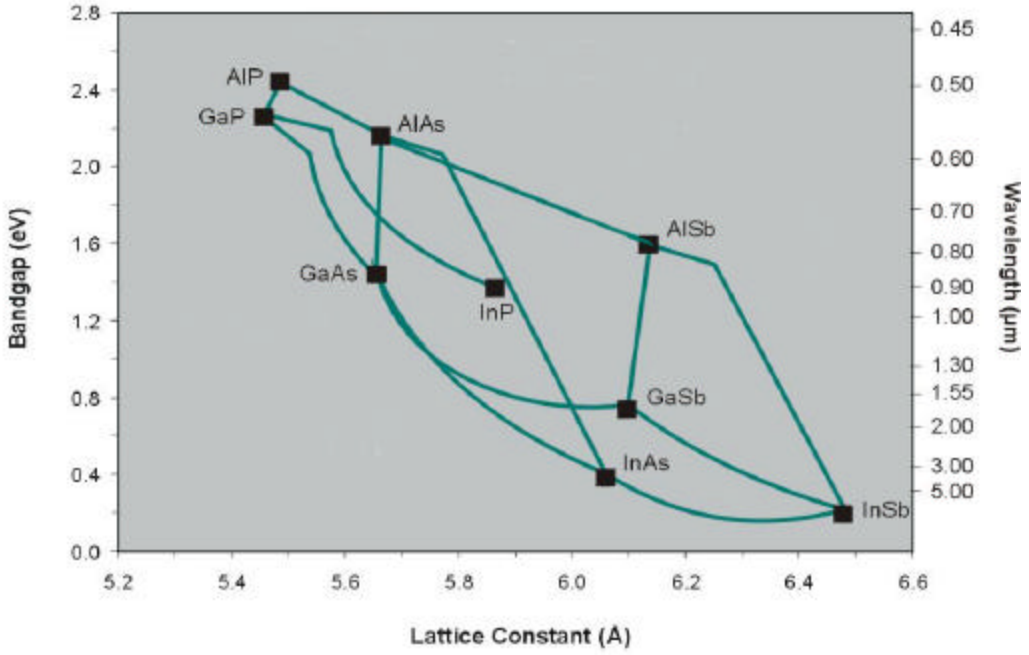

Figure 1.1 Bandgap energy and wavelength vs. lattice constant of some III-V semiconductor compounds and alloys.

To detect trace gases such as nitric oxide (NO) and carbon monoxide (CO), diode lasers which can access their absorption transitions of large linestrength are desired. Typically, electronic transitions and transitions in fundamental or first-overtone vibrational bands have relatively strong linestrength. However, electronic transitions are typically in the ultraviolet (UV) or deep UV regions. Though it is potentially possible to reach the UV region with nitride-based diode lasers, the available wavelength range is currently rather limited (~390-410 nm), and the

extension of the wavelength range to UV or deep UV is still under research and development. On the other hand, the fundamental and first-overtone vibrational transitions are typically in the mid-infrared region. Some of this wavelength region can be reached by the III-V based lasers, e.g., the (Al)InGaAsSb/GaSb lasers (figure 1.1).

CO is a very important species, both as an air pollutant and a good indicator of combustion efficiency (Wang *et al.* 2000a). There is thus a strong need for sensitive *in situ* CO sensors. The 1.5-μm band "telecom" (telecommunication) lasers can access the CO second-overtone band. However, since the linestrength is very weak and there is also relatively large spectral interference from other species, sensitive *in situ* detection is very difficult. Therefore, longer-wavelength lasers which can access the stronger transitions in the first-overtone band at 2.3 μm or the fundamental band at 4.6 μm are desired. Diode lasers based on InGaAsP/InP and InGaAlAs/InP material systems are very difficult to extend beyond 2 μm. However, 2.3-μm (Al)InGaAsSb/GaSb diode lasers have been successfully demonstrated to operate in a continuous-wave mode and around room temperature (Garbuzov *et al.* 1999). These lasers provide the opportunity to detect CO with its first-overtone transitions, and very good *in situ* sensitivity can potentially be achieved. The first part of this thesis has been devoted to exploring this new strategy of CO measurement by taking advantage of new lasers developed by Sarnoff Corporation and Sensors Unlimited Inc.. The lasers obtained were research-grade prototypes and had poor reliability (lifetime ranged from several minutes to several hundred hours for the over 20 lasers tested). Therefore, significant reliability issues must be addressed before these lasers can be employed for long-term in-field applications. Although both of these companies recently decided to focus on the telecom market and quit the smaller gas-sensing business, it is hoped that the high potential for CO measurements at 2.3 μm demonstrated here will serve to stimulate new sources for these lasers.

Vehicle exhaust is the biggest CO source in urban areas. Indeed this accounts for more than ninety percent of total CO emissions in urban areas. Monitoring the emission status of each individual vehicle is one strategy for controlling this biggest emission source. The generally adopted monitoring strategy, i.e., infrequent smog checks, has been identified to have some serious drawbacks. On-road remote sensing is considered to be an important supplemental strategy. Though there is a need for on-road remote sensing, relatively little attention has been paid to this important field by the diode-laser gas-sensing community. It is much more difficult to monitor distributed mobile pollution sources on the road than to monitor stationary sources. The

exhaust from vehicle tailpipes quickly disperses in the air, and thus the gas temperature and composition quickly evolve. Therefore, fast time response is required to yield accurate measurements. In addition, exhaust from different vehicles has different, non-uniform, and unknown concentration and temperature profiles. Absorption spectroscopy is a line-of-sight technology, and quantitative measurements generally require a uniform concentration profile and a known or uniform temperature profile along the light beam path. Therefore, traditional absorption-spectroscopy techniques are not appropriate for this application. Hence, another goal of this thesis is to develop a new strategy to mitigate or eliminate the abovementioned constraints and thus significantly extend the application domain of absorption spectroscopy.

The worldwide market for diode lasers reached the stratospheric level of $6.59 billion in 2000 (figure 1.2). This figure represents a growth rate of 108% over the $3.17 billion reported for 1999, which is the largest increase ever recorded for the diode laser market (Steele 2001). Clearly telecom is by far the largest market, driven by insatiable requirements for bandwidth. Unfortunately, instrumentation and sensing account for the smallest, almost negligible, diode laser market.

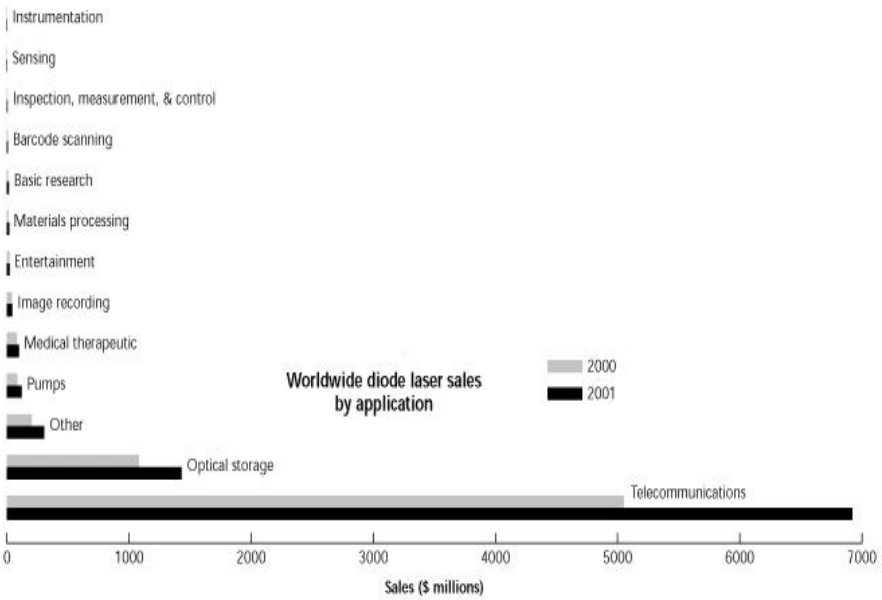

Figure 1.2 Worldwide sales of diode lasers by application. (Laser Focus World, February 2001).

The huge market of telecom lasers keeps attracting diode-laser manufacturers to quit the gas-sensing business and to focus on the telecom market. It is becoming increasingly difficult to find

lasers of non-telecom wavelength, though some companies in Europe and Japan still manufacture diode lasers for spectroscopic applications. On the other hand, the stringent requirements and the strong competition on the telecom lasers continuously drive the advancement of every aspect of laser technology: laser structure, material growth, and processing. This advancement of the laser technology and other aspects of lightwave communication technologies such as fiber-optic technology will eventually benefit the gas-sensing community.

For example, telecom lasers are likely to eventually cover a larger wavelength range to deliver more bandwidth. Traditionally, telecom diode lasers operate in either the 1.3-μm band or the 1.5-μm band for transmission because of the low attenuation of silica-based fiber at these wavelengths. The 1.4-μm band has not been available because of higher attenuation (1dB/km or higher) of the silica-based fiber. However, technology for fiber manufacturing has been significantly improved recently. The water concentration in some fiber, e.g., Lucent Technologies AllWave™ optical fiber, can be made so low that the entire range of 1285 nm to 1625 nm can now be used for laser transmission with reasonably low attenuation. Therefore, telecom-grade lasers will likely be available over this larger wavelength range in the near future to take full advantage of these new fibers. Many important gas species have transitions in this wavelength range, and thus this extension of telecom wavelength range can certainly be valuable to the gas-sensing community.

In addition to the wavelength requirement, diode lasers for gas sensing based on spectroscopic techniques need to operate in single-axial and single-transverse mode. The side-mode suppression ratio (SMSR) usually needs to be better than 20 dB. This typically precludes the use of cheap Fabry-Perot lasers, e.g., those used for data storage or entertainment applications, in long-term in-field gas-sensing applications, because these lasers typically have low SMSR and exhibit mode-hop behavior. More expensive distributive feedback (DFB) and distributive Bragg reflector (DBR) lasers are traditionally used for commercial gas sensors, though FP lasers may be used in laboratory research environments. In the past decade, significant advancement has been made in the technology of vertical-cavity surface-emitting lasers (VCSELs), mainly driven by telecom and interconnection applications. These lasers are inherently low cost due to their good manufacturability and high yield, on-wafer testing capability, low beam divergence and thus easy fiber-pigtailed packaging. Single-axial-mode operation is intrinsically obtained due to VCSELs' extremely short effective cavity length (one to several wavelengths). With careful transverse-

mode control, single-transverse-mode operation can be simultaneously achieved. Therefore, VCSELs can also satisfy the SMSR requirement for gas-sensing applications.

Currently, VCSELs are only commercially available with a very limited wavelength range (~0.7-1 μm). However, many research institutes and companies are actively developing VCSELs in the 1.3-μm and 1.5-μm bands for telecom applications (Coldren *et al*. 2001; Harris 2000; Chang-Hasnain 2000). Once they are commercially available, these cheap and single-mode lasers with low beam divergence will certainly find their applications in and make great impact on the gas-sensing field. Furthermore, electrically-pumped VCSELs operating near 2.2 μm (Baranov *et al*. 1998) and optically-pumped mid-infrared (~2.9 μm) VCSELs (Bewley *et al*. 1999) have been successfully demonstrated with Sb-based materials. However, it may take much longer time for these VCSELs to be of commercial grade due to the significantly less investment compared to that on telecom VCSELs. Finally, because of the small active volume of VCSELs, their thermal load and time constant are significantly smaller than those of edge-emitting lasers. These characteristics enable fast and large wavelength tuning. This special property of VCSELs has been exploited for the first time in this thesis to develop a new wavelength-scanning scheme suited for high-pressure gas sensing.

The overall objective of this thesis is to develop new strategies and to extend the application domains of absorption gas sensing by taking advantage of the new diode lasers which have emerged in the past few years. Specific objectives of this thesis are the following:

1. Investigate the new 2.3-μm Sb-based diode lasers for combustion diagnostics applications. The best transitions that are free from interference and have minimum temperature sensitivity were identified. The linestrength of these transitions were verified with static gas-cell measurements. Then the experiment was conducted in the low-temperature (~470 K) exhaust duct and the immediate post-flame zone (1820-1975 K) of an atmospheric-pressure flat-flame burner.
2. Extend the application of the developed 2.3-μm CO sensor to on-road remote monitoring of vehicle exhaust. Special complications of this application were identified and a new gas sensing approach was proposed to overcome these complications.
3. Develop a wavelength-scanning technique for high-pressure oxygen gas sensing by exploiting the large and fast wavelength tunability of some 760-nm VCSELs. The origin of this large and fast tunability and other laser characteristics of importance to gas sensing were studied.

1.2 Organization of the thesis

The fundamentals of high-resolution absorption spectroscopy are introduced in Chapter 2. Both direct absorption and modulation spectroscopy are discussed. Chapter 3 presents some fundamentals of diode lasers. Characteristics of different laser structures are described, and the basics of laser dynamics relevant to wavelength-modulation spectroscopy are also given. The application of Sb-based 2.3-μm lasers in detecting carbon monoxide is discussed in Chapter 4. The main findings of both exhaust and immediate post-flame zone measurements are presented in detail. Chapter 5 explores the application of diode-laser sensors to on-road vehicle-exhaust sensing. A new temperature- and composition-insensitive technique is proposed to overcome the complication of unknown environment parameters encountered in these applications. Chapter 6 presents the application of 760-nm VCSELs to high-pressure oxygen sensing with the oxygen A-band transitions. Chapter 7 summarizes the thesis and suggests future work. Appendix A provides the physical background and measurement method of diode-laser relative intensity noise (RIN).

Chapter 2. *Semiconductor Laser Absorption Spectroscopy*

Diode-laser absorption spectroscopy advantageously offers *in situ* gas-sensing capability in hostile environments. With its reasonably good sensitivity and relatively simple realization, diode-laser absorption spectroscopy finds widespread industrial applications (Allen 1998). Essentials of quantitative absorption spectroscopy for measuring gas concentration are first introduced. This thesis used two techniques of diode-laser absorption spectroscopy: direct-absorption spectroscopy and modulation spectroscopy. Their essential characteristics will be discussed in the following sections.

2.1 Fundamentals of quantitative absorption spectroscopy

The fractional transmission, $T(\nu)$, of the effectively monochromatic semiconductor laser radiation at frequency ν [cm^{-1}] through a gaseous medium of length L [cm] may be described by the Beer-Lambert relationship:

$$T(\nu) = \left(\frac{I}{I_o} \right)_\nu = \exp\left(-\int_0^L k_n(x)\, dx\right), \tag{2.1}$$

where k_n [cm^{-1}] is the spectral absorption coefficient; I and I_o are the transmitted and incident laser intensities. The spectral absorption coefficient k_n [cm^{-1}] comprising N_j overlapping transitions in a multi-component environment of K species can be expressed as

$$k_\nu = P \sum_{j=1}^{K} X_j \sum_{i=1}^{N_j} S_{i,j}(T)\, \Phi_{i,j}, \tag{2.2}$$

where P [atm] is the total pressure, X_j is the mole fraction of species j, $S_{i,j}$ [cm^{-2} atm^{-1}] and $F_{i,j}$ [cm] are the linestrength and lineshape of a particular transition i of the species j, respectively. The lineshape function $F_{i,j}$ is normalized such that

$$\int_n \Phi_{i,j}(x, \nu)\, d\nu \equiv 1. \tag{2.3}$$

Broadening mechanisms can be classified as either homogeneous or inhomogeneous. Homogeneous broadening mechanisms affect all molecules equally, while inhomogeneous broadening mechanisms affect some subgroups of molecules differently than others. The dominant homogeneous broadening mechanism in this thesis is collisional interactions with other molecules, resulting in a Lorentzian lineshape profile,

$$\ddot{O}_C(\acute{\imath}) = \frac{1}{2p}\frac{\Delta n_C}{(n - n_0 - \Delta n_S)^2 + \left(\frac{\Delta n_C}{2}\right)^2}, \tag{2.4}$$

where Δn_C represents the collision width (FWHM, full width at half the maximum), Δn_S is the collision shift, and n_0 is the linecenter frequency. In the limit of binary collisions the collision width and shift are proportional to pressure at constant temperature and, for multi-component environments, the total collisional linewidth and shift may be obtained by summing the contribution from all components:

$$\Delta n_C = P\sum_j (X_j 2g_j), \tag{2.5}$$

$$\Delta n_S = P\sum_j (X_j d_j), \tag{2.6}$$

where X_j is the mole fraction of component j, γ_j [cm^{-1} atm^{-1}] and δ_j [cm^{-1} atm^{-1}] are the collisional broadening and shift coefficients due to perturbation by the jth component. Both the collisional broadening coefficient and shift coefficient are functions of temperature, and simple power laws may be used to describe these dependences:

$$g_j^T = g_j^{T_0}\left(\frac{T_0}{T}\right)^{n_j}, \tag{2.7}$$

$$d_j^T = d_j^{T_0}\left(\frac{T_0}{T}\right)^{m_j}, \tag{2.8}$$

where T_0 is the reference temperature, n_j and m_j are corresponding temperature exponents. The temperature exponents are weak functions of temperature and are generally smaller for higher temperature ranges.

The collision-caused frequency shift is negligible compared with the typical tuning range of semiconductor diode lasers even at very high pressures. Therefore, if a wavelength-scanning (the wavelength is scanned over the entire transition feature) scheme is used, the frequency shift due to collision has no effect on measuring gas concentrations. However, if there are multiple transitions in the probed spectral range, then the frequency spacings between neighboring transitions at high pressures may be different from their values reported in the literature and databases based on low pressures due to the different shift coefficients of different transitions. Consequently, the relative frequencies of these transitions are usually set as variables to be optimized in the data fitting routine for high-pressure gas sensing.

Theoretically, to calculate the collision linewidth of a transition in an *N*-component environment, we need to know 2*N* spectroscopic data (*N* different broadening coefficients $g_j^{T_0}$, *N* different temperature exponents n_j) and *N*+1 environment parameters (*N* partial pressures of different components and gas temperature *T*). Practically, only parameters of those major components matter, because the contribution of different components is weighted by their mole fractions (Eq. (2.5)). Even so, this sometimes prevents the successful application of modulation spectroscopy, which generally requires accurate knowledge of the transition linewidth at the measurement conditions.

Doppler broadening is the dominant inhomogeneous broadening mechanism and results from the different Doppler frequency shift of each velocity class of the molecular velocity distribution. If the velocity distribution is Maxwellian, the resulting lineshape corresponds to a Gaussian profile,

$$\Phi_D(\nu) = \frac{2}{\Delta\nu_D}\sqrt{\frac{\ln 2}{\pi}}\exp\left\{-4\ln 2\left(\frac{\nu-\nu_0}{\Delta\nu_D}\right)^2\right\}, \tag{2.9}$$

where $\Delta\nu_D$ represents the Doppler width (FWHM), which is calculated using

$$\Delta\nu_D = 7.1623\times 10^{-7}\nu_0(T/M)^{1/2}, \tag{2.10}$$

where ν_0 [cm^{-1}] is the linecenter frequency, *T* [K] is the absolute temperature, and *M* [a.m.u] is the molecular weight of the probed species. In contrast to collision linewidth, we only need to know the gas temperature to calculate Doppler linewidth.

If Doppler and collisional broadening are of similar magnitude, the resulting lineshape can be modeled as a Voigt profile (Varghese and Hanson 1981a), which is a convolution of Lorentzian and Gaussian profiles:

$$\Phi(\nu) = \int_{-\infty}^{+\infty}\Phi_D(u)\Phi_C(\nu-u)du, \tag{2.11}$$

assuming two broadening mechanisms are independent. Defining the Voigt *a* parameter as

$$a_0 = \frac{\sqrt{\ln 2}\Delta\nu_C}{\Delta\nu_D}. \tag{2.12}$$

and a non-dimensional line position *w* as

$$w = \frac{2\sqrt{\ln 2}(\nu-\nu_0-\Delta\nu_S)}{\Delta\nu_D}, \tag{2.13}$$

The Voigt profile can be calculated as

$$\Phi(\nu)=\Phi_D(0)V(a,w), \qquad (2.14)$$

where $\Phi_D(0)$ represents the magnitude of the Doppler profile at linecenter, and V(a,w) is the Voigt function, which can be calculated with many numerical algorithms with different accuracy and efficiency (e.g., Armstrong 1967; Whiting 1968; Drayson 1976; Humlicek 1982; Ouyang and Varghese 1989; Schreier 1992).

The transition linestrength, which reflects the net result of both absorption and stimulated emission, depends on optical transition probability and lower- and upper-state molecular populations. The optical transition probability is a fundamental parameter, dependent only on the wavefunctions of the lower and upper states, and thus is not a function of temperature. However, the lower- and upper-state populations are functions of temperature. Within the work of this thesis, local thermal equilibrium can be safely assumed, and thus the molecular population distribution among different energy states is solely determined by the local gas temperature. At the temperature and pressure ranges encountered in this thesis, population distribution is always in the non-degenerate limit and can be satisfactorily described by the Boltzmann statistics.

In some spectroscopic databases such as HITRAN96 (Rothman *et al*. 1998) linestrength is given in unit of cm/molecule, i.e., on a per molecule basis. Although this is a more fundamental presentation, it is not very convenient to use in the context of gas concentration measurements where pressure or mole fraction rather than molecule number is often used. Therefore, in the gas-sensing community linestrength is typically expressed in a unit of cm^{-2} atm^{-1}, i.e., on a per atmosphere pressure basis. The conversion is

$$\begin{aligned} S(T)[cm^{-2}atm^{-1}] &= S(T)[cm/molecule]\cdot\frac{N[molecule]}{PV[cm^3atm]} \\ &= S(T)[cm/molecule]\cdot\frac{7.34e21}{T[K]}\left[\frac{molecule\cdot K}{cm^3atm}\right]. \end{aligned} \qquad (2.15)$$

The temperature-dependent linestrength [$cm^{-2}atm^{-1}$] can be expressed in terms of known linestrength at a reference temperature T_0:

$$S(T)=S(T_0)\frac{Q(T_0)}{Q(T)}\left(\frac{T_0}{T}\right)\exp\left[-\frac{hcE''}{k}\left(\frac{1}{T}-\frac{1}{T_0}\right)\right]\left[1-\exp\left(\frac{-hc\nu_0}{kT}\right)\right]\left[1-\exp\left(\frac{-hc\nu_0}{kT_0}\right)\right]^{-1} \qquad (2.16)$$

where Q is the molecular partition function, h [J sec] is Planck's constant, c [cm sec^{-1}] is the speed of light, k [J K^{-1}] is Boltzmann's constant, and E'' [cm^{-1}] is the lower-state energy. The

partition function can be obtained using the following polynomial with coefficients listed in some databases, e.g., HITRAN96 (Rothman *et al.* 1998):

$$Q(T) = a + bT + cT^2 + dT^3 . \tag{2.17}$$

If the linestrength is expressed in unit [cm/molecule], then there is no $\frac{T_0}{T}$ term in the temperature-dependence equation (2.16).

2.2 Direct-absorption spectroscopy

Both scanned- and fixed-wavelength direct-absorption techniques have been used in semiconductor-laser gas property sensors (Baer *et al.* 1996). In the fixed-wavelength scheme the laser wavelength is typically fixed at an absorption linecenter. In addition to requiring knowledge of line broadening, the fixed-wavelength scheme suffers other complications, especially in dirty or multi-phase industrial environments. These complications will be discussed in detail in Chapter 6. Unless very high measurement repetition rate is desirable, the scanned-wavelength scheme should be used.

In the scanned-wavelength scheme the laser frequency is tuned over an extended spectral range. From the measured absorption lineshape, fundamental spectroscopic information such as linestrength and pressure broadening coefficient can be inferred. This kind of measurement is usually an indispensable step for verifying or improving the fundamental spectroscopic parameters in the literature or databases, and thereby insuring the proper interpretation of spectrally resolved absorption data, and checking or helping to eliminate the etalon noise due to multiple reflection and scattering from surfaces of optical components. Furthermore, it removes the effect of linewidth on determining gas concentrations by integrating or fitting the obtained entire lineshape, and thus it gives absolute measurements of gas concentration. This is a great advantage, especially for applications such as combustion diagnostics where the composition and the temperature of the probed gas mixture usually vary with time. Finally, by scanning the laser frequency over some finite spectral range, non-resonant attenuation such as aerosol extinction, optical window attenuation and beam steering can be distinguished from resonant gas absorption. This will be further discussed in Chapter 6 in comparison with the fixed-wavelength schemes.

A more convenient equation for direct-absorption measurements may be obtained by integrating Eq. (2.1) over the absorption lineshape function F_{ij}:

$$\int_{\nu} [-\ln(T(\nu))]\, d\nu = \int_0^L P \sum_{j=1}^{K} X_j(x) \sum_{i=1}^{N_j} S_{i,j}(x)\, dx\,, \tag{2.18}$$

where $-\ln(T_\nu)$ is defined as absorbance. The integral of absorbance is referred to as "integrated area" in this thesis. For gas sensing at low or atmospheric pressures, it is sometimes possible to identify a spectral region where only the transition i of species j, whose concentration is to be measured, absorbs by scrutinizing the simulated survey spectra based on available spectroscopic database such as HITRAN96. Then, the task of data reduction is significantly simplified, since Eq. (2.18) is now reduced to

$$\int_{\nu} [-\ln(T(\nu))]\, d\nu = \int_0^L P X_j(x) S_{i,j}(x)\, dx\,. \tag{2.19}$$

The mole fraction of the probed species j, X_j, can be obtained from measurements of the fractional transmission $T(\nu)$ using either Eq. (2.18) or Eq. (2.19) under some assumptions justified by specific gas-sensing applications. Since linestrength is a function of temperature, the temperature profile along the laser beam path is typically required to infer gas concentration. However, in some applications it is difficult or impossible to obtain the temperature profile. A ratio technique to measure gas concentration without knowing the temperature profile will be proposed and discussed in detail in Chapter 5.

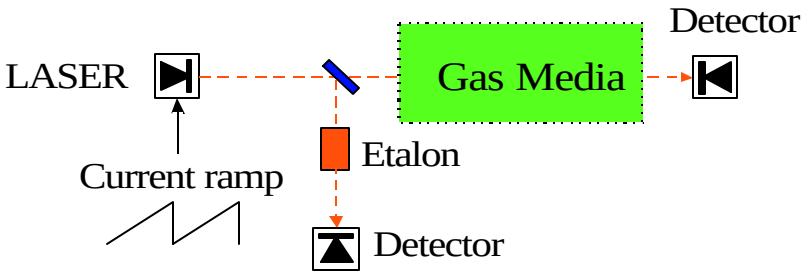

Figure 2.1 Schematic of typical direct-absorption measurements.

The typical procedure for direct-absorption measurements is outlined below. Figure 2.1 illustrates the typical schematic. The laser wavelength is tuned by ramping the injection current. The laser output is separated into two beams. One is directed through the gas medium of interest and then detected to obtain the transmitted laser intensity given in figure 2.2. By fitting the regions without gas absorption to a low-order polynomial, the incident laser intensity can also be obtained (figure 2.2). These two intensities yield the fractional transmission versus time. However, as shown in equation (2.18) or (2.19), the fractional transmission in the frequency domain rather than the time domain as shown in figure 2.2 is required to infer the gas concentration. Therefore, the other laser beam passes through an etalon, and the transmission is

measured (figure 2.3). The peak-to-peak spacing of the etalon trace is constant in the optical frequency domain, i.e., the free spectral range (FSR) of the etalon. This etalon trace, therefore, can yield laser frequency versus time, enabling the absorbance versus frequency (figure 2.4) to be obtained. This trace is fitted with a theoretical transition lineshape to yield the gas concentration.

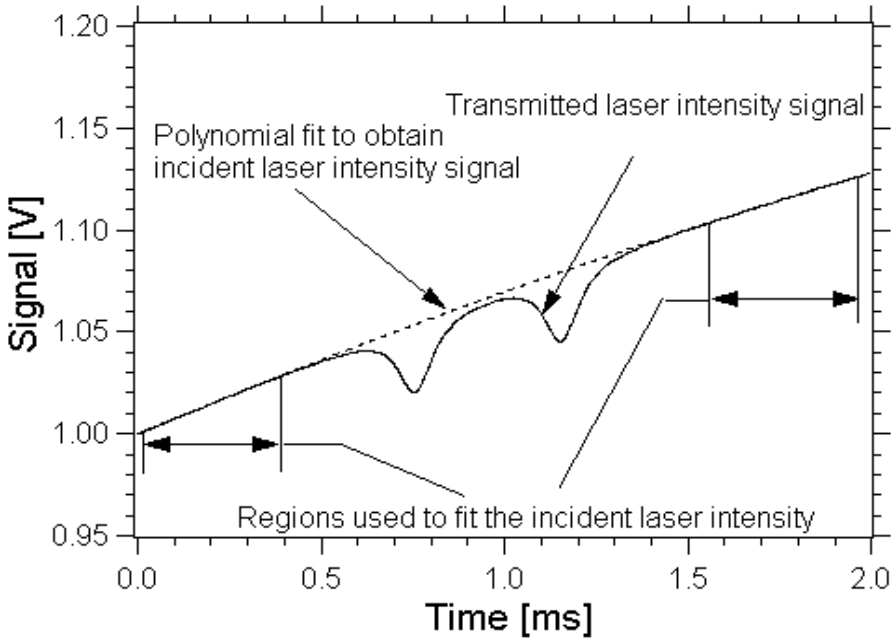

Figure 2.2 Sample signal obtained by passing through a gas medium.

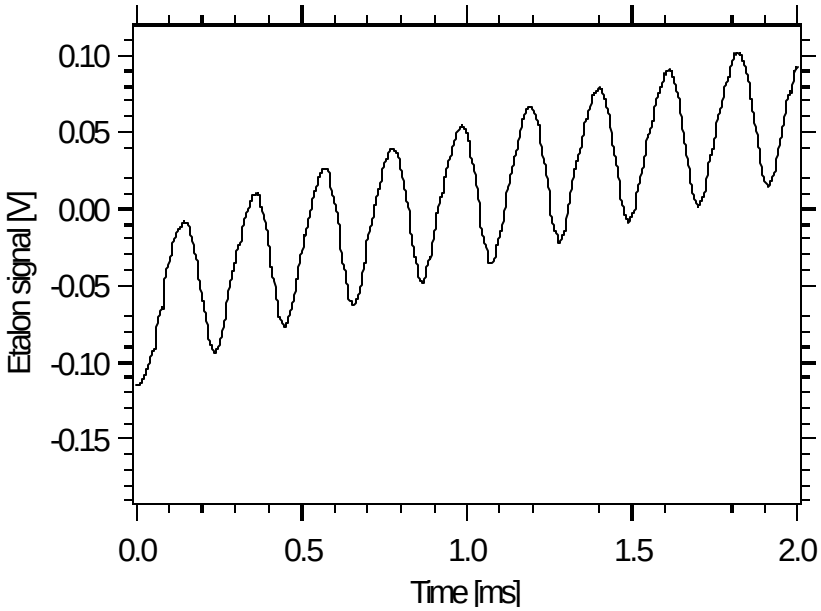

Figure 2.3 Sample etalon signal trace. The peak-to-peak frequency spacing is the free spectral range (FSR) of the etalon.

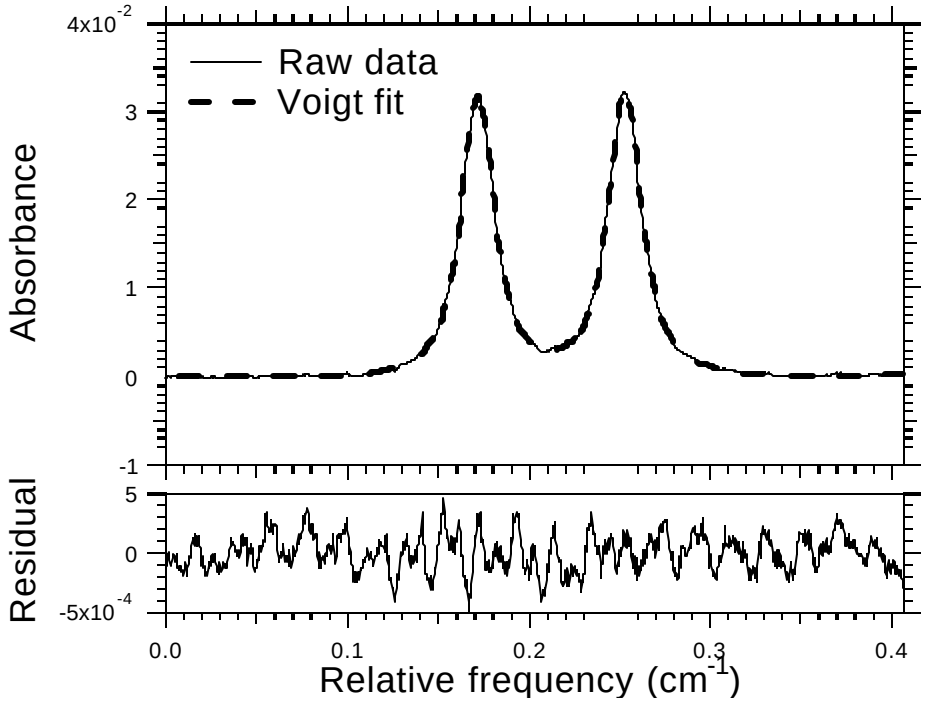

Figure 2.4 A sample absorbance trace (for a pair of absorption lines) in the frequency domain is fitted to a theoretical lineshape to yield the gas concentration.

2.3 Modulation spectroscopy

Modulation spectroscopy significantly reduces noise by shifting detection to higher frequencies where excess laser noise and detector thermal noise are significantly smaller and reducing the detection bandwidth using phase-sensitive detection. Modulation spectroscopy is generally categorized into two groups: wavelength-modulation spectroscopy (WMS) and frequency-modulation spectroscopy (FMS). WMS uses a modulation frequency less than the half-width frequency of the absorption line of interest. Conversely, FMS uses a modulation frequency larger than the transition half-width frequency. With bulk-laser systems such as dye lasers, the optical frequency can be either modulated by dithering the optical length of the laser cavity (Rea *et al.* 1984) or modulated with external electro-optic modulators (Bjorklund 1980). The first scheme with a modulation frequency typically less than 10 kHz is in the WMS regime, while the second scheme with a modulation frequency usually larger than 100 MHz may reach the FMS regime. The laser excess noise (1/*f* noise) typically goes well above MHz and thus for bulk-laser systems the second scheme gives much better sensitivity because of the significantly smaller laser excess noise.

However, semiconductor lasers can be conveniently injection-current modulated from sub-Hz to their relaxation resonance frequency (see section 3.4) that is typically in the 1-10 GHz range. In addition to the modulation of optical frequency, the current modulation induces an intensity modulation. Though this residual intensity modulation causes extra noise, sensitivity comparable to external electro-optic modulation may be obtained. Silver (1992) further found that the sensitivity achievable by modulating the semiconductor lasers at several tens of MHz may be comparable to that achievable at modulation frequencies of several GHz. This "high-frequency" WMS regime is very attractive since it achieves high sensitivity without invoking RF electronics (Reid and Labrie 1981; Silver 1992; Philippe and Hanson 1993). The diode-laser WMS and FMS can be treated with a uniform approach using the electric field of laser radiation (Silver 1992). However, since only WMS was used in this thesis, the traditional mathematical approach using the intensity of laser radiation is used here (some basics of FMS will be discussed later in comparison to a variant of modulation spectroscopy for broadband absorption).

A schematic of a WMS setup is shown in figure 4.11. In addition to scanning the mean frequency $\bar{\nu}$ of a semiconductor laser over the interesting transition by a slow ramp current modulation, a fast sinusoidal dither (f) of the injection current was used to obtain wavelength modulation. Then the instantaneous optical frequency, $\nu(t)$, can be represented by:

$$\nu(t) = \bar{\nu} + a\cos(2\pi ft), \tag{2.20}$$

where a is the maximum small-amplitude excursions of $\nu(t)$ around $\bar{\nu}$. The transmitted laser intensity may be expressed as a Fourier cosine series:

$$I(t) = I_0(t)T(\bar{\nu} + a\cos(2\pi ft)) = I_0(t)\sum_{k=0}^{k=+\infty} H_k(\bar{\nu}, a)\cos(k2\pi ft), \tag{2.21}$$

where $H_k(\bar{\nu}, a)$ is the Fourier coefficient for the fractional transmission $T(\bar{\nu} + a\cos(2\pi ft))$. This transmission signal is sent to either a lock-in amplifier or a mixer to detect the specific harmonic component, which is proportional to $I_0 H_k(\bar{\nu}, a)$, if the residual intensity modulation is neglected.

Commonly, the second-harmonic ($2f$) component is detected due to several reasons. First, the $2f$ scheme can eliminate the effect of the linear component of the laser intensity variation in addition to the elimination of constant dc background. Secondly, most commercial analog lock-in amplifiers can detect the second harmonic component. Finally, the second harmonic signal peaks at the linecenter. Amplitude modulation together with limited detection bandwidth causes a slight asymmetry of $2f$ traces. If this amplitude modulation is neglected, then

$$2f \text{ signal} \propto I_0 H_2(\quad a \quad = I_0 \left(\frac{1}{\quad}\right)_{-p}^{+p} T \quad + a \quad (\text{í} \; u \quad \cos(\quad u)) \text{cos} \qquad (2.22)$$

The fractional transmission T is defined in Eq. (2.1).

Gas concentration is inferred from direct-absorption spectroscopy measurements by integrating the absorbance, i.e., the natural logarithm of the ratio of incident laser intensity and transmitted laser intensity, over the entire lineshape. This ratio procedure removes the uncertainties of laser intensity, electronic signal amplification, etc. However, there is generally no such normalization procedure in the data reduction of WMS techniques. In addition, WMS typically does not use the information content of the entire lineshape to obtain gas concentration. Instead, the signal peak height or peak-to-valley height is used. Therefore, WMS signal is dependent on both the instrument hardware parameters (i.e., laser intensity, signal amplification, and wavelength-modulation amplitude) and the spectroscopic parameters (linestrength and linewidth). A calibration measurement is typically made at a reference condition to eliminate the dependences on the hardware parameters. However, the spectroscopic parameters are dependent on the environmental parameters, i.e., temperature, pressure, and gas composition. Therefore, any deviation of these parameters from the calibration condition needs to be compensated. The compensation for the variation of the linestrength parameter through the temperature variation is straightforward,

$$X_{comp} = X_{meas} \frac{S_{calib}}{S_{real}}, \qquad (2.23)$$

where X_{comp} and X_{meas} are the compensated and measured species concentrations, and S_{real} and S_{calib} are the linestrengths at the temperatures of the real and calibration measurements. However, it is relatively complicated to compensate for the variation of the linewidth. The linewidth variation physically changes the peak absorption and the modulation index (defined by equation (2.27)), and both changes vary WMS signal (see, e.g., equation (2.30)). In this thesis, the absorption lineshape can be assumed to be either Lorentzian or Voigt, with both requiring collisional linewidth information. As discussed in section 2.1, the collisional linewidth depends on both spectroscopic and environmental parameters with many of them likely unknown. This seriously limits the application domain of WMS, and is a significant drawback compared with direct-absorption techniques.

For transitions with a Voigt lineshape, there is no explicit equation for compensating the variation of linewidth, and thus numerical evaluation of equation (2.22) is required. For

transitions with a Lorentzian lineshape, analytical expressions exist for the Fourier coefficients and thus compensation can be easily made. Weak absorption can be generally assumed for WMS measurements, and thus the fractional transmission can be expressed as:

$$T(\nu) \approx 1 - \int_0^L PXS\Phi dx \tag{2.24}$$

where all symbols have the same notation as in equation (2.2). If one further assumes uniform concentration, pressure and temperature profiles along the laser beam path, we have

$$T(\nu) \approx 1 - (XL)PS\Phi . \tag{2.25}$$

XL is sometimes called column density. Defining two dimensionless parameters:

$$x = \frac{\bar{\nu} - \nu_0 - \Delta\nu_s}{\Delta\nu_c / 2}, \tag{2.26}$$

$$m = \frac{a}{\Delta\nu_c / 2}, \tag{2.27}$$

the instantaneous fractional transmission can be expressed as:

$$T(\nu(t)) \approx 1 - (XL)PS\left[\frac{2}{p\Delta\nu_c}\frac{1}{1+(x+m\cos 2\pi ft)^2}\right] \tag{2.28}$$

where m is usually called modulation index in the context of wavelength modulation spectroscopy. The second harmonic Fourier coefficient of the above fractional transmission is then (Reid and Labrie 1981)

$$H_2(x,m) = \frac{2(XL)PS}{p\Delta\nu_c}\left\{\frac{\sqrt{2}}{m^2}\frac{(M+1-x^2)\sqrt{M+\sqrt{M^2+4x^2}}+4x\sqrt{\sqrt{M^2+4x^2}-M}}{\sqrt{M^2+4x^2}}-\frac{4}{m^2}\right\} \quad (x \geq 0) \tag{2.29}$$

where $M = 1 - x^2 + m^2$. This expression is only accurate for $x \geq 0$. However, it gives the full lineshape, since the second harmonic lineshape is an even function of x.

The lineshape function $H_2(x)$ varies with the modulation index (figure 2.5). The lineshape becomes broader when increasing the modulation index. Therefore, different lineshapes can be obtained by setting a different wavelength-modulation amplitude, a. This property adds extra freedom to the WMS compared to the direct-absorption spectroscopy, which has a lineshape function $\Phi(x)$ independent of the hardware setting. The signal peak height achieves the maximum at a modulation index of 2.2 (figure 2.5); therefore, many experiments set the modulation index to a value of approximately 2. However, to reduce the interference from nearby transitions, a smaller modulation index is sometimes preferred for less broadened lineshapes. The

ratio of the peak height to the valley height is also different for different modulation indices, and this property can be used to set a desired modulation index for a specific measurement or to quantify the modulation amplitude a if the linewidth is known. At the linecenter, i.e., at x=0, the term inside the bracket of Eq. (2.29) can be simplified to $\frac{2}{m^2}\left(\frac{2+m^2}{(1+m^2)^{1/2}}-2\right)$. Therefore, if the peak signal height is used to infer gas column density, then we have a much simplified expression:

$$XL \propto \frac{P_{2f}\,\Delta\nu}{I_0\,S}\left[\frac{2}{m^2}\left(\frac{2+m^2}{(1+m^2)^{1/2}}-2\right)\right]^{-1}. \qquad (2.30)$$

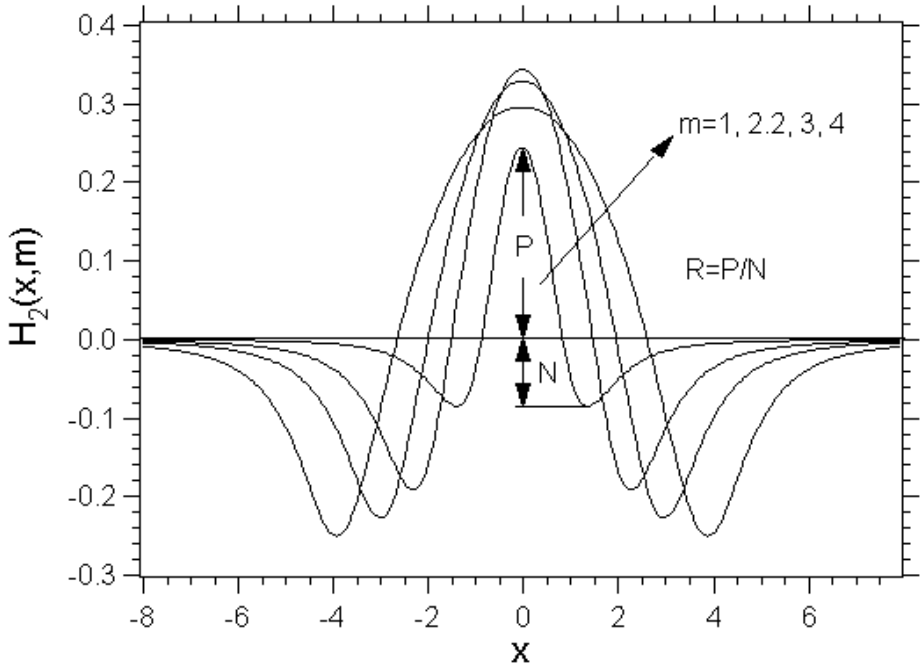

Figure 2.5 Shape of WMS 2f trace with different modulation indices.

The WMS scheme described above is a scanned-mean-frequency scheme, i.e., the laser mean frequency $\bar{n}$ is scanned over the transition lineshape. The advantage of this scheme is that the signal quality can be checked, and interference such as etalon noise level can be determined. However, for real measurements, WMS typically infers gas concentrations from the signal peak height, and thus it is not necessary to scan the laser mean frequency to obtain non-peak information. Instead, the laser mean frequency can be locked to the transition linecenter using the first or third harmonic component of the transmitted signal as a feedback signal to the temperature or current controllers of the laser diode. This fixed-mean-frequency scheme can

achieve much faster measurement repetition rate, since it is limited by the detection bandwidth rather than the scanning period of the laser mean frequency.

Although modulation-spectroscopy techniques yield gas concentrations only from the peak height of the phase-sensitively detected signal, they are inherently much less vulnerable to hostile environments than the wavelength-fixing direct-absorption spectroscopy techniques, because the absorption information is obtained from the variation of attenuation with optical frequency rather than the attenuation itself with the wavelength-fixing direct-absorption spectroscopy. In combustion environments, background emission and attenuation of laser intensity (density-gradient-induced beam steering, scattering and absorption by solid- and liquid-phase aerosols) are potential noise sources and may pose serious challenges to fixed-wavelength direct-absorption measurements. However, modulation-spectroscopy techniques are immune to background emission noise due to their high-frequency phase-sensitive detection and are less sensitive to laser attenuation noise. In cases where background emission noise is small, the "dc" component (which can be easily obtained using a low-pass electronic filter) of the transmission signal may be used to further improve the system robustness:

$$X_{CO,meas} \propto H_2(\tilde{\nu},a)\frac{I_0(1+\delta_{noise})H_2(\tilde{\nu},a)}{I_0(1+\delta_{noise})H_0(\tilde{\nu},a)}=\frac{2f\ \text{signal}}{dc\quad \text{sign}}, \tag{2.31}$$

because $H_0(\tilde{\nu},a)$ is essentially unity for small absorptions; here δ_{noise} represents the combined effects of beam steering and attenuation by aerosols. With this self-compensation capability of the WMS techniques, the effects of light intensity fluctuations (δ_{noise}) can be easily removed.

2.4 Modulation spectroscopy for broadband absorption

Modulation techniques discussed above may be called standard modulation spectroscopy, which is valid only for transitions with linewidth comparable to the obtainable amplitude of the laser wavelength modulation. However, there exists a variant of modulation spectroscopy that can be applied to broadband absorption. The technique was not used in this thesis, but is briefly discussed here, since it significantly broadens the application domain of modulation spectroscopy. Figure 2.6 illustrates the basic idea of this technique. Two lasers are used in this scheme, with one laser "on-line", i.e., its wavelength falls within the wavelength region of the gas

-line," i.e., outside the wavelength region of absorption. The two laser beams are combined together. Both lasers are modulated at the same frequency, but their intensity modulation is 180 degrees out-of-phase. Therefore, their intensities can be described by

$$I_1 = I_{1,0}(1 + M_1 \cos wt), \tag{2.32}$$

and

$$I_2 = I_{2,0}(1 - M_2 \cos wt), \tag{2.33}$$

where M_1 and M_2 are corresponding intensity modulation depths. A beamsplitter splits the combined laser beam into two beams. One (reference beam) directly goes to a detector, while the other (measurement beam) is directed through the gas medium of interest and then to a detector. The intensities of the reference beam and the measurement beam are

$$I_{ref} = a\{I_{1,0} + I_{2,0} + (I_{1,0}M_1 - I_{2,0}M_2)\cos wt\}, \tag{2.34}$$

and

$$I_{meas} = b\{I_{1,0}T_{gas}T_{1,nongas} + I_{2,0}T_{2,nongas} + (I_{1,0}M_1T_{gas}T_{1,nongas} - I_{2,0}M_2T_{2,nongas})\cos wt\}, \tag{2.35}$$

where constants a and b describe the splitting factors of the beamsplitter, T_{gas} is the fractional transmission at the wavelength l_1 due to the gas medium, and $T_{1,nongas}$ and $T_{2,nongas}$ consider the non-gas attenuation such as optical window transmission at wavelengths l_1 and l_2 correspondingly.

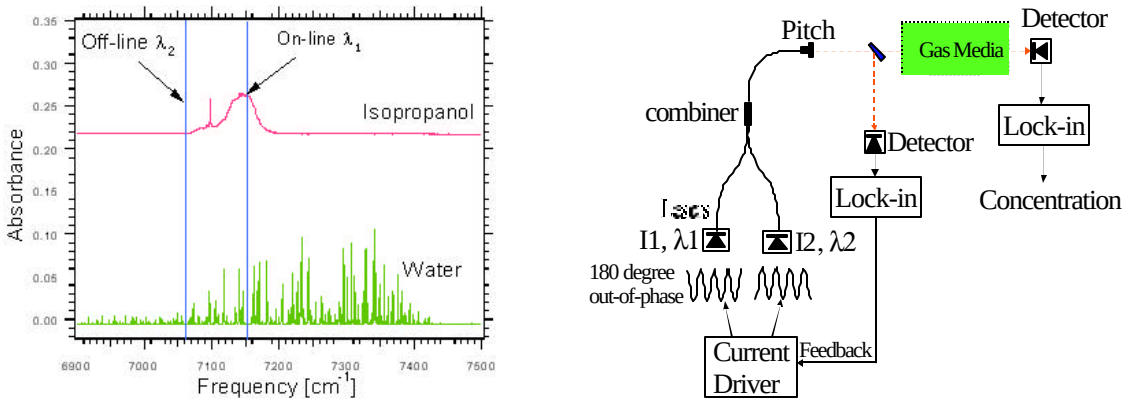

Figure 2.6 A modulation-spectroscopy technique for detecting species, e.g., isopropanol, with broadband absorption. Wavelengths of "on-line" and "off-line" lasers are selected to avoid spectral interference from other species, e.g., water in the left diagram.

Phase-sensitive detection at an angular frequency w is used to extract the signals of both channels, and the final obtained signals for the reference and measurement channels are

$$S_{ref} \propto I_{1,0}M_1 - I_{2,0}M_2, \tag{2.36}$$

and

$$S_{meas} \propto I_{1,0} M_1 T_{gas} T_{1,nongas} - I_{2,0} M_2 T_{2,nongas} , \tag{2.37}$$

correspondingly. S_{ref} is used as the negative feedback signal to actively control the intensities of the two lasers to achieve $S_{ref} \approx 0$, i.e., $I_{1,0} M_1 \approx I_{2,0} M_2$. The effect of laser noise on detection sensitivity is suppressed through this feedback control. The signal of the measurement beam is then

$$S_{meas} \propto I_{1,0} M_1 (T_{gas} T_{1,nongas} - T_{2,nongas}) , \tag{2.38}$$

which is solely due to the attenuation difference in the measurement beam path at the two different laser wavelengths. If this attenuation difference is dominated by the gas absorption or the non-gas attenuation is same at the two different wavelengths, relation (2.38) can be simplified to

$$S_{meas} \propto \left[T_{gas} - 1 \right] \approx k_{l1} L . \tag{2.39}$$

Therefore, the gas concentration can be inferred from the signal of the measurement channel. Like standard modulation spectroscopy, this scheme also requires calibration. The off-line laser offers the capability to monitor or compensate for non-gas attenuation. This scheme exploits the laser intensity modulation rather than the wavelength modulation exploited in standard modulation spectroscopy.

The modulation frequency should be chosen based on the required time response (or detection bandwidth) and detection sensitivity. To filter out the harmonic component effectively in the phase-sensitive detection, the modulation frequency should be much (e.g., an order of magnitude) larger than the required detection bandwidth. Higher modulation frequency also can achieve higher sensitivity by reducing the laser excess noise and the detector thermal noise. One advantage of using laser sources rather than conventional broadband light sources is that the potential spectral interference from other species can be avoided by selecting appropriate laser wavelengths as shown in the left diagram of figure 2.6. Finally, this scheme also has the advantage of high suppression of background noise due to the phase-sensitive detection. However, since it is basically a fixed-wavelength method, this scheme may suffer from the complication of wavelength-dependent non-gas attenuation, i.e., $T_{1,nongas}$ may be different from $T_{2,nongas}$ (see details in chapter 6). This complication is particularly troublesome if the attenuation difference is varying over time.

It helps to understand both the above two-laser detection scheme and the standard frequency modulation spectroscopy (FMS) by making a comparison between them. For the FMS, the laser is modulated at a high frequency w ($w > \Delta n\,(HWHM)$), and the instantaneous electrical field of the laser output can be described as:

$$E(t) = E_0\left[1 + M\sin(wt + y)\right]\exp\left[iw_0 t + ib\sin(wt)\right] \tag{2.40}$$

where w is the modulation frequency, w_0 is the optical frequency, M is the amplitude modulation depth, b describes the phase modulation (or frequency modulation) and is usually called as frequency modulation depth, and y gives the phase difference between the amplitude and phase modulation. By substituting the following two equations:

$$M\sin(wt + y) = \frac{M}{2i}\left[\exp\left(i(wt + y)\right) - \exp\left(-i(wt + y)\right)\right], \tag{2.41}$$

$$\exp\left[ib\sin(wt)\right] = \sum_{l=-\infty}^{\infty} J_l(b)\exp(ilwt), \tag{2.42}$$

equation (2.40) is transformed to

$$E(t) = E_0\exp(iw_0 t)\sum_{l=-\infty}^{\infty} r_l\exp(ilwt), \tag{2.43}$$

where

$$r_l = \frac{M}{2i}\exp(iy)J_{l-1}(b) + J_l(b) + \frac{-M}{2i}\exp(-iy)J_{l+1}(b). \tag{2.44}$$

$J_l(b)$ is the lth order Bessel function. For FMS, b is typically much less than unity, and thus the only significant components in the expansion are the carrier (l = 0) and the first-order sideband pair (l = ±1), as illustrated in figure 2.7. If the amplitude modulation effect is negligible, i.e., $M \approx 0$, then we have

$$r_1 = J_1(b) = -J_{-1}(b) = -r_{-1}, \tag{2.45}$$

i.e., the two sidebands have the same amplitude, but they are 180 degrees out of phase. The laser electric field is then approximated as

$$E(t) = E_0\exp(iw_0 t)\left\{J_0(b) + J_1(b)\left[\exp(iwt) - \exp(-iwt)\right]\right\}. \tag{2.46}$$

Like WMS, FMS has fixed wavelength and scanned wavelength schemes. For the fixed wavelength scheme, the laser wavelength is adjusted such that one side band is near the absorption peak, i.e., subject to maximum absorption, while the other side band is located for negligible absorption (figure 2.7). We should recognize now that this strategy of sensitive detection of narrow absorption feature is in essence very similar to that used in the two-laser

scheme of modulation spectroscopy for detecting broadband absorption. The mismatch of the influence of absorption feature to the two sidebands is used to detect the narrow absorption feature with FMS, while the mismatch of the attenuation by two lasers is used for detecting the broadband absorption. However, since the two sidebands are obtained by modulating one laser source for FMS, their amplitudes are inherently balanced (small misbalance may exist due to the residual amplitude modulation, see equation (2.44)), and thus the negative feedback control loop is not required.

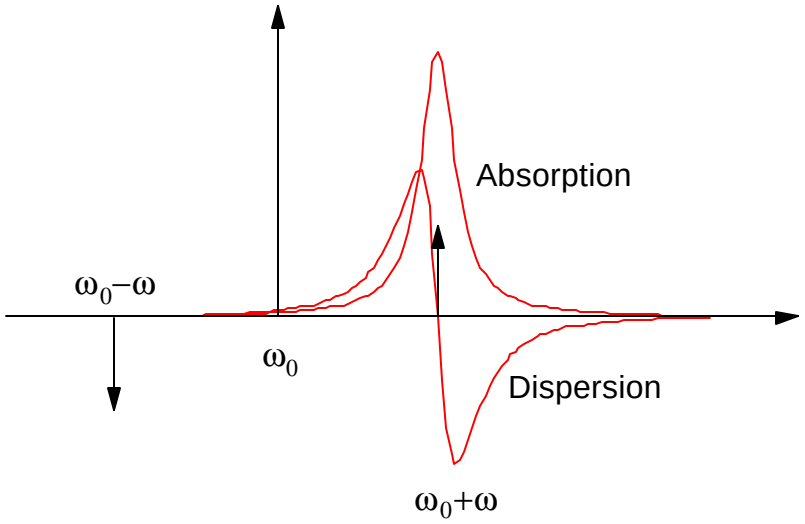

Figure 2.7 Spectral view of the standard frequency modulation spectroscopy.

For the two-laser scheme of modulation spectroscopy, two lasers are not coherent (because the difference between the optical frequencies of two lasers is much larger than the modulation frequency) and the laser intensities rather than the laser electric fields are used to analyze and interpret the measurements. However, the carrier and the two sidebands are coherent for FMS; therefore, electric field rather than intensity is used in the above derivation. When this laser beam passes through a gas medium, the transmitted laser electric field is

$$E(t)=E_0\exp(iw_0t)\left\{T_0J_0(b)+J_1(b)\left[T_1\exp(iwt)-T_{-1}\exp(-iwt)\right]\right\} \tag{2.47}$$

where $T_l=\exp(-d_l-j_l)$, $d_l=k_{w_0+lw}L/2$, and $j_l=(w_0+lw)n_lL/c$ $(l=0,\pm1)$. k_{w_0+lw} is the spectral absorption coefficient at the optical frequency w_0+lw. L is the length of the gas medium, c is the light speed, and n_l is the refraction index at the frequency w_0+lw (refractive

index is strongly frequency-dependent near the absorption feature, see the dispersion curve in figure 2.7). d_l describes the amplitude attenuation due to the gas absorption, while j_l describes the phase delay through the gas medium. The transmitted laser intensity is proportional to the modular square of the transmitted electric field, we obtain

$$I(t) \propto \left|E(t)\right|^2 = E_0^2 \sum_{l=-1}^{1} \sum_{m=-1}^{1} T_l T_m^* J_l(b) J_m(b) \exp\left[i(l-m)wt\right]. \tag{2.48}$$

We may make some approximations before going further. Since $b << 1$ for FMS typically, we have $J_0(b) \approx 1$ and $J_{\pm 1}(b) = \pm b/2$. Furthermore, since FMS is typically used for trace-gas detection, $|d_0 - d_1|$, $|d_0 - d_{-1}|$, $|j_0 - j_1|$, and $|j_0 - j_{-1}|$ are much smaller than unity. With these approximations, equation (2.48) can be simplified to

$$I(t) \propto [1 + (d_{-1} - d_1) b \cos(wt) + (j_1 + j_{-1} - 2j_0) b \sin(wt)] \tag{2.49}$$

The non-DC terms (usually called beat signal) arise from a heterodyning of the carrier with sidebands in equation (2.48) (the beat signal between the two sidebands is negligible), and thus their strengths are proportional to the geometric mean of the intensity of each side sideband and the carrier. Finally the beat signal is measured by the phase-sensitive detection at the modulation frequency to infer the information of the absorption feature.

Note that the in-phase ($\cos wt$) component of the beat signal is proportional to the difference in loss experienced by the two sidebands, whereas the quadrature ($\sin wt$) component is proportional to the difference between the phase shift experienced by the carrier and the average of the phase shifts experienced by the sidebands. Therefore, not only the absorption but also the dispersion information may be obtained. This unique feature of FMS results from the coherent nature of the laser carrier and sidebands. Absorption features are detected from the mismatch of the change of the electric fields of the laser carrier and sidebands rather than the mismatch of the change of the intensities as in the two-laser scheme.

Chapter 3. *Semiconductor Diode Laser Fundamentals*

Single-mode, room-temperature, continuous-wave semiconductor diode lasers are ideal tunable light sources for gas sensing systems based on high-resolution absorption spectroscopy. This chapter first introduces the basic principles of semiconductor diode lasers, and then describes some representative laser structures including Fabry-Perot (FP), distributed feedback (DFB), distributed Bragg reflector (DBR), and vertical-cavity surface-emitting lasers (VCSELs). Because diode lasers are modulated to implement wavelength-modulation spectroscopy in this thesis, some basics of laser dynamics are presented. Finally, the 2.3-μm (Al)InGaAsSb/GaSb Fabry-Perot diode lasers used in this thesis for CO measurements is discussed.

3.1 Achieving gain in semiconductor diode lasers

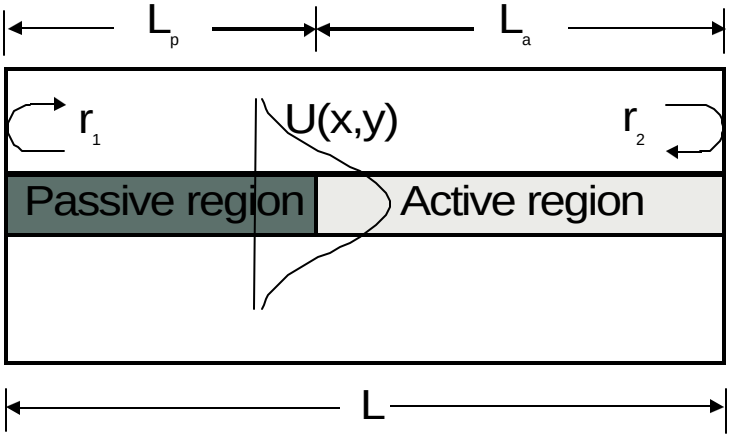

Figure 3.1 A generic edge-emitting laser cavity cross section showing active and passive sections and the guided mode profile.

Figure 3.1 shows the cross section of a generic edge-emitting semiconductor diode laser. It consists of a passive section of length L_p and an active section of length L_a. For simplicity, it is assumed that there is no impedance discontinuity at the interface of the passive and the active regions. In order for a mode of the laser to reach threshold, the gain in the active section must be increased to the point where all the propagation and mirror losses are compensated, so that the electric field exactly replicates itself after one round-trip in the laser cavity. Mathematically, it can be expressed as:

$$r_1 r_2 \exp\left[\left(\Gamma_{xy} g_{th} - \alpha_a\right) L_a\right] \exp\left(-\alpha_p L_p\right) = 1, \tag{3.1}$$

where r_1 and r_2 are amplitude reflection coefficients of two end mirrors, Γ_{xy} is the transverse confinement factor considering the overlapping of the optical field and the active layer, g_{th} is the required threshold gain of the active layer, α_a and α_p are the loss factors in the active section and passive section, and L_a and L_p are the corresponding section lengths. The remainder of this section will introduce how to achieve gain in semiconductor diode lasers.

As atoms are brought together to form semiconductor crystals, the original discrete atomic energy levels form into energy bands. At zero K, the highest energy band with electrons is called the valence band, and the next higher energy band is called the conduction band. The valence band and conduction band are involved in the photon-atom interaction. Semiconductor diode lasers typically use direct-bandgap semiconductors, i.e., semiconductors with the lowest minimum of conduction band directly above the highest maximum of valence band. The energy difference between these two energy extremes is defined as the bandgap of this semiconductor material. From the Bloch theorem, all of the information about this band structure can be described by that in the first Brillouin zone. Due to the usually small number of carriers in semiconductors compared with the number of host atoms, these carriers typically locate only near the Brillouin zone center. Around the Brillouin zone center, it is possible to approximate the shape of the *E-K* extrema (left diagram of figure 3.4) by parabolas. Then the concept of effective masses of electrons and holes can be introduced to simplify the description of carriers. With this simplification, though the electrons and holes in semiconductors are subject to the periodic potential of the semiconductor crystal lattice, near the Brillouin zone center they can be simply described as if they move in free space with their effective masses. The results of the classical "particle in a box" model can then be used.

Figure 3.2 (a) sketches the band diagram of a homojunction diode at equilibrium. The electrons and holes are fermions, and they are subject to the Pauli-exclusion principle. Therefore, the distribution of these carriers among available states is described by the Fermi-Dirac distribution. The Fermi level (i.e., chemical potential in the context of semiconductor physics) of the diode is constant at equilibrium. Like other lasers, to achieve gain, a highly nonequilibrium condition, generally known as a population inversion, needs to be established. This is achieved by injecting carriers into the P-N junction under forward bias (figure 3.2 (b)). Under forward bias, the two

carrier pools are no longer under thermal equilibrium between each other, and thus the concept of Fermi level is meaningless. However, the distribution of electrons among different energy states can still be approximated as under thermal equilibrium, and so can the hole distribution, if two different quasi-Fermi levels are introduced to separately describe these two carrier pools:

$$f_1 = \frac{1}{\exp\left[\left(E_1 - E_{Fh}\right)/kT\right]}, \tag{3.2}$$

and

$$f_2 = \frac{1}{\exp\left[\left(E_2 - E_{Fe}\right)/kT\right]}, \tag{3.3}$$

where E_{Fh} and E_{Fe} are the quasi-Fermi levels for holes in the valence band and electrons in the conduction band. Almost all modern semiconductor lasers are based on heterostructure to better confine the injected carriers and photons, and usually the active regions consist of quantum-well structure. However, the basic idea is still the same as in the homojunction case: achieving population inversion by injecting carriers into the laser active region. Lasers with double heterostructure will be discussed in the next section. The remaining of this section discusses the exact meaning of population inversion, i.e., the condition at which optical gain rather than absorption is achieved, in semiconductor lasers.

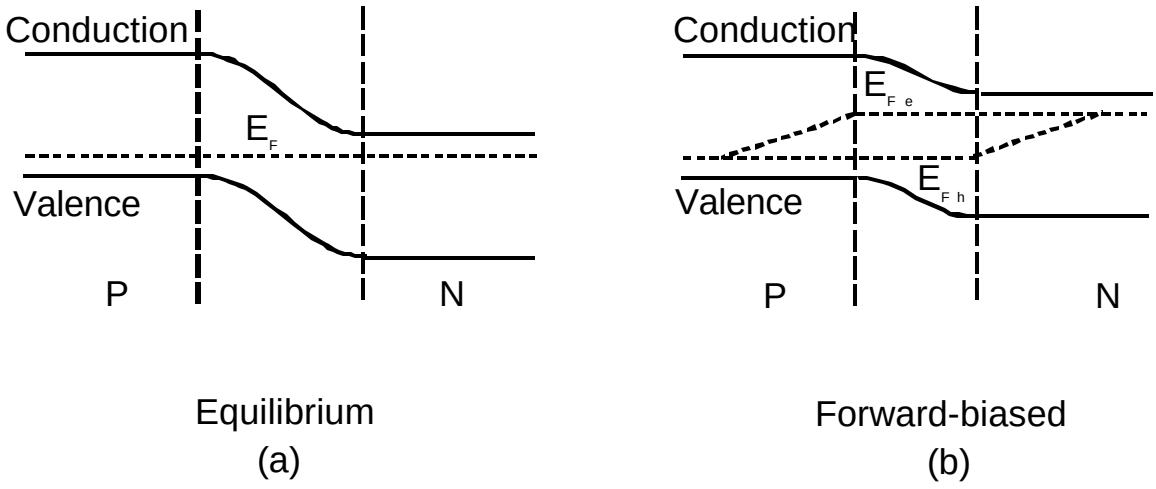

Figure 3.2 Illustration of the band edges of a homojunction diode (a) at equilibrium and (b) under forward bias. (b) shows that the electron and hole quasi-Fermi levels E_{Fh} and E_{Fe} approximately continue into the depletion region and decrease into the N and P regions.

Figure 3.3 sketches band-to-band stimulated transitions. The left diagram shows the stimulated absorption, i.e., one electron at state 1 in the valence band absorbs one photon and is elevated to some state 2 in the conduction band. In the right diagram, the incoming photon stimulates the electron to liberate its energy in the form of a new photon, lowering it from state 2 in the conduction band to state 1 in the valence band. Like other lasers, in order to achieve gain, the stimulated emission rate R_{21} needs to be larger than the stimulated absorption rate R_{12}. For both processes, conservation of momentum and energy need to be satisfied. Since the momentum of photons is very small compared with the electron momentum $\hbar\vec{k}$, the conservation of momentum requires $\vec{k}_1 \approx \vec{k}_2$. The left diagram of figure 3.4 illustrates the requirements for energy and momentum conservation. It shows that for specific photon energy only those energy states in the annuli are involved in optical transitions.

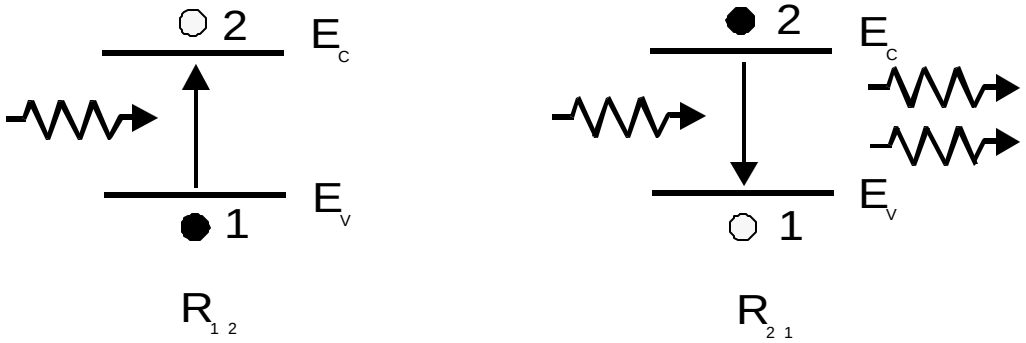

Figure 3.3 Band-to-band stimulated absorption and emission. Black dots represent electrons, while gray dots represent holes.

For both stimulated processes to happen, there must exist a state pair of a filled state in one annulus and a vacant state in the other annulus. Assuming the states in one annulus is full, and the states in the other annulus is entirely vacant, based on the first-order time-dependent Schrodinger equation, the transition rate from the full annulus to the vacant annulus per unit active volume can be found to be:

$$R_r = \frac{2\pi}{\hbar}\left|H'_{21}\right|^2 \rho_f(E_{21})\Big|_{E_{21}=\hbar\omega}, \tag{3.4}$$

where $\rho_f(E_{21})$ is the reduced density of states considering the requirement of momentum conservation, and H'_{21} is the

$$H'_{21} \equiv \langle \psi_2 | H'(r) | \psi_1 \rangle = \int_V \psi_2^* H'(r) \psi_1 d^3 r . \tag{3.5}$$

Here ψ_2 and ψ_1 are corresponding wavefunctions of state 2 and state 1. $H'(r)$ is the spatial part of the perturbation to the Hamiltonian due to the interaction of photons and carriers. This is known as the Fermi's Golden Rule (No. 2).

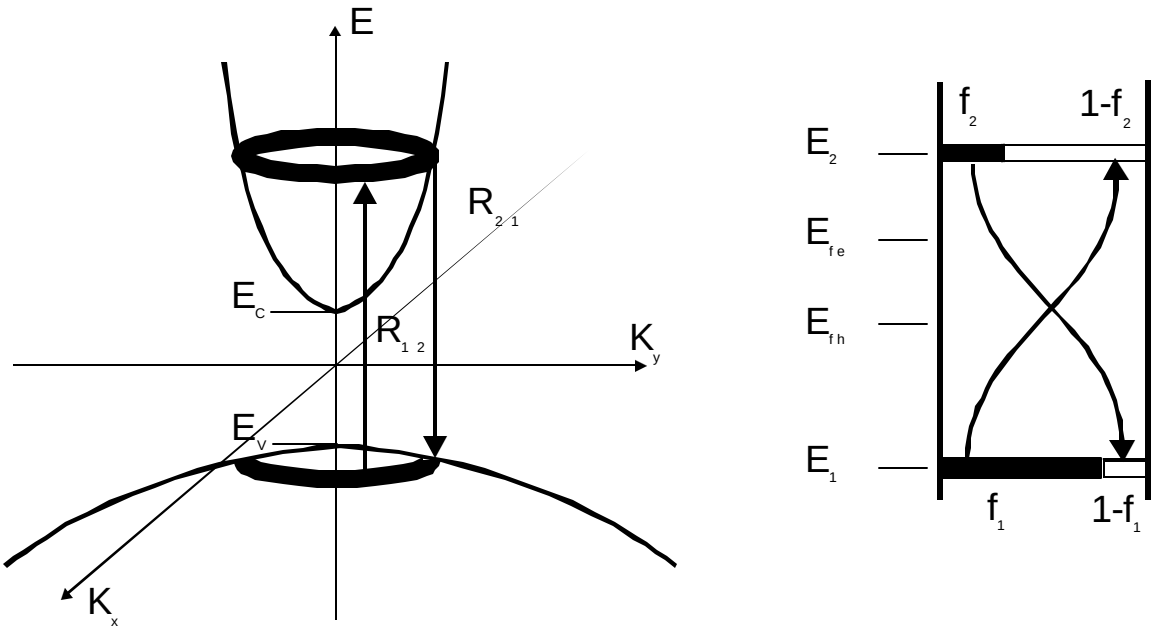

Figure 3.4 State pairs which interact with photons with energy E_{21} (E_2-E_1) for stimulated transitions. Requirement of energy and momentum conservations reduces the state of pairs to the annuli shown in the left E-K (energy vs. momentum) plot. For bulk lasers, the K vector space is three-dimensional, this two-dimensional representation of the K vector space can be regarded as a simplified presentation. For quantum-well lasers, the K vector space is two-dimensional, and the above E-K plot represents one set of subbands. The right plot shows the electron occupation probabilities f_1 and f_2 in the valence band and the conduction band respectively. The finite width of energy states expresses the finite energy uncertainty due to relaxation processes limiting carrier lifetime.

However, at real conditions, both bands are partially filled, as illustrated in the right plot of figure 3.4. In this case, the stimulated absorption and emission rate can be expressed as:

$$R_{12} = R_r [\, f_1 (1 - f_2) \,], \tag{3.6}$$

and

$$R_{21} = R_r [\, f_2(1 - f_1)]. \tag{3.7}$$

Then the net stimulated emission rate is

$$R_{st} = R_{21} - R_{12} = R_r (f_2 - f_1). \tag{3.8}$$

To achieve gain, the net stimulated emission rate needs to be positive. This requires the occupancy probability in state 2, f_2, to be larger than that in state 1, f_1. This is the meaning of population inversion in semiconductor diode lasers. This meaning is similar to that of lasers with discrete energy levels 2 and 1, e.g., He-Ne lasers, where the population inversion means

$$\frac{N_2}{g_2} > \frac{N_1}{g_1}. \tag{3.9}$$

N_2 and N_1 are the number densities of gain species in the levels 2 and 1. g_2 and g_1 are corresponding degeneracy of both levels. Both sides of Eq. (3.9) can also be considered as occupancy factors, though they may be larger than one since these gain species may not be fermions.

If taking the ratio of these stimulated transition rates, we have

$$\frac{R_{21}}{R_{12}} = \frac{f_2(1 - f_1)}{f_1(1 - f_2)} = \exp\left[(\Delta E_F - E_{21})/kT\right], \tag{3.10}$$

where $\Delta E_F = E_{Fe} - E_{Fh}$ is the separation of quasi-Fermi levels. Therefore, the net stimulated emission rate becomes positive only when the quasi-Fermi level separation is greater than the photon energy of interest. Since the photon energy must at least be equal to the bandgap energy E_g, ΔE_F must be larger than E_g to achieve gain. Large amounts of carriers need to be injected into the junction depletion region to achieve this highly nonequilibrium condition.

It is worthwhile to mention another class of semiconductor lasers: quantum-cascade (QC) lasers. Superlattice (closely-coupled quantum wells) based type-I QC semiconductor lasers have been successfully developed in the wavelength range of 3.4-13 μm (Capasso *et al.* 1999) based on the InGaAlAs/InP material system. The mature growth and processing technologies of this material system ensure the high reliability of these lasers. Absorption gas sensors based on these devices have also been successfully demonstrated (Namjou *et al.* 1998; Paldus *et al.* 1999). These lasers are different from normal diode lasers in a fundamental way: carrier population inversion happens between the discrete excited states of the conduction band rather than between conduction and valence bands (Faist *et al.*1994). Figure 3.5 shows one period of a QC laser, and

the carrier population inversion is established between energy levels 3 and 2. Many periods of this structure are cascaded in a QC laser, and photons are emitted at each period when electrons are streaming down this potential staircase. No longer limited by the bandgap of the intrinsic materials, these QC lasers rely on quantum size effects to produce arbitrary emission wavelength. They are unipolar devices, and some designs even allow lasing operation under both positive and negative bias (Gmachl *et al.* 1999). Therefore, they are not diode lasers at all. Since only electrons are involved in the lasing and there are no p-type materials in the laser structure, the intersubband transitions of the valence band and the Auger recombination effects, which give the very poor temperature behavior of normal mid-infrared diode lasers, are eliminated.

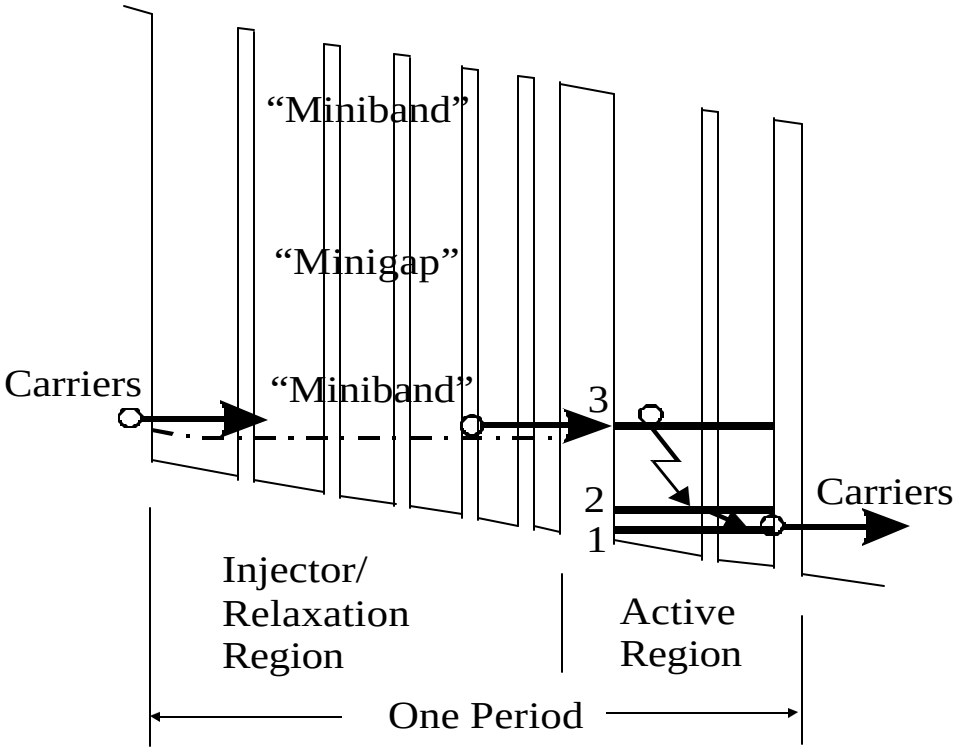

Figure 3.5 Conduction-band structure of one period of a quantum-cascade laser.

Instead of the 2-level system shown in figure 3.3 or figure 3.4 with normal diode lasers, QC lasers are 4-level laser systems, with the upper and lower levels being the energy levels of the closely-coupled quantum wells. The maximum lifetime of electrons (~1 ps) in the upper level is limited by the optical phonon emission rate. Due to this high non-radiative transition rate, the threshold current is very large (e.g., 2 A). In addition, to increase the differential quantum efficiency, many periods of the lasing structure are cascaded. This leads to a very high compliance voltage (e.g., 7 V). This combination of high current and large voltage leads to very

large heat generation. However, these lasers have been demonstrated to operate in a pulsed mode up to ~330 K. These near-room-temperature pulsed lasers show great promise in developing portable trace-gas sensors.

3.2 Double heterostructure and quantum wells

The concept of heterojuction-injection diode laser was originally proposed to obtain lasing in indirect-gap semiconductors or improve efficiency in direct-gap ones by H. Kroemer (Kroemer 1963) only one year after the demonstration of diode lasers (H. Kroemer won the Nobel Prize of Physics in 2000 mainly because of his seminal work on heterojunction devices). Almost all modern diode lasers are based on double heterostructures (DH). Figure 3.6 shows a schematic of the material structure, corresponding energy band diagram, transverse refractive index profile, and electric field of a PIN double-heterostructure laser diode. The thin intrinsic active layer is sandwiched between P- and N-type cladding layers. The active layer has a smaller bandgap energy than those of the cladding layers. This formed potential well traps both electrons and holes injected from N- and P-regions. Therefore, carrier number density in the active layer is significantly enhanced. This increased number density in turn leads to higher gain. In addition, the refractive index of the active layer is larger than those of the cladding layers. This refractive index profile forms a waveguide structure and confines photons within this waveguide. Finally, the photons in the cladding layer will have very low attenuation since the photon energy ($\approx$ bandgap energy of the active layer) is smaller than the bandgap energy of the cladding layer. Therefore, DH structure provides an ideal laser structure.

To reduce threshold current density further, a quantum-well laser structure is usually used. Figure 3.7 diagrams a transverse band structure for a single-quantum-well laser. In quantum-well lasers, quantum wells have the lowest energy, and thus carriers diffuse to and are confined in the quantum wells. Due to the small dimension (e.g., 8-nm thickness) of quantum wells, the current density required to achieve certain amount of carrier number density is much lower than that required for DH bulk lasers. In addition, the low-dimensional quantum effect changes the distribution of the density of states, and a larger amount of density of states can be achieved near the band edges compared with that of bulk lasers. This in turn leads to larger reduced density of states near the band edges. Therefore, from Eq. (3.4), the transition rate near the band edges will be enhanced. This means that a much smaller carrier number density is required to achieve reasonable gain, since it is not necessary to fill carriers to high energy levels. In summary, the small volume and low dimensionality (2-dimensional rather than 3-dimensional) of quantum-well

lasers can reduce threshold current density significantly. However, the thickness of quantum wells is much smaller than the light wavelength so that the waveguide formed by quantum wells cannot confine photon efficiently. Therefore, a double heterostructure is usually used to separately confine photons (figure 3.7).

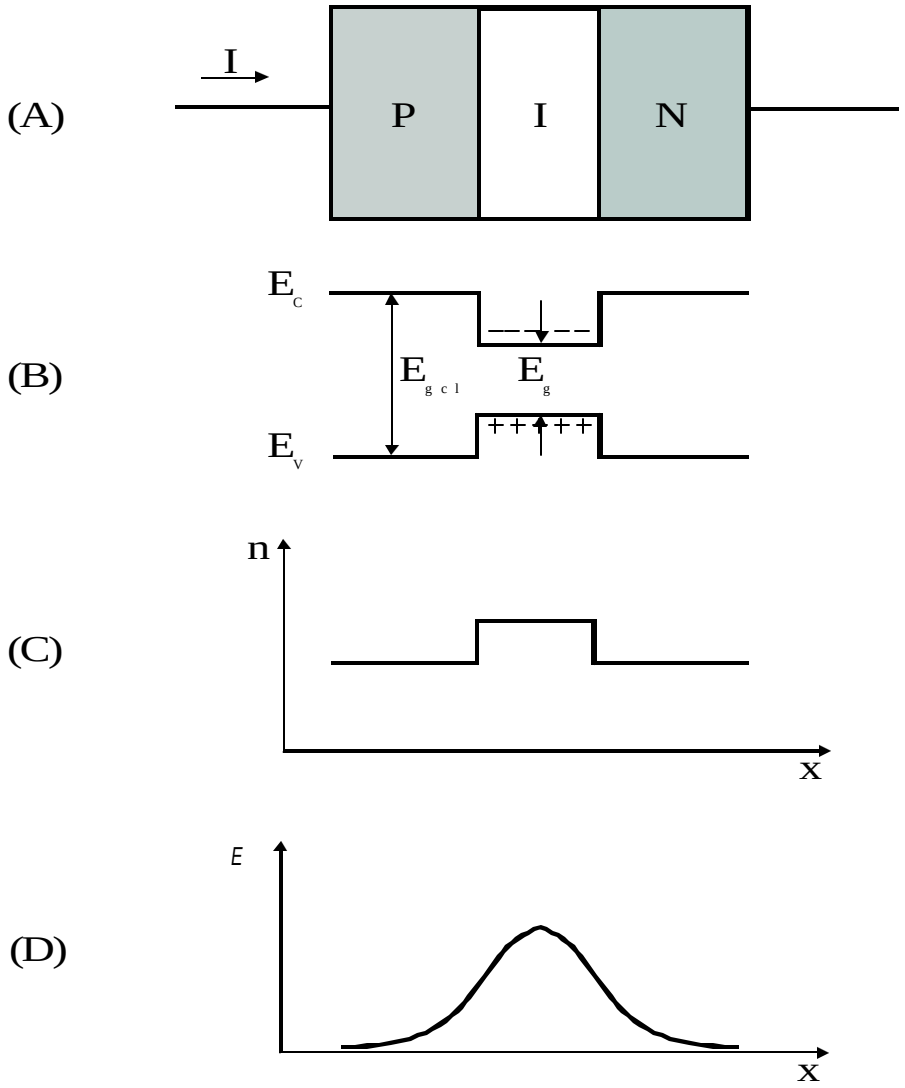

Figure 3.6 Aspects of the double-heterostructure diode laser: (A) a schematic of the material structure; (B) an energy diagram of the conduction and valence bands vs. transverse distance; (C) the refractive index profile; (D) the electric field amplitude profile for a laser mode.

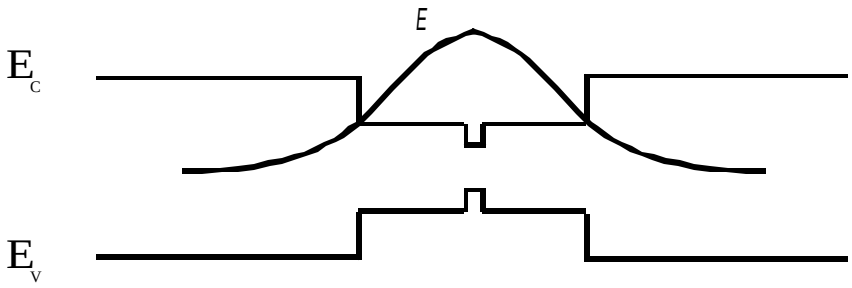

Figure 3.7 Transverse band structure for a standard separate-confinement heterostructure (SCH) quantum-well laser.

3.3 Laser structures

This section will discuss some representative laser structures. These different laser structures can be generally categorized into two groups: edge-emitting and surface-emitting. Edge-emitting lasers are also called in-plane lasers, meaning laser cavities and laser beams are in a plane parallel to laser wafer substrates. In contrast, a surface-emitting laser emits a laser beam perpendicular to the wafer substrate. Single axial-mode and single transverse-mode operation is generally required for the high-resolution absorption spectroscopy used in this thesis. Different mechanisms are used to achieve single axial mode and single transverse mode. The general approach to achieve single transverse mode is to introduce some finite aperture in laser structures so that higher-order transverse modes compete less favorably than the fundamental transverse mode and thus could not reach lasing threshold. It is relatively straightforward to apply this approach to diode lasers for absorption gas sensors, since large laser power is not required. In contrast, different approaches are used to achieve single axial-mode operation for edge-emitting and surface-emitting lasers. Therefore, this section will emphasize the mechanisms for achieving single axial-mode operation.

3.3.1 Edge-emitting lasers

Figure 3.8 illustrates the far-field angular distribution of the optical intensity of an edge-emitting laser. Guiding of the optical field in the transverse direction (perpendicular to the layers of the structure) is obtained by the double heterostructure described in the last section. Waveguiding in the lateral direction can be obtained by gain guiding (i.e., guiding by the imaginary part of the complex refractive index), index guiding (i.e., guiding by the real part of the complex refractive index) or a combination of them. However, it is difficult for the laser beam in an edge-emitting laser to have the same dimension in both directions. Usually, as it leaves the laser, the beam is small in the transverse direction and relatively larger in the lateral direction. As it propagates to

the far field, the situation reverses because of diffraction, with a relatively large beam in the vertical direction and a smaller beam in the horizontal direction, as illustrated in figure 3.8.

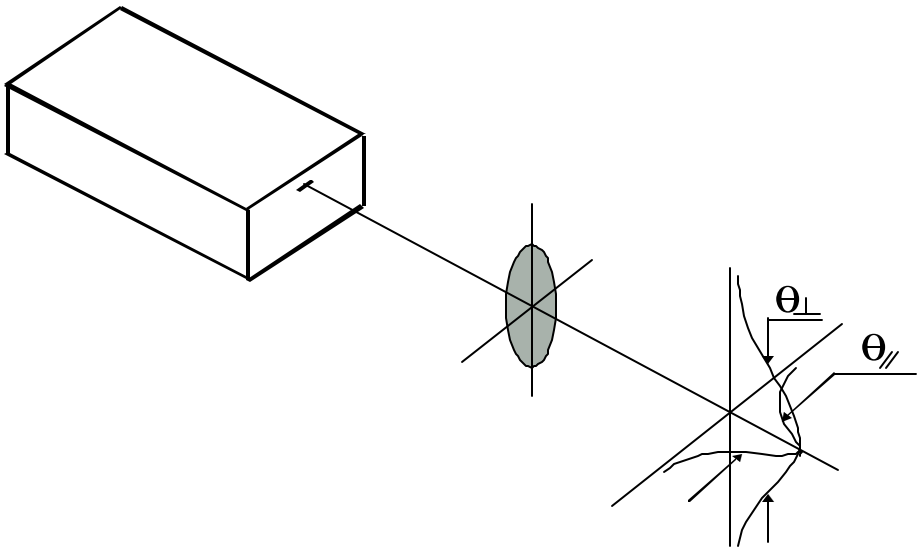

Figure 3.8 Illustration of the divergence of a laser beam in the vertical and horizontal directions from an edge-emitting laser.

A. Fabry-Perot (FP) lasers

For edge-emitting lasers, simple cleaved facets can be used to form necessary resonant cavities for optical feedback. The large refraction discontinuity at the semiconductor-air interface provides a reflection coefficient of ~30 percent. For some special applications or to protect the active materials, passivation coatings may be applied to the cleaved facets. The cleaved surfaces have the advantage of perfect parallelism. These plane-parallel facets form a Fabry-Perot cavity, and therefore such lasers are called Fabry-Perot (FP) lasers.

For FP lasers with a cross section shown in figure 3.1, the wavelength separation between two modes is

$$dl = \frac{l^2}{2\left(\bar{n}_{ga} L_a + \bar{n}_{gp} L_p\right)}, \tag{3.11}$$

where $\bar{n}_{ga}$ and $\bar{n}_{gp}$ are the effective group indices of the active and passive sections. For typical FP diode lasers with a length of several hundred micrometers to several millimeters, the mode spacing is less than several nanometers. The gain bandwidth of semiconductor diode lasers is typically several tens of nanometers, much larger than the mode spacing of typical FP cavities. As

a result, it is often the case that the laser does not run in single mode, or at least may hop between several modes. This is highly undesirable for high-resolution spectroscopic applications. Several laser structures, e.g., coupled cavity, can provide single-mode operation. The most popular structure is based on the wavelength-selective reflection capability of grating structures and will be discussed next.

B. Distributed Bragg reflector (DBR) and distributed feedback (DFB) lasers

Both DBR (figure 3.9) and DFB (figure 3.10) laser structures rely on the wavelength-selective reflection capability offered by periodic grating structures, usually formed by corrugating an interface in the laser structure. This corrugated structure highly reflects light when the wavelength is such that the period of the corrugation is an integer number of half wavelength in the material (this condition is defined as the Bragg condition). This high reflection results from the constructive addition of the reflected light from every corrugation period. This distributed grating structure is called a distributed Bragg reflector.

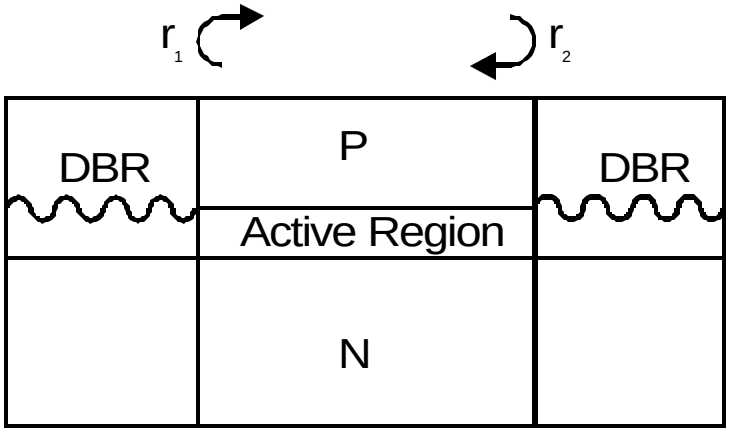

Figure 3.9 A distributed Bragg reflector laser structure.

A DBR laser can be formed by replacing one or both of the discrete mirrors with a distributed Bragg reflector (figure 3.9). These reflectors are formed along passive waveguide sections. In contrast, DFB lasers are formed by making grating structure along the active region (figure 3.10) rather than the passive regions for DBR lasers. Historically, DFB lasers preceded the DBR lasers, primarily because of its simplicity and relative ease of manufacturing. For standard DFB lasers with no shift in the grating (figure 3.10 a), it can be shown that the lasing wavelength is usually different from that satisfying the Bragg condition to satisfy the phase requirement for lasing. One variant form is the quarter-wave shifted DFB laser (figure 3.10 b), and then the exact

Bragg wavelength satisfies the phase requirement for lasing. Therefore, the quarter-wave shifted DFB lasers reach threshold with smaller gain and thus have lower threshold current.

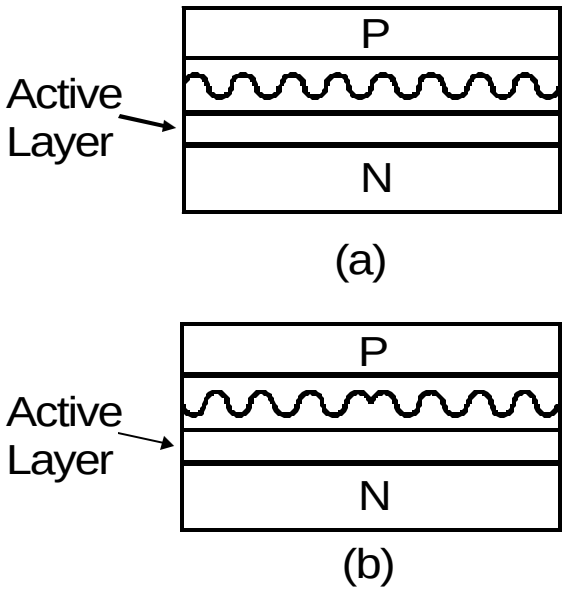

Figure 3.10 (a) Standard distributed feedback (DFB) laser structure (b) quarter-wave shifted DFB structure.

The top diagram of figure 3.11 shows how a DBR or DFB laser realizes single-axial mode operation. a_m denotes mirror loss, i.e., $\frac{1}{L_a + L_p}\ln(r_1 r_2)$ with the notation in Eq. (3.1). $<\Gamma g - a_i>$ represents the net gain and loss of the laser material averaged over the entire laser length, i.e., $\frac{1}{L_a + L_p}\left[(\Gamma g - a_a)L_a - a_p L_p\right]$ with the notation in Eq. (3.1). The laser reaches threshold when $<\Gamma g - a_i> = a_m$. The single axial-mode operation is achieved by the relatively narrow stopband of the Bragg reflectors. The width of the central stopband of gratings is

$$\Delta l \approx \frac{l^2}{\bar{n} L_g}, \tag{3.12}$$

where l is the laser wavelength, $\bar{n}$ is the average refractive index of the grating materials, and L_g is the grating length. The width of the central stopband is inversely proportional to the grating length. For DBR or DFB lasers, the grating is made sufficiently long that the obtained wavelength-selective reflection provides enough suppression of one mode over other modes.

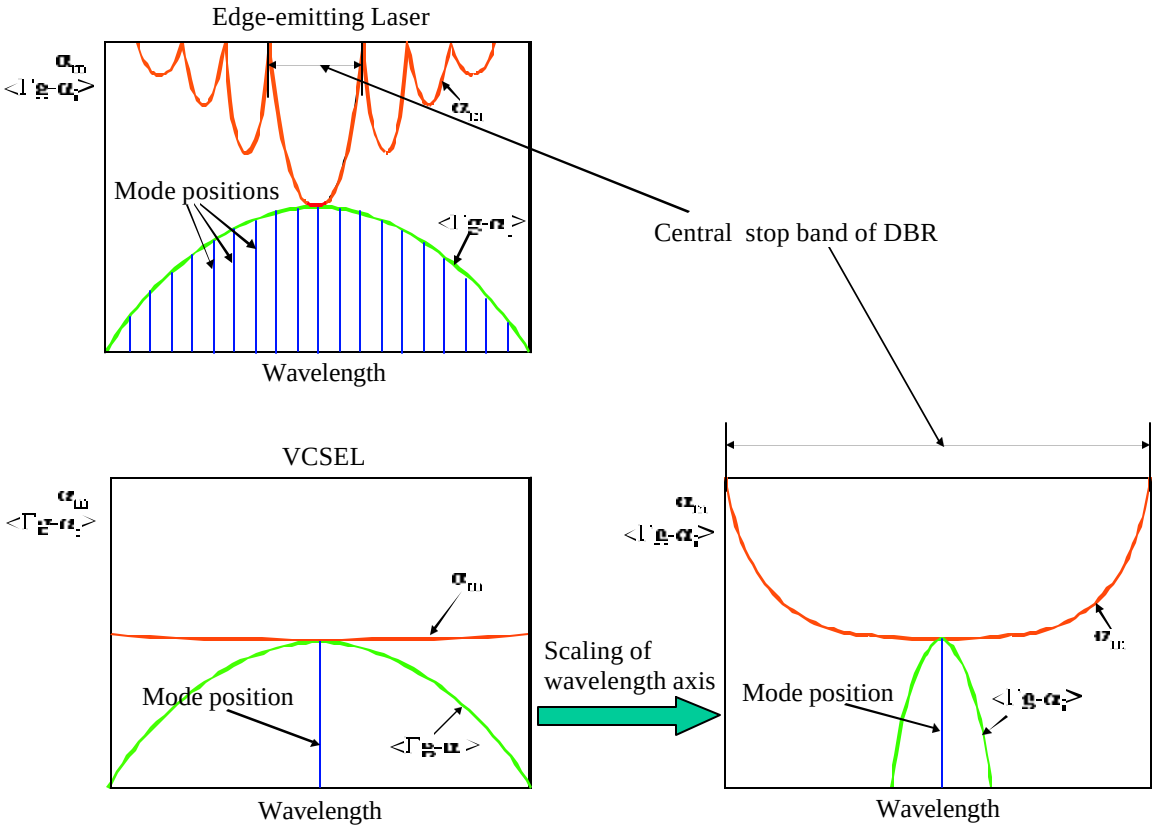

Figure 3.11 Schematic illustration of how a single axial mode is selected in an edge-emitting or a VCSEL laser. The wavelength axis of the right bottom diagram is scaled to show the mirror loss in a larger wavelength range. The gain curve has the same width in all three plots.

3.3.2 Surface-emitting lasers

Over the years, many configurations of surface-emitting lasers have been considered, e.g., the grating-coupled surface-emitting laser and the 45° deflecting-mirror surface-emitting laser. This section focuses on the vertical-cavity surface-emitting laser (VCSEL) structure. Proposed by Professor Kenichi Iga at Tokyo Institute of Technology in 1977, the VCSEL structure is the most widely used and most actively researched surface-emitting laser structure.

Figure 3.12 shows the schematic of a VCSEL structure. A VCSEL is like a DBR laser, but made in the vertical direction. With this vertical structure, a circular laser beam with low beam divergence can be easily achieved. This makes them much easier to interface to fibers than edge-

emitting lasers. Therefore, the packaging cost, which typically accounts for the main part of laser cost, can be significantly reduced. In addition, this vertical structure allows the cavity mirrors to be epitaxially grown or deposited by vapor deposition techniques on a wafer scale. Since laser cavities have been formed before dicing wafers and light comes out perpendicular to the wafer surface, automatic on-wafer probe stations can be used to conveniently and efficiently characterize the electrical, optical and electro-optical performance of devices on the entire wafer. Bad devices can be screened out before expensive packaging process. This wafer-scale manufacturing and testing capability is another significant advantage of VCSELs over edge-emitting lasers.

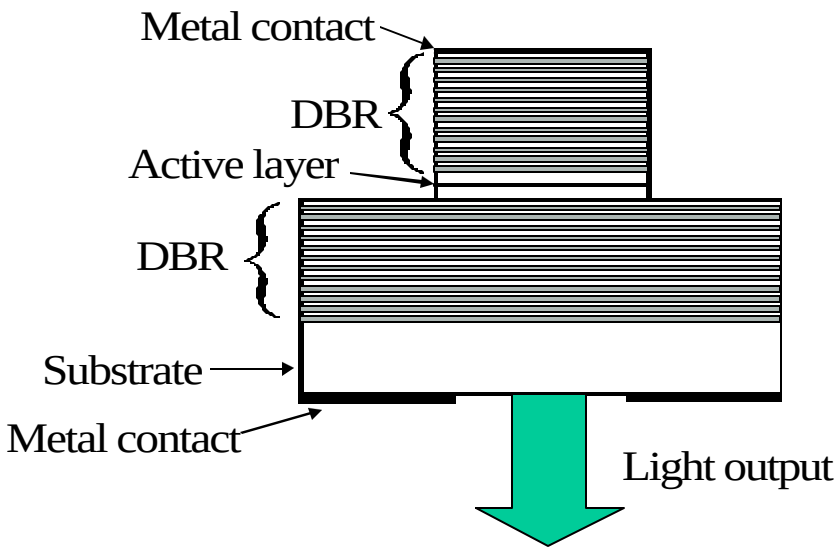

Figure 3.12 Schematic of a VCSEL structure. Light emits from the transparent substrate.

The length of the active region (L_a) of VCSELs is the thickness of the active layer (figure 3.12), and thus is significantly shorter than that of edge-emitting lasers, where the length of the active region is defined by the length rather than the thickness of the active layer. The total gain in electrically pumped VCSELs is on the order of 1% due to the thin thickness of the active layer. Therefore, the mirror loss, material loss and waveguide loss need to be very small to achieve lasing. Making high-reflectivity mirrors is one of the most difficult challenges encountered in VCSEL fabrication, especially for 1.3-μm and 1.5-μm VCSELs.

For short-wavelength (0.7~1 μm) VCSELs, high-reflectivity DBRs can be easily formed with AlGaAs material system due to the large refractive index difference between AlAs and GaAs. For

1.3-μm and 1.5-μm lasers, the material systems historically used are InGaAlAs and InGaAsP, lattice-matched to InP substrate (figure 1.1). However, the refractive index difference that can be achieved with these two material systems is very small, and thus a large number of periods of DBR layers must be grown to achieve >99% reflectivity. To grow such thick DBR layers with good lattice matching and strain control is a formidable task. In addition, the heterojunctions of DBR layer interfaces, especially in the p-type DBRs, pose barriers for efficient carrier injection, and thus special doping profiles and material composition profiles are required around these interfaces to make the barrier less steep and thus reduce the electrical resistivity. This further complicates the growth process. Finally, the thermal properties of the DBRs with these materials are much worse than those of AlGaAs DBRs, and the operating current of these long-wavelength VCSELs is also higher than AlGaAs-based VCSELs. Therefore, the thermal management of these long-wavelength VCSELs is also very demanding.

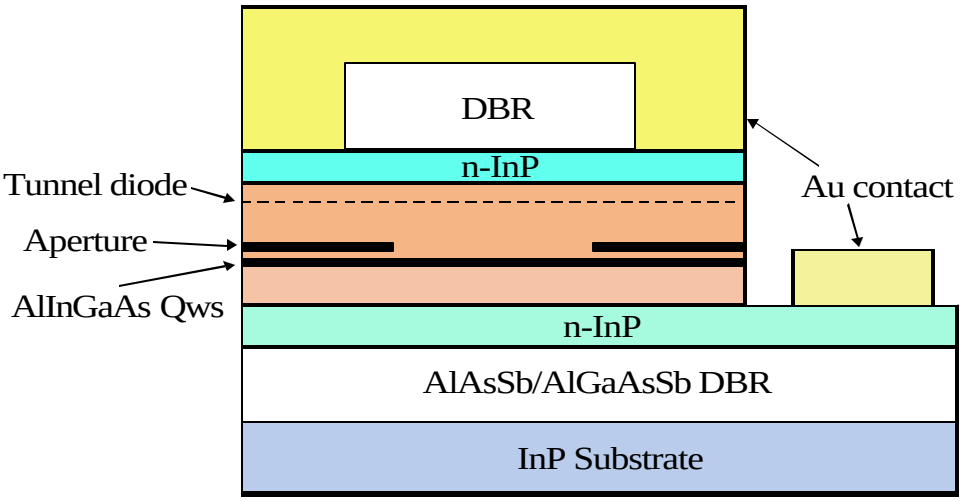

Figure 3.13 Double intracavity-contacted 1.5 μm single mode VCSEL (Coldren *et al.*, UCSB; 2001)

Alternative approaches have recently been proposed and demonstrated to achieve these 1.3-μm and 1.5-μm VCSELs. Representative schemes includes: 1) AlGaAsSb DBRs lattice-matched to InP substrate are used in combination with InGaAlAs or InGaAsP gain region (Hall *et al*, 2001) because of the large refractive index difference between AlAsSb and AlGaAsSb (Guden and Piprek, 1996); 2) intracavity contacts and extended cavity are used to improve the electrical and thermal performance (figure 3.13; Coldren *et al.*, 2001); 3) InGaNAs active region system lattice-matched to GaAs substrate is used to take advantage of the mature AlGaAs DBR technology (Harris, 2000; Steinle *et al.*, 2001). One such scheme is shown in figure 3.14.

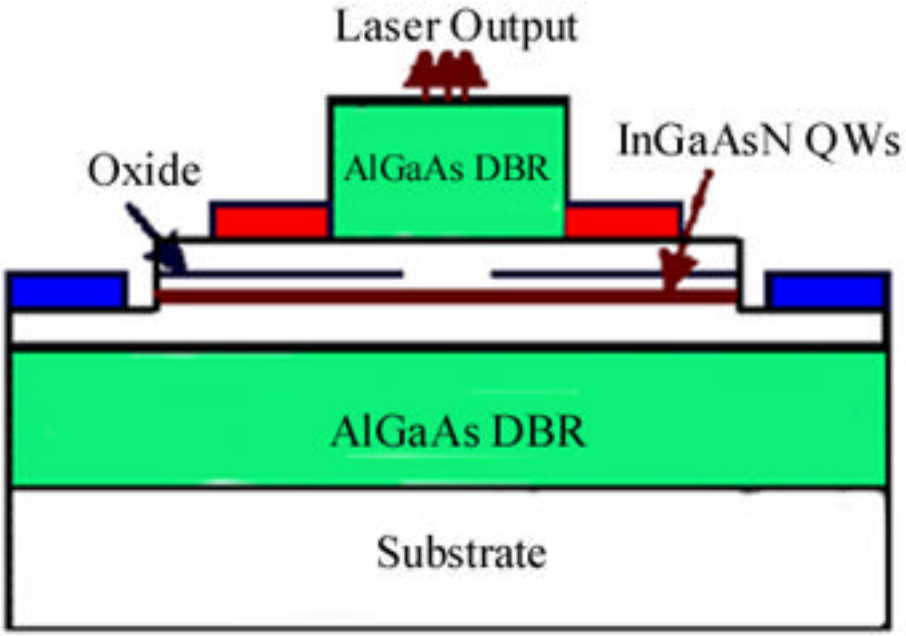

Figure 3.14 1.3-μm InGaAsN VCSEL with AlGaAs DBRs (Steinle *et al.*, Infineon Technologies; 2001).

VCSELs operating in the 2-3 μm range have been successfully demonstrated with Sb-based materials (Bewley *et al.* 1999; Baranov *et al.* 1998). These VCSELs are ideal candidates for gas-sensing applications. For these VCSELs, AlSbAs-GaSb DBRs were used. Since they have large difference of refractive index, less than 20 periods of quarter-wave stacks can achieve sufficient DBR reflectance. In addition, these materials (binary or ternary rather than quaternary alloys) have relatively good thermal properties, and thus the thermal management of these VCSELs is relatively straightforward.

The two bottom diagrams of figure 3.11 illustrate the mechanism to achieve single axial-mode operation in VCSELs. The DBR typically consists of several to several tens of periods of quarter-wave stacks with alternative high and low refractive indices. The length of these DBR mirrors are significantly shorter than those in DBR or DFB lasers, therefore, the stopband width of DBR mirrors in VCSELs are significantly wider. In this case the DBR is not used to select single axial mode, but to obtain the high reflectivity required to achieve lasing. The single axial mode is intrinsically achieved in electrically-pumped VCSELs. Since the effective cavity length of electrically-pumped VCSELs is typically only one wavelength or at most several wavelengths for the extended cavity design (figure 3.13), the axial mode spacing is much larger than the gain

bandwidth of the semiconductor material. For VCSELs the single axial-mode operation is, therefore, intrinsically achieved by the short effective cavity length of VCSELs.

However, due to the relatively large lateral dimension, VCSELs may operate multi-transverse mode. It is necessary to incorporate some mechanism of suppressing high-order transverse modes to achieve single transverse mode operation. There are several common ways to achieve this. One way is to limit the optical aperture size of the annular metal contact (figure 3.12). This method is adopted for the 760-nm VCSELs used in this thesis for oxygen measurements. A better way is to put an oxide aperture near the active layer to provide guiding for both current and light field (figure 3.13 and 3.14).

3.4 Laser dynamics

The detailed dynamics of semiconductor lasers as we modulate them at high speeds is rather complicated, especially when the modulation amplitude is large. However, for modulation spectroscopy applications, the modulation amplitude is typically small, and thus the relatively simple rate-equation model can be used to understand the phenomena with reasonable accuracy. Like other laser systems, two coupled rate equations, one for photon and the other for gain species (carrier in this case), are necessary to describe the laser dynamics.

Rate-equation analysis is simply a conservation analysis on the rate basis. Figure 3.15 shows the inputs and outputs of the carrier and photon reservoirs for the rate-equation analysis of a single-mode laser. It is assumed here that there is only one carrier reservoir, i.e., all carriers behave in the same way. Otherwise, several carrier reservoirs need to be introduced to consider the different carrier behaviors.

First, consider the carrier reservoir, I/q carriers are injected into the laser, of which only $h_i I/q$ reach the active region, where h_i is the internal efficiency. The rest recombine elsewhere in the device. Some carriers in the carrier reservoir non-radiatively recombine at the rate $R_{nr}V$, where V is the volume of the active region. Some spontaneously recombine at the rate $R_{sp}V$, of which $R_{sp}^{'}V$ go into the laser mode. The rest recombine via stimulated emission into the laser mode at the rate $R_{21}V$. Some photons in the photon reservoir are absorbed to generate carriers at

the rate $R_{12}V$. The carrier reservoir has NV total carriers, where N is the carrier number per unit volume. Therefore the carrier number rate equation is

$$\frac{d(NV)}{dt} = \frac{h_i I}{q} - (R_{sp} + R_{nr})V - (R_{21} - R_{12})V \ . \tag{3.13}$$

For the photon reservoir, the stimulated and spontaneous emission into the laser mode provide the photon generation at the rate $R_{21}V + R_{sp}^{'}V$. The stimulated absorption depletes photons at the rate $R_{12}V$. All other photons leave the cavity at the rate $\frac{N_p V_p}{t_p}$, where V_p is the optical mode volume, and t_p is the carrier effective lifetime. Of those leaving the cavity, only $h_0 \frac{N_p V_p}{t_p}$ leave through the desired mirror as useful output power, P_0, where h_0 is the optical efficiency of the laser. The photon reservoir has $N_p V_p$ photons, where N_p is the photon number density per unit volume. The photon number rate equation is then

$$\frac{d(N_p V_p)}{dt} = (R_{21} - R_{12})V - \frac{N_p V_p}{t_p} + R_{sp}^{'}V \ . \tag{3.14}$$

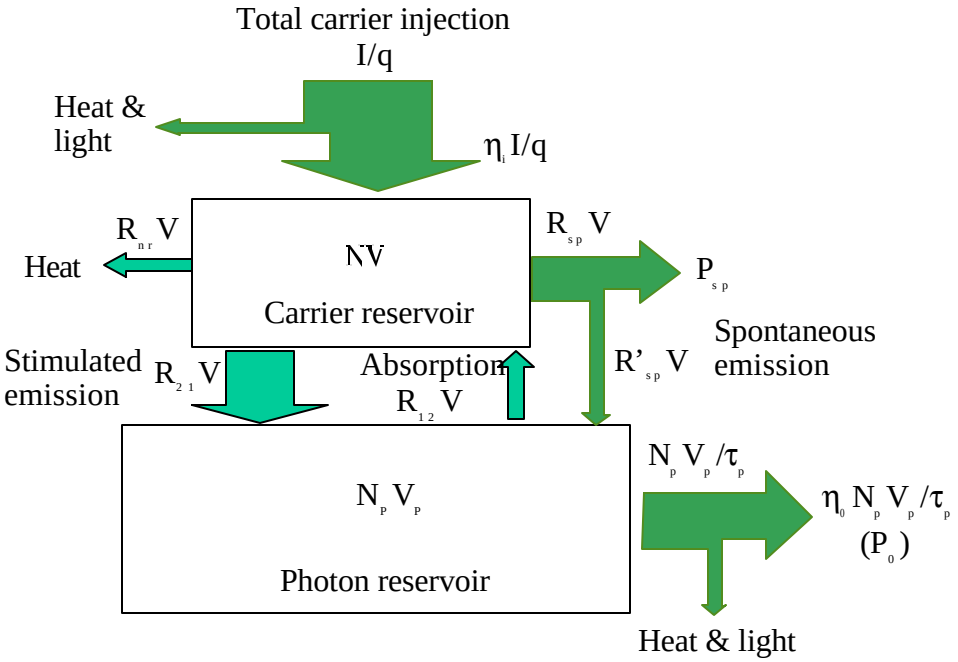

Figure 3.15 Conservation of carriers and photons used in the rate-equation analysis of semiconductor lasers.

The net stimulated emission term $R_{21} - R_{12}$ can be expressed in terms of the material gain per unit length, g, and the photon number density, N_p. The number of photons added to the light beam in the laser mode per unit length per unit volume inside the laser cavity is simply the gain coefficient, g, times the number of photons per unit volume, N_p, in the laser mode, i.e., gN_p. Since the photons in the laser mode are traveling at the group velocity v_g inside the cavity, the number of photons added to the beam per unit volume per unit time is $v_g g N_p$. By dividing out the corresponding reservoir volumes from above rate equations of total numbers, rate equations of number densities can be obtained:

$$\frac{dN}{dt} = \frac{h_i I}{qV} - (R_{sp} + R_{nr}) - v_g g N_p, \tag{3.15}$$

$$\frac{dN_p}{dt} = \left[\Gamma v_g g - \frac{1}{t_p} \right] N_p + \Gamma R_{sp}^{'}, \tag{3.16}$$

where Γ is the volume ratio V/V_p, called mode confinement. For electrically pumped VCSELs, since the cavity length is only one wavelength, except for the extended-cavity case, the standing-wave effect enhances the effective gain, which can be considered by using an effective Γ.

Before going into the detailed mathematical derivation of the laser dynamics, it is helpful to first think about the physical interaction between the two reservoirs. Suppose we increase the carrier density in the laser. This will cause an increased gain, and thus the photon density will tend to build up in the laser due to the $\Gamma v_g g N_p$ term in Eq. (3.16). The resulting increase in photon density, however, tends to cause the carrier density to start to fall because of the increased stimulated recombination (i.e., the $v_g g N_p$ term in Eq. (3.15)). That decrease in carrier density then tends to cause the photon density to fall, which tends to cause the carrier density to rise, and so on. This intrinsic oscillatory process limits the highest frequency of efficient modulation.

For modulation spectroscopy, lasers are subject to a small sinusoidal modulation of the injection current in addition to a bias current. Since the amplitude of this modulation is typically small, the small-signal frequency analysis of the modulation process will be presented below. Since laser relative intensity noise (RIN) limits the best achievable detection sensitivity, lasers

usually operate well above threshold to obtain low RIN. Under this condition, the spontaneous emission term $\Gamma R_{sp}^{'}$ in Eq. (3.16) can be neglected.

The gain increases with increasing carrier density while it decreases with increasing photon number density. This dependence can be approximated as:

$$g(N, N_p) = \frac{g_0}{1 + e N_p} \ln\left(\frac{N + N_s}{N_{tr} + N_s} \right), \tag{3.17}$$

where e is the gain compression factor introduced to reflect the effect of photon density on the gain; N_s is a parameter introduced that the gain does not go to infinity at zero carrier number density; and N_{tr} is the number density at which the material just reaches transparency. Under small perturbations of the carrier and photon number densities, the gain variation can be expressed as

$$dg = a dN - a_p dN_p, \tag{3.18}$$

where $a = \frac{1}{1 + e N_p}\left(\frac{g_0}{N + N_s} \right)$ and is called the differential gain; $a_p = \frac{e g}{1 + e N_p}$.

Considering I, N, and N_p as dynamic variables, the differentials of Eqs. (3.15) and (3.16) become

$$\frac{d}{dt}\begin{bmatrix} dN \\ dN_p \end{bmatrix} = \begin{bmatrix} -g_{NN} & -g_{NP} \\ g_{PN} & -g_{PP} \end{bmatrix}\begin{bmatrix} dN \\ dN_P \end{bmatrix} + \frac{h_i}{qV}\begin{bmatrix} dI \\ 0 \end{bmatrix} \tag{3.19}$$

where

$$\begin{aligned} g_{NN} &= 1/t_{\Delta N} + v_g a N_p, \\ g_{NP} &= 1/\Gamma t_p - v_g a_p N_p, \\ g_{PN} &= \Gamma v_g a N_p, \\ g_{PP} &= \Gamma v_g a_p N_p. \end{aligned} \tag{3.20}$$

Here, $\frac{1}{t_{\Delta N}} = \frac{dR_{sp}}{dN} + \frac{dR_{nr}}{dN}$. $t_{\Delta N}$ is called the differential carrier lifetime.

To derive the small-signal frequency response, the small perturbations of current, carrier and photon number densities are expressed as:

$$dI(t) = I_1 \exp(jwt),$$

$$dN(t) = N_1 \exp(jwt), \tag{3.21}$$

$$dN_p(t) = N_{p1} \exp(jwt).$$

Substituting into Eq. (3.19) and dividing out the common factor $\exp(jwt)$, obtain

$$\begin{bmatrix} g_{NN} + jw & g_{NP} \\ -g_{PN} & g_{PP} + jw \end{bmatrix} \begin{bmatrix} N_1 \\ N_{p1} \end{bmatrix} = \frac{h_i I_1}{qV} \begin{bmatrix} 1 \\ 0 \end{bmatrix}. \tag{3.22}$$

Solving this linear system, obtain

$$N_1 = \frac{h_i I_1}{qV} \frac{g_{PP} + jw}{w_R^2} H(w), \tag{3.23}$$

$$N_{p1} = \frac{h_i I_1}{qV} \frac{g_{PN}}{w_R^2} H(w), \tag{3.24}$$

where

$$H(w) = \frac{w_R^2}{w_R^2 - w^2 + jwg}, \tag{3.25}$$

$$w_R^2 = g_{NP} g_{PN} + g_{NN} g_{PP}, \tag{3.26}$$

$$g = g_{NN} + g_{PP}. \tag{3.27}$$

w_R and g are the relaxation resonance frequency and the damping factor of the intrinsic oscillation process, respectively. For operation well above threshold, the relaxation resonance frequency can be approximated as

$$w_R \approx \sqrt{\frac{v_g a N_p}{t_p}}. \tag{3.28}$$

Equation (3.24) shows that except a scaling factor, $H(w)$ is the modulation transfer function of the photon number density subject to an injection current modulation. The modulation of the photon number density manifests as the modulation of the laser intensity. For standard modulation spectroscopy that bases its detection on the laser wavelength modulation, this intensity modulation leads to an asymmetric signal shape and is also a source of extra noise. Therefore, it is deleterious and called residual intensity modulation. But the modulation technique for broadband absorption, introduced at the end of chapter 2, relies on this intensity modulation.

Figure 3.16 illustrates that the laser intensity will follow its drive force, i.e., the current modulation, at low frequencies. It will tend to resonate around the relaxation resonance frequency depending on the damping factor. At low bias current, the damping factor is small and the laser

modulation strongly resonates. The damping factor increases when increasing the bias current, and thus the resonance behavior becomes weaker at larger bias current. At very large bias current, the oscillation is overdamped and the resonance disappears. Above the relaxation resonance frequency, the laser intensity responds less and less (~40 dB/decade) to the driving force.

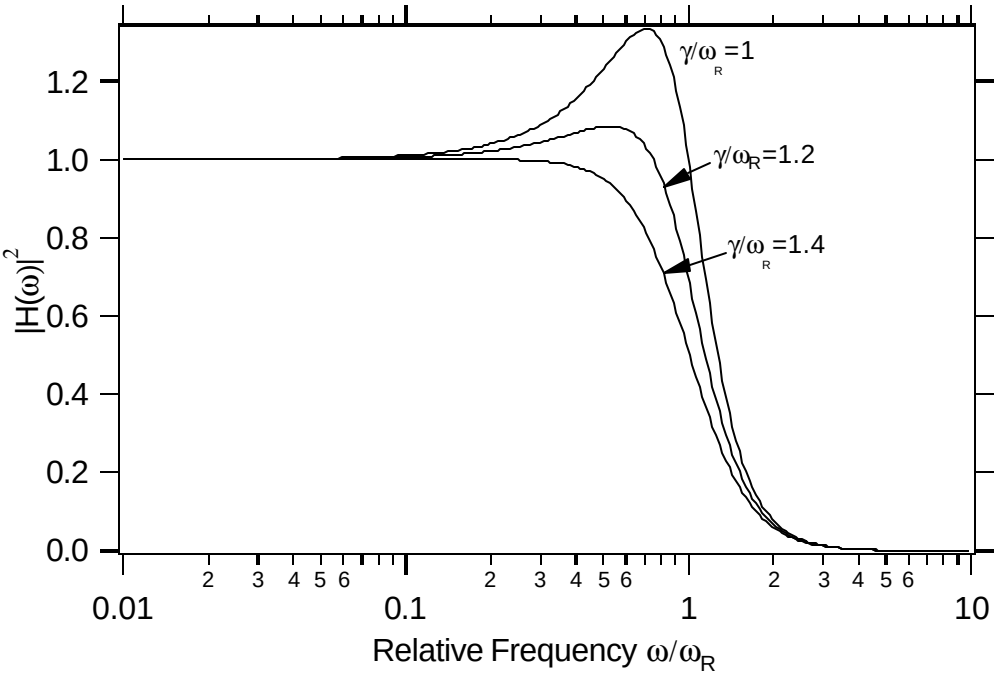

Figure 3.16 Illustration of the modulation transfer function $H(w)$.

Equation (3.23) shows that the carrier density is modulated by the injection current modulation. This modulation of the carrier density leads to a modulation of refractive index, which in turn modulates the laser wavelength. At low modulation frequencies the temperature of the laser is also modulated by the current modulation. Since the refractive index varies with temperature, the laser wavelength is also modulated via this thermal effect. The temperature and carrier effects are opposite in sign. The total modulation amplitude of the laser optical frequency, n_1, is the sum of these two contributions:

$$\frac{n_1}{I_1} = \left(\frac{n_1}{I_1}\right)_{carrier} + \left(\frac{n_1}{I_1}\right)_{thermal}. \tag{3.29}$$

Assuming a small modulation of the carrier number density that the optical frequency varies linearly with the carrier number density modulation, we have the carrier-variation induced frequency modulation:

$$\left(\frac{n_1}{I_1}\right)_{carrier} = \frac{h_i}{qV}\frac{g_{PP} + jw}{w_R^2} H(w)\left(\frac{dn}{dN}\right)_{bias} \tag{3.30}$$

where $\left(\frac{dn}{dN}\right)_{bias}$ is the frequency variation rate through the carrier number density near the bias condition. The wavelength modulation through this carrier effect is effective up to the relaxation resonance frequency w_R.

Assuming a uniform temperature of the laser cavity (i.e., the lumped capacitor model), the dynamics of the laser temperature can be described by:

$$cm\frac{dT}{dt} = \dot{Q}_{gen} - \dot{Q}_{dis} \ , \tag{3.31}$$

where c, m and T are the heat capacity, mass and temperature of the laser cavity, $\dot{Q}_{gen}$ is the heat generation rate by the injection current, and $\dot{Q}_{dis}$ is the heat dissipation rate through conduction to the laser mount. The heat dissipation rate can be further expressed as

$$\dot{Q}_{dis} = \frac{\Delta T}{Z_T}, \tag{3.32}$$

where ΔT is the temperature difference between the laser cavity and the laser mount, and Z_T is the thermal impedance of the laser structure. Like equation (3.21), the temperature perturbation around the equilibrium temperature T_0 can be expressed as

$$dT = T_1 \exp(jwt). \tag{3.33}$$

The right hand side of equation (3.31) can be separated into the part at the bias current condition (obviously, this part is zero), and the other part due to the current modulation:

$$\begin{aligned} \dot{Q}_{gen} - \dot{Q}_{dis} &= (\dot{Q}_{gen} - \dot{Q}_{dis})_{bias} + (\dot{Q}_{gen} - \dot{Q}_{dis})_{\mathrm{mod}} \\ &= (\dot{Q}_{gen} - \dot{Q}_{dis})_{\mathrm{mod}} \end{aligned} \tag{3.34}$$

Substituting these expressions into the equation (3.31) and dropping out the common factor $\exp(jwt)$, obtain

$$\left(jwcm + \frac{1}{Z_T}\right)T_1 = \left(\frac{d\dot{Q}_{gen}}{dI}\right)_{bias} I_1 . \tag{3.35}$$

Here a linear variation of the heat generation rate with the small injection current modulation is assumed. Therefore, the laser optical frequency modulation due to the thermal effect is

$$\left(\frac{n_1}{I_1}\right)_{thermal} = \frac{Z_T\left(\frac{d\dot{Q}_{gen}}{dI}\right)_{bias}\left(\frac{dn}{dT}\right)_{bias}}{1+jw\,cmZ_T}, \tag{3.36}$$

here the optical frequency is also assumed to vary linearly with the temperature modulation. The product cmZ_T is called the thermal time constant of the laser structure, which sets the high frequency limit of an efficient wavelength modulation through this thermal effect.

This thesis only uses the low-frequency (33kHz, $<<w_R$) wavelength-modulation spectroscopy technique, therefore, the laser intensity modulation has maximum response. The 2.3-μm GaSb-based lasers have a thermal time constant of several hundred microseconds, both carrier and thermal effects contribute to the wavelength modulation. The 760-nm VCSELs used in this thesis have a thermal time constant of several microseconds, and the wavelength modulation obtained is dominated by the thermal effect.

3.5 (Al)InGaAsSb/GaSb diode lasers

As briefly discussed in the chapter 1, 2.3-μm diode lasers can access the CO first-overtone band and thus are desired for sensitive CO measurements. The most commonly used diode lasers operating near room temperatures are based on AlGaAs/GaAs, InGaAsP/GaAs, and InGaAsP/InP systems and essentially cover the wavelength range between 0.7 and 2 μm (see figure 1.1). Although considerable progress has been made in the development of 2-μm diode lasers in both the InGaAsP/InP (Major *et al.* 1993) and (Al)InGaAsSb/GaSb (Choi *et al.* 1994) material systems, numerous attempts to expand upon these results to longer wavelengths had been unsuccessful (2.2-μm room-temperature continuous-wave InGaAlAs/InP diode lasers have been demonstrated recently (Kuang *et. al.* 2001)). For GaSb-based lasers, the limitation was associated with the miscibility gap for InGaAsSb quantum-well (QW) material (Garbuzov *et al.* 1998). Recently, considerable progress in the achievement of longer-wavelength room-temperature continuous-wave operation for GaSb-based diode lasers has been reported (Garbuzov *et al.* 1999). To avoid the structure degradation associated with the miscibility gap, structures with heavily-strained, quasi-ternary InGaSb(As) QWs outside the miscibility gap were grown. From these structures, 2.3-μm diode lasers with a 5-μm-wide ridge waveguide and a 0.25-mm-long cavity were successfully fabricated. CW output powers in the range of 1–20 mW were obtained and typical threshold currents were in the range of 50–80 mA at room temperature. CW

operation was obtained up to 50 °C. These lasers were used in this thesis for measuring CO concentrations.

Although these ridge-waveguide lasers employed Fabry-Perot configurations, single-dominant-longitudinal-mode operation was successfully achieved (Garbuzov *et al.* 1999) for some selected devices under certain ranges of temperature and current. Figure 3.17 presents the wavelength versus temperature characteristic of one such laser operating at 90 mA. The shaded regions show the regions in which the laser operated multimode while single-dominant-longitudinal-mode (~25-dB side-mode suppression, inset of Figure 3.17) operation was achieved outside the shaded regions. The high side-mode suppression in these single-dominant-longitudinal-mode regions enables absorption spectroscopy without mode-selection components such as monochromators which generally make the alignment and maintenance of optical systems difficult, reduce the radiation power, and introduce a significant amount of noise. These lasers are current- and temperature-tunable in the single-dominant-longitudinal-mode regions with the tuning rates in static or quasi-static conditions of about 0.063 nm/mA and 0.2 nm/°C (figure 3.18), respectively.

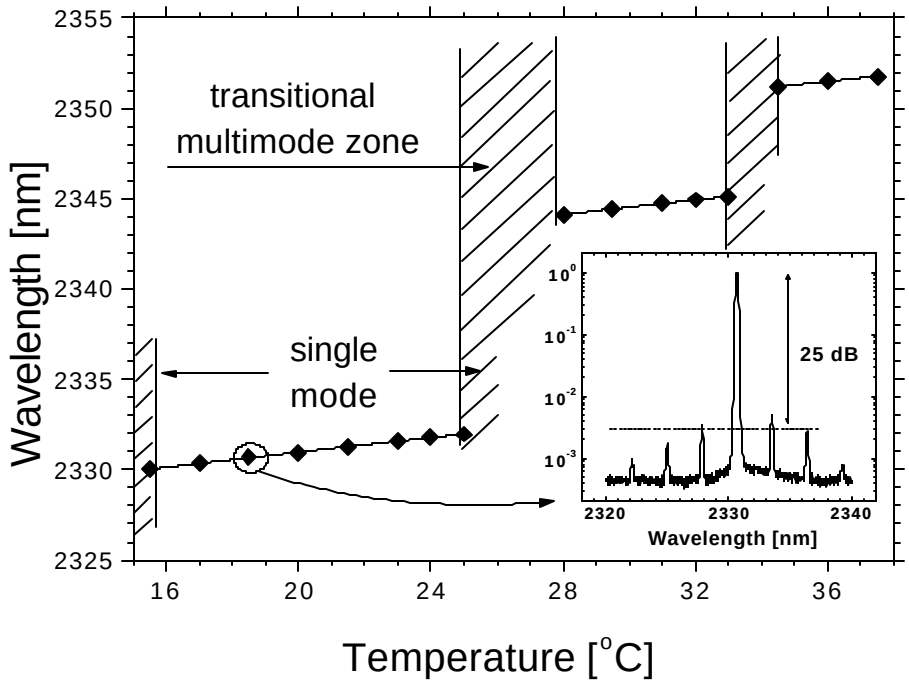

Figure 3.17 Wavelength vs. temperature characteristics for an (Al)InGaAsSb/GaSb laser (0.25-mm cavity length) at a fixed current (90 mA). The inset shows the lasing spectra acquired at 18.5°C.

Incidentally, the static current-tuning rate is conceptually different from the current-tuning rate through the small-signal modulation. Above the lasing threshold, the carrier number density is clamped to the threshold value for static operations (When increasing the current, the laser power is increased. The gain is in turn reduced due to the gain compression by the increased photon number density (equation (3.17)). To keep the gain at the threshold value, the carrier number density has to be increased. In addition, the laser gain is a function of temperature; therefore, the threshold carrier number density varies with the temperature which is different at different current levels. However, both effects are secondary). Therefore, this static current-tuning rate is solely due to the thermal effect, rather than the combination of the thermal and carrier effects discussed in the last section for the small-signal modulation, where the carrier number density is modulated around the threshold value. However, since the thermal effect dominates the tuning at low frequencies, the static current-tuning rate should be similar to the tuning rate of the small-signal current modulation obtained at low frequencies.

The devices used in this thesis were research-grade prototypes. They were mounted in L-shape submounts for research purposes. These lasers had not been subject to the burn-in process (usually lasting 96 hours) to screen out fragile devices as is done with commercial lasers. If so, only a very few of these lasers would survive. Though extreme care was paid when handling them, these lasers had very short lifetime. Of the twenty-six lasers received from Sarnoff Corporation, the best laser lasted ~3 months (the laser was only turned on when doing measurements, so the operating time was only ~200 hours). Some of them failed after only several minutes of testing.

Due to the mode-hopping behavior, these lasers had to be characterized over the whole matrix of temperature and current combination to find all possible single-mode regions (figure 3.18). Then these single-mode regions were compared with simulated spectra to identify candidate lasers and corresponding operating conditions for CO measurements. The single-mode region with good side-mode suppression as shown in figure 3.17 could not be found for approximately half of the devices tested, no matter what combination of current and temperature was used. To make things worse, the single-mode operation regions drifted quickly so that the temperature and current combination needed to be re-optimized frequently during the experiment. For example, one laser initially exhibited very good single-mode operation around the R(30) transition which was selected for the CO measurements in the immediate post-flame zone, and some reasonably

good preliminary data were obtained. Unfortunately the single-mode region drifted out of the transition before a more thorough study can be done. So the key to operate these lasers was to run experiments as fast as possible.

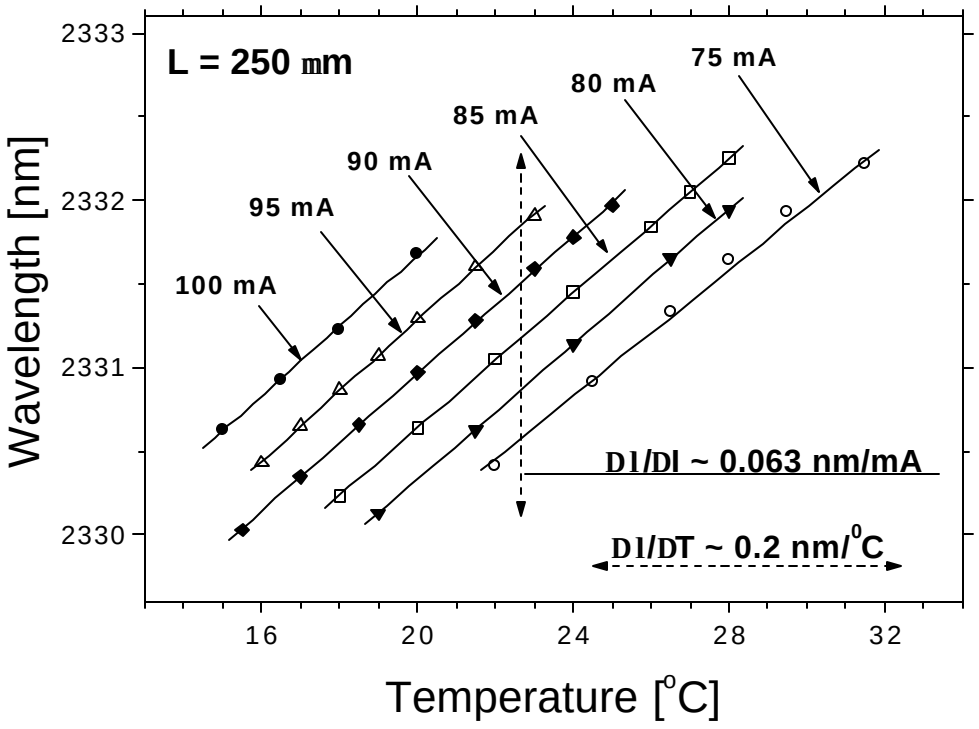

Figure 3.18 Temperature and current dependences of a single-mode operation region.

Laser structures, e.g., DFB, DBR or VCSEL, which can guarantee stable single-mode operation are necessary for in-field sensors. 2-μm DFB (Bleuel *et al.* 1999) and 2.2-μm VCSELs (Baranov *et al.* 1998) based on (Al)InGaAsSb/GaSb have been successfully demonstrated, and it is straightforward to extend these results to 2.3 μm (private contact with Sarnoff Corp.). However, significant progress on improving device reliability needs to be achieved before these lasers can be applied to long-term in-field applications. Unfortunately, Sarnoff Corporation and Sensors Unlimited Inc. decided to focus on telecom market and stopped improving these lasers. Hopefully, some other companies or institutes will attack the reliability issue.

Chapter 4. *In Situ CO Detection With 2.3-mm Lasers*

The 2.3-μm Sb-based continuous-wave room-temperature diode lasers have been applied to *in situ* CO measurements in both the exhaust duct and the immediate post-flame zone of an atmospheric-pressure, premixed, laminar, C_2H_4-air flat-flame burner. This work demonstrated for the first time the excellent performance of *in situ* CO sensors using first-overtone transitions. Unlike sensors using second-overtone transitions, these sensors do not suffer from interference from major combustion products.

4.1 Motivation

CO is a key indicator of combustion efficiency and thus is a good parameter for combustion sensing and control (Brouwer *et al.* 1990; Fujii *et al.* 1997). Because of its adverse effect on human health, CO is one of the six criteria ambient air pollutants regulated by the U.S. Environmental Protection Agency. Combustion processes are the dominant anthropogenic sources of CO and thus are facing increasingly stringent emission regulations. In addition, CO is considered to be a good surrogate of organic emissions from combustion processes (Kilgroe *et al.* 1990). Continuous emission monitoring (CEM) of CO concentration is required by the U.S. government for municipal waste combustors (U.S. Government 40CFR60), hazardous waste incinerators and boilers and industrial furnaces burning hazardous wastes (U.S. Government 40CFR264/266). Therefore, a fast, accurate, and convenient method for monitoring CO concentration in combustion environments is of great importance for compliance monitoring and combustion control.

Traditionally, the majority of CO concentration measurements have been recorded using extractive probes in conjunction with non-dispersive infrared (NDIR) analyzers. Delivering and conditioning a hot, moisture-saturated combustion gas for analysis can be a difficult process, requiring a complex sampling manifold which needs to be well maintained (Jahnke 1993). This sampling manifold gives a long time delay, and CO may also be lost in the sampling manifold due to many mechanisms, especially at high temperature conditions (Schoenung *et al.* 1981; Nguyen *et al.* 1995). Furthermore, NDIR devices employ wide-band infrared radiation sources in the wavelength range of the CO fundamental band; such instruments are potentially subject to interferences (U.S. Government 40CFR60: Reference Method 10) from the major combustion products, particularly H_2O, that also strongly absorb in the same wavelength range (Figure 4.1).

In situ sensors which have no time delay and no or less interference thus offer potential advantages.

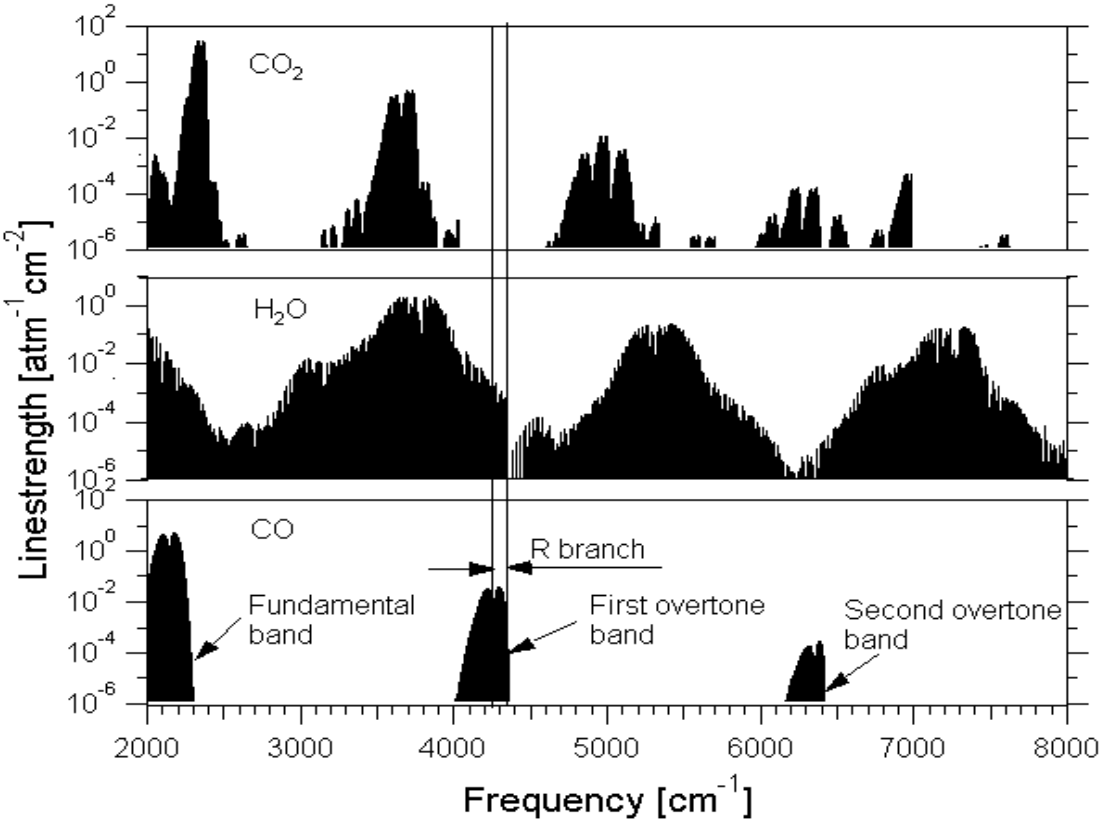

Figure 4.1 Survey spectra of CO and major combustion products H_2O and CO_2 at 500 K based on HITRAN96 database.

Tunable diode laser absorption spectroscopy (TDLAS) is non-intrusive, rugged, species specific and may be used for *in situ* measurements in high temperature flows. TDLAS also yields path-averaged species concentration, which can be beneficial in elucidating the overall performance for imperfectly mixed flows. Previous diode-laser based CO sensors for combustion measurements have been based on either lead-salt lasers (Schoenung *et al.* 1981; Varghese *et al.* 1981a) or InP (Upschulte *et al.* 1999; Mihalcea *et al.* 1998) lasers. Lead-salt lasers can access the CO fundamental band (near 4.6 μm), and *in situ* sensors based on them have been successfully developed and widely employed by combustion researchers. However, their deployment for in-field industry applications is rather limited, owing largely to operational complexity as they require cryogenic cooling and generally operate multi-mode with low power output. Recently developed near-room-temperature quantum-cascade pulsed lasers can also access the CO

fundamental band and several groups are currently developing portable CO sensors based on these lasers. Although InP-based diode lasers may operate single-mode and near room temperature, they operate in the near-infrared (1.3-2 μm) region and can thus access only the much weaker transitions in the CO second-overtone band near 1.56 μm (Figure 4.1). Weak linestrengths, as well as strong interference from the major combustion species CO_2 and H_2O, either limit measurements to large CO populations (Upschulte *et al.* 1999) or lead to a combination of extraction sampling, water filtering, and long-pathlength multipass cell (Mihalcea *et al.* 1998).

Recently developed room-temperature, continuous-wave, single-mode (Al)InGaAsSb/GaSb diode lasers operating near 2.3 μm (see section 3.5; also see, e.g., Garbuzov *et al.* 1999 and Maiorov *et al.* 1999) provide the capability to access transitions in the CO first overtone band and thus provide the opportunity for both sensitive *in situ* detection and operational convenience. The linestrengths of CO first-overtone transitions are more than 100 times stronger than those of the second-overtone transitions, and several CO transitions in the R branch are relatively isolated from neighboring H_2O and CO_2 transitions. In addition, the CO first overtone band falls within the spectral ranges of commercially-available extended-InGaAs, short-wavelength (<3 μm) HgCdTe, and InAs detectors. These detectors generally are cheaper, easier to use (room-temperature or TE-cooled) and have better noise performance or faster time response than the HgCdTe, InSb, and PbSe detectors employed for the 4.6-μm CO fundamental band.

In situ CO combustion measurements, in both the exhaust duct and the immediate post-flame zone of an atmospheric-pressure flat-flame burner, using the first-overtone absorption will be presented in this chapter.

4.2 Candidate transition selections

No or small spectral interference from the major combustion species CO_2 and H_2O, as well as large linestrength and laser accessibility, are the main criteria for selecting specific CO transitions. For high temperature measurements, since it is not easy to measure temperature accurately, low temperature sensitivity of the linestrength is also desirable.

Figure 4.2 presents calculated survey spectra of CO (10 ppm) and H_2O (10%) at 500 K and 1 atmosphere based on the HITRAN96 database. CO_2 absorption in this spectral range is negligible

at 500 K. Several CO transitions (R(4), R(6), R(10), R(11) and R(15)) with relatively large linestrengths are isolated from H_2O interference. The R(15) transition (4311.96 cm^{-1}) was selected for measurements in the exhaust region because of its minimum temperature sensitivity (figure 4.4, also figure 5.2) and laser wavelength access.

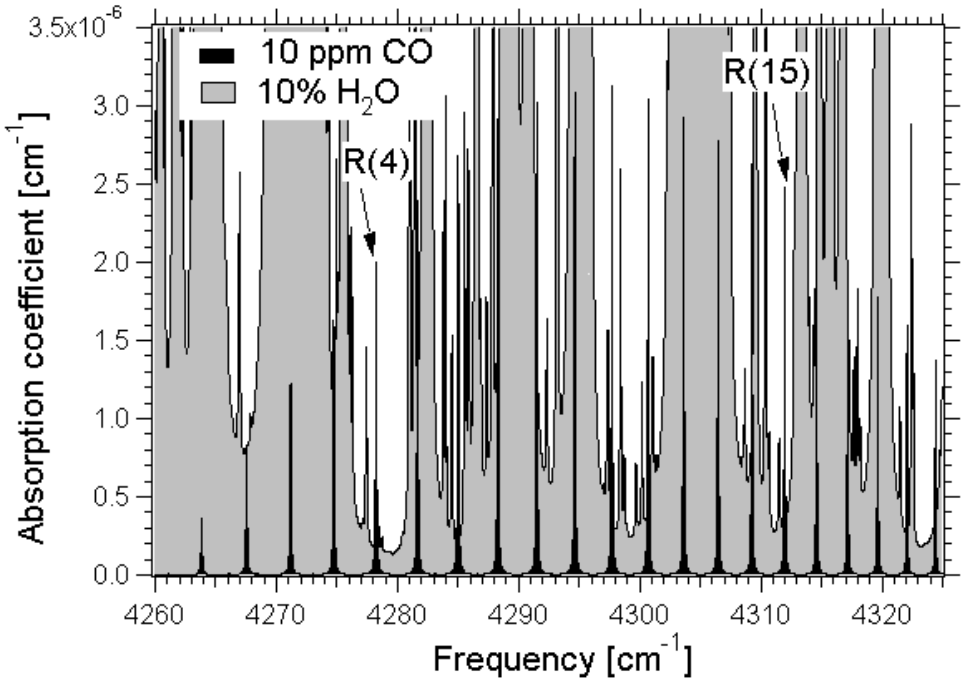

Figure 4.2 Calculated spectra of H_2O (10%) and CO (10 ppm) at 500 K, 1 atm based on HITRAN96 parameters.

Figure 4.3 presents calculated survey spectra of CO (500 ppm), H_2O (10%) and CO_2 (10%) at 1500 K and 1 atmosphere. H_2O and CO_2 spectra are calculated based on HITEMP96, a high-temperature extension of HITRAN96. Although there are several CO transitions isolated from H_2O and CO_2 absorption features at 500 K (Figure 4.2), interference from hot bands of H_2O and CO_2 in a flame is more severe. The R(30) transition (4343.81 cm^{-1}) was chosen for measurements in the immediate post-flame zone because it has small H_2O interference and no CO_2 interference based on HITEMP parameters.

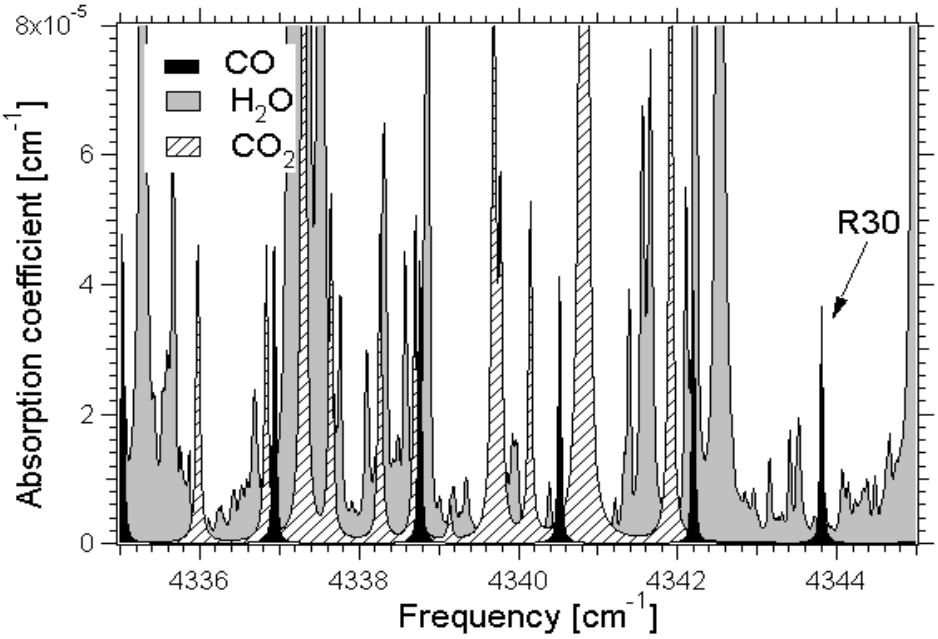

Figure 4.3 Calculated spectra of H_2O (10%), CO_2 (10%), and CO (500 ppm) at 1500 K, 1 atm based on HITEMP96 parameters.

Table 4.1 gives pertinent fundamental spectroscopic data of the R(15) and R(30) transitions for CO concentration measurements. Figures 4.4 presents calculated linestrengths and corresponding relative temperature sensitivities of the R(15) and R(30) transitions over the temperature range of interest for combustion monitoring. The HITRAN96 coefficients of the polynomial expression for CO partition function are tabulated in Table 4.2. Because of its large lower-state energy, the R(30) transition has low relative temperature sensitivity of linestrength ($\left|dS/dT\right|/S < 6.7\times10^{-4}\ \mathrm{K}^{-1}$) in the temperature range from 1000 K to 2200 K. A typical ±30 K temperature measurement uncertainty corresponds to a maximum uncertainty of only ±2% in linestrength.

Table 4.1 Fundamental spectroscopic data of the CO R(15) and R(30) transitions ($v' = 2 \leftarrow v'' = 0$).

CO transition	Lower-state energy, E_i'' [cm^{-1}]	Linecenter frequency, $\nu_{0,i}$ [cm^{-1}]	Linestrength, S_i [cm^{-2} atm^{-1}] at 300 K	
			HITRAN	Measured
R(15)	461.0545	4311.9617	3.38×10^{-2}	3.33×10^{-2}
R(30)	1782.6624	4343.8066	1.28×10^{-4}	1.26×10^{-4}

Table 4.2 HITRAN96 coefficients of the polynomial ($Q(T) = a + bT + cT^2 + dT^3$) for the partition function of CO.

Coefficients	$70 \le T \le 500$ K	$500 < T \le 1500$ K	$1500 < T \le 3005$ K
a	0.27758	0.90723×10^{1}	0.63418×10^{2}
b	0.36290	0.33263	0.20760
c	-0.74669×10^{-5}	0.11806×10^{-4}	0.10895×10^{-3}
d	0.14896×10^{-7}	0.27035×10^{-7}	0.19844×10^{-8}

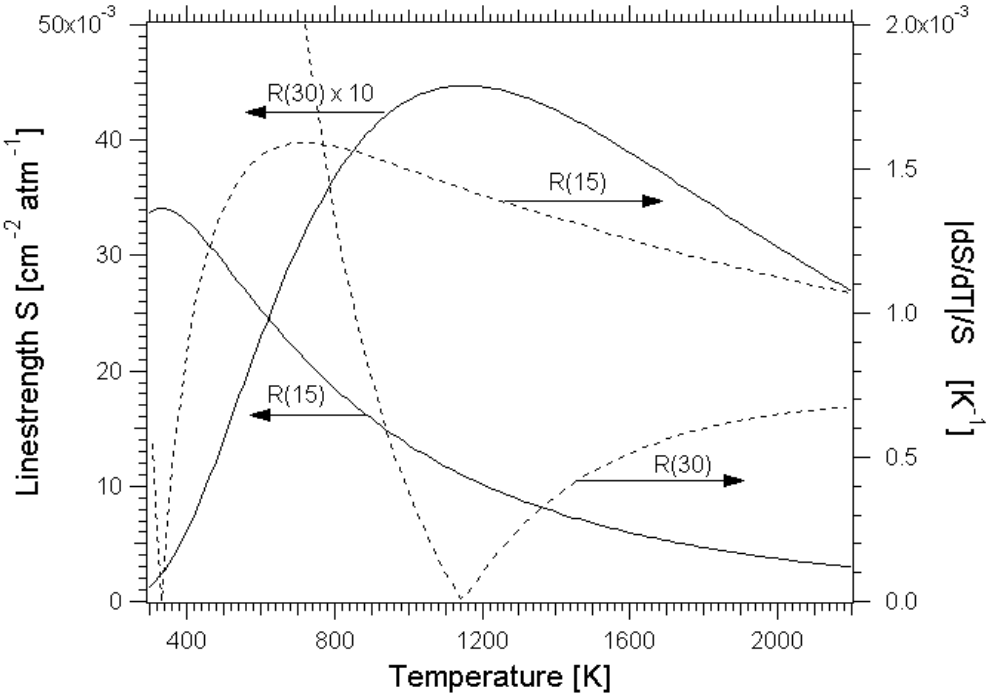

Figure 4.4 Calculated linestrengths and corresponding relative temperature sensitivities of the CO R(15) and R(30) transitions as a function of temperature.

4.3 Experimental Details

Figure 4.5 shows the experimental setup for *in situ* CO measurements using direct-absorption spectroscopy. Two In(Al)GaAsSb/GaSb diode lasers were employed to tune over the R(15) and R(30) transitions for measurements in the exhaust duct (79 cm above the burner) and the immediate post-flame zone (1.5 cm above the burner), respectively. Each laser was mounted in a TE-cooled heat sink and driven by a battery-powered low-noise current source. Each laser beam was then collimated by an off-axis paraboloidal reflector. A He-Ne laser beam was superimposed on each diode-laser beam to help with optical alignment. Both lasers can be tuned without mode hopping for approximately 1-cm^{-1} range centered around the linecenters by individually ramp-

modulating the injection currents of each diode laser while maintaining a constant case temperature. The lasers were rapidly scanned at 500 Hz to minimize beam-steering effects and low frequency (1/*f*) noise. Both lasers operate in a single dominant mode (~25-dB side-mode suppression) within the entire scanning ranges. A solid germanium etalon (1.42-GHz free spectral range; not shown in figure 4.5) was used to determine the relative frequency variations during the laser tuning. Transmitted beams were focused onto TE-cooled InAs detectors. The outputs of detectors were coupled to low-noise DC amplifiers (~100-kHz bandwidth). Amplified transmission signals were coupled to a 12-bit oscilloscope and oversampled at 2 MHz. The digitized signals were sent to a computer for analysis. A zero-phase forward and reverse IIR digital filter was used to reduce the signal bandwidth to 50 kHz without distorting the signals.

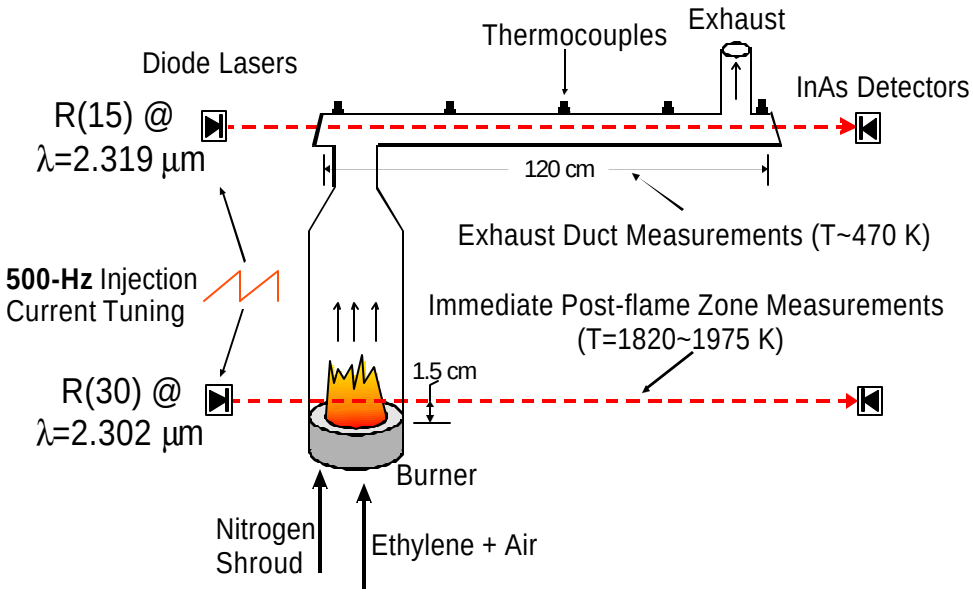

Figure 4.5 Schematic diagram of the experimental setup for *in situ* CO measurements in the exhaust and immediate post-flame regions of a flat-flame burner.

A water-cooled atmospheric-pressure C_2H_4-air premixed flat-flame (McKenna) burner (6-cm diameter) served as the combustion test facility for *in situ* CO concentration measurements. Ethylene and dry-air flows were metered with calibrated rotameters, premixed and injected into the burner. A fixed dry-air flow rate (30.9 l/min) was used with varying fuel flow rates (1.15–3.10 l/min) to adjust the equivalence ratio over a range ϕ=0.53–1.43. Uncertainty in the fuel flow rate, and thus the equivalence ratio, was estimated to be approximately ±2%. For measurements in the immediate post-flame zone, a nitrogen shroud flow was used to define the

bead. The effect of thermal conduction along the wire and radiation to the thermal couple are estimated to be negligible and not included in the equation. The thermal conductivity of the gas mixture at each equivalence ratio was calculated assuming a chemical equilibrium composition. A Nusselt number of 2.4 and a bead emissivity of 0.23 were used in the temperature correction calculation. Since the thermal conductivity is a function of temperature, the correction was iterated until convergence was achieved. For measurements in the exhaust duct, the nitrogen shroud was not employed. The laser beam was directed along the centerline of the horizontal duct (120-cm pathlength). Five thermocouples (uncoated type-S; 7.5-mil bead size) were distributed along the duct to measure the transverse temperature profiles.

4.4 Linestrength verification

Because of the importance of accurate linestrength values in direct-absorption measurements, the diode-laser absorption sensors were first applied to a 14.9-cm-long static gas cell with wedged windows to verify the HITRAN96 linestrength values of the CO R(15) and R(30) transitions. To measure the linestrength of the R(15) transition, 5% (Praxair primary standard, ±0.02% absolute) CO with balance N_2 was used. Measurements were made over a range of pressures and good data consistency was achieved (figure 4.6).

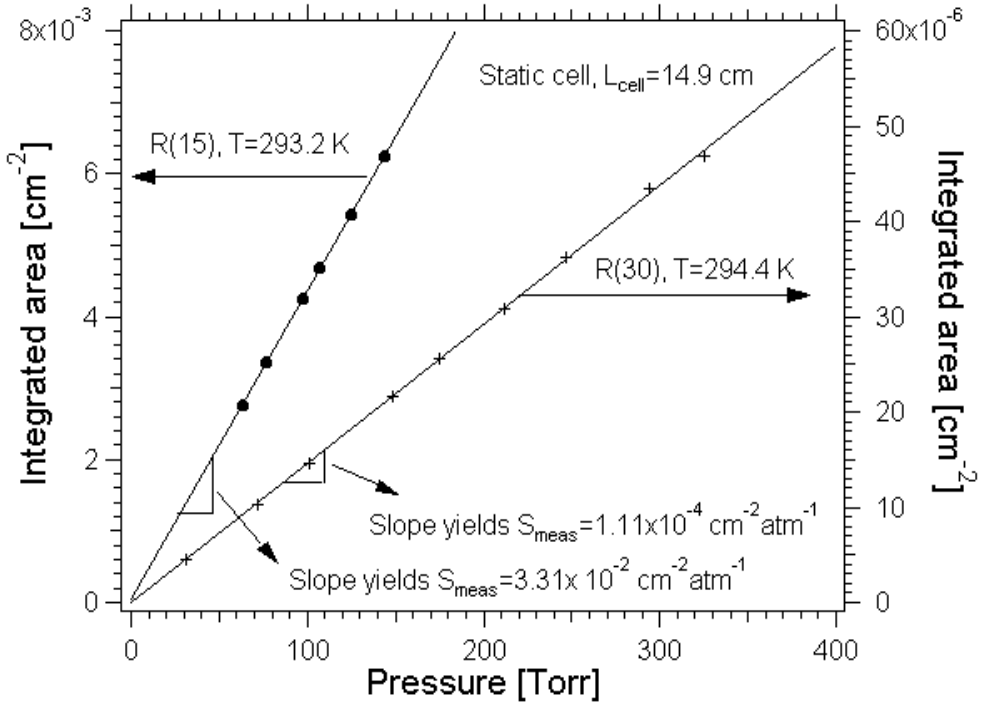

Figure 4.6 Measured integrated areas (per centimeter beam path) at various pressures for the CO *R*(*15*) and *R*(*30*) transitions.

The measured linestrength of 3.31×10^{-2} **[**cm^{-2} atm^{-1}] at 293.2 K agrees with the HITRAN96 value of 3.36×10^{-2} **[**cm^{-2} atm^{-1}] within the estimated ±3% measurement uncertainty. Pure CO (Praxair, 99.5%) was used to measure the linestrength of the R(30) transition. The linestrength of the R(30) transition is small at room temperature (Figure 4.4) and therefore the peak absorbances of static-cell measurements were only around 1%. However, as the noise equivalent absorbance of the static-cell measurements was only ~2×10^{-5}, high signal-to-noise ratios (~500) were achieved. The measured linestrength of 1.11×10^{-4} **[**cm^{-2} atm^{-1}] (figure 4.6) at 294.4 K agrees with the HITRAN96 value of 1.13×10^{-4} **[**cm^{-2} atm^{-1}] within the ±3% measurement uncertainty. These measured linestrengths of the R(15) and R(30) transitions were converted to values at 300 K and listed in the Table 4.1 together with the HITRAN96 values. Because the calculated partition function in the HITRAN96 database for the diatomic molecule CO is expected to be very accurate, no effort was made to verify the linestrengths at elevated temperatures.

4.5 Measurements in the exhaust duct

4.5.1 Direct Absorption

CO concentrations in the exhaust duct were first measured with direct-absorption spectroscopy. Since, in the horizontal exhaust duct, the temperature was relatively low, CO concentrations were essentially chemically frozen. Uniform CO concentration along the laser beam path can therefore be assumed. In this case, Eq. (2.19) can be reorganized to obtain:

$$X_{CO} = \frac{\int_{\nu} [-\ln(T(\nu))]d\nu}{P\int_0^L S(x)dx}. \tag{4.2}$$

The temperatures along the centerline of the exhaust duct dropped from ~540 K to ~400 K. Since it was this measured temperature profile that was used to evaluate the denominator integral in Eq. (4.2), only the fluctuation of this temperature profile contributed to the measurement uncertainty and thus no special effort was taken to reduce the temperature variation along the duct.

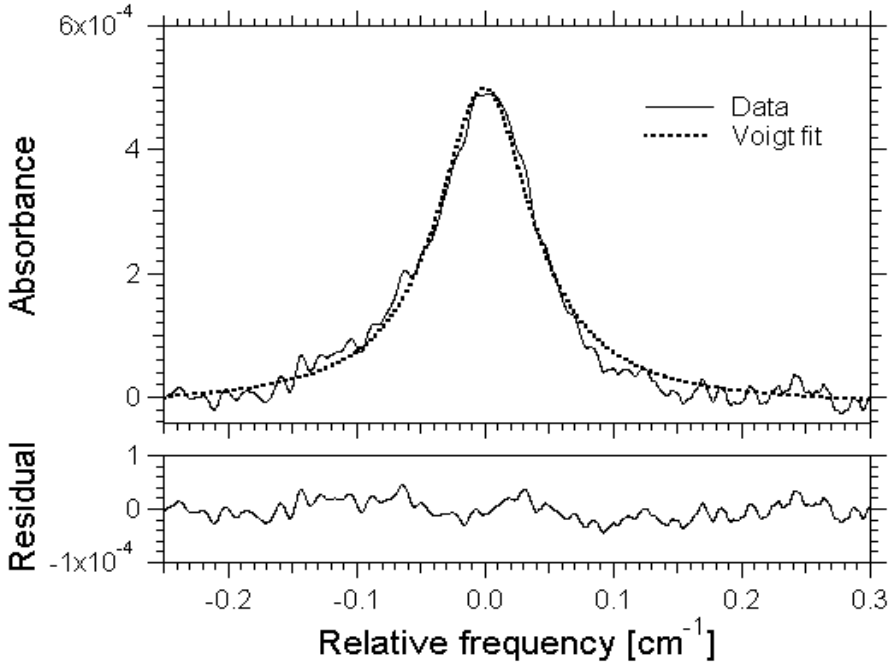

Figure 4.7 Measured CO lineshape (R(15) transition, 50-sweep average) recorded in the exhaust duct (X_{CO} = 22 ppm, ϕ = 0.97, T ~ 470 K, L = 120 cm).

Figure 4.7 presents a 50-sweep-averaged (0.1-s total measurement time) lineshape for 22-ppm CO (ϕ = 0.97) recorded with a detection bandwidth of 50 kHz. The raw data trace was least-squares fit to a Voigt profile to yield the numerator integral in Eq. (4.2). From the residual of the best-fit Voigt profile, the noise-equivalent absorbance was estimated to be ~3×10^{-5}, which

corresponded to a ~1.5 ppm-m detectivity. Averaging of more sweep times did not improve the detectivity, possibly because of the drift of the experimental condition.

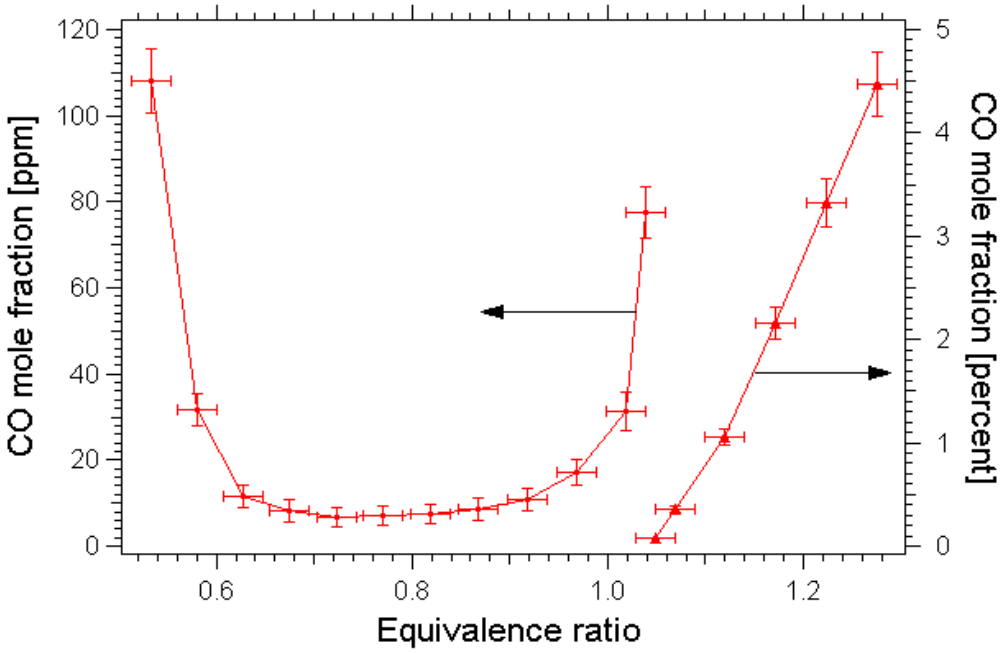

Figure 4.8 Measured CO concentrations recorded using direct-absorption spectroscopy in the exhaust duct (T~470 K, P=1atm) as a function of equivalence ratio.

Figure 4.8 presents the measured CO concentration in an equivalence-ratio range of 0.53-1.27. The CO concentration decreases as the equivalence ratio is reduced until the flame becomes unstable at very lean conditions. For equivalence ratio less than 0.6, the CO concentration was observed to vary significantly with time (inset of figure 4.11) because of combustion instabilities. The smallest CO mole fraction (6.7 ppm) was measured at ϕ = 0.72. At this condition, the signal-to-noise ratio is approximately 5. The main measurement uncertainty at low concentration conditions is due to the difficulty in obtaining correct baselines for these atmospheric-pressure-broadened lineshapes. Although a balanced-detection strategy (i.e., differential absorption) works well for static-cell measurements, it is less suitable for measurements in combustion environments due to inherent beam steering. One alternative is to increase the beam path by multi-passing. Another approach is to employ a variation of absorption with enhanced sensitivity.

4.5.2 Wavelength-modulation spectroscopy

WMS was selected as a means of increasing the sensitivity of CO measurements (figure 4.9). While the laser mean frequency $\bar{\nu}$ was tuned over the CO R(15) transition by a 50-Hz ramp current modulation, a 33-kHz (f) sinusoidal dither of the injection current was used to obtain wavelength modulation. A lock-in amplifier was used to measure the second-harmonic component of the transmitted laser signal. The time constant of the lock-in amplifier was set to 300 μs.

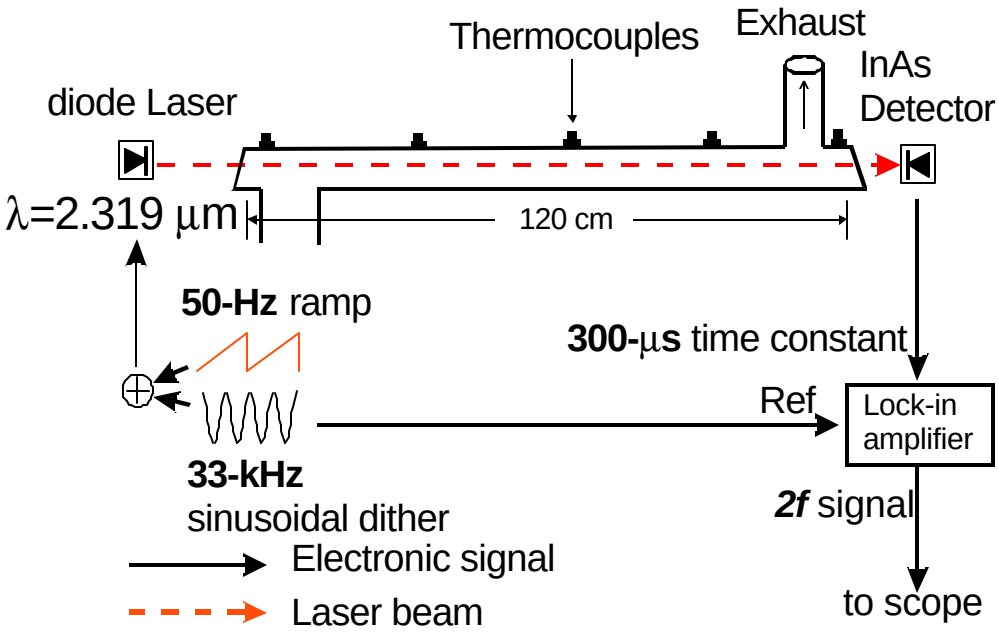

Figure 4.9 Schematic diagram for CO measurements in the exhaust duct using WMS techniques.

Figure 4.10 presents representative lineshapes (20-sweep average) recorded at equivalence ratios of 0.72 and 0.95. The amplitude of the wavelength modulation a was intentionally set to a relatively small value such that the modulation index was ~1.46 (a weak function of equivalence ratio) to reduce the interference from a nearby transition (~0.41 cm^{-1} away, ~4311.55 cm^{-1}). This transition was observed in a heated static cell filled with H_2O and thus was verified to be a transition of H_2O or its isotopes. It is well known that smaller modulation index gives smaller lineshape broadening, which results in smaller H_2O interference, although the signal amplitude is also sacrificed. The effect of this H_2O line was calculated to be less than 1% for 1-ppm CO concentration at a modulation index of 1.46. For the data traces in Figure 4.10 the signal-to-noise ratio was estimated to be approximately 100, which corresponded to a detection sensitivity of ~0.1 ppm-m for a measurement repetition rate of 2.5 Hz.

The achieved detectivity is far better than that required for combustion emission-compliance monitoring. It also enables ambient-air quality monitoring, on-road remote sensing of vehicle exhausts, etc. Therefore, some experiments for these applications were quickly designed to take advantage of this good detectivity. Unfortunately, the laser stopped lasing while we were preparing for these experiments.

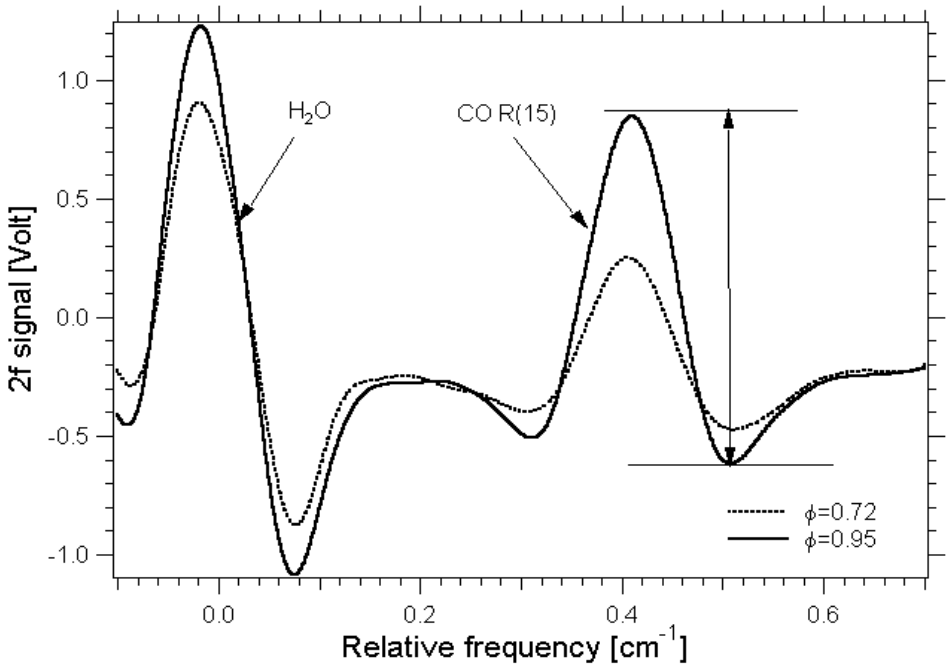

Figure 4.10 Representative 2*f* lineshapes (~1.46 modulation index, 20-sweep average) for CO measurements in the exhaust duct.

The CO concentrations were determined from the height of the peak relative to the right-wing valley (Figure 4.10). This simple approach was justified by the high signal-to-noise ratios, although it may be better to fit a recorded trace to a matched filter (Riris *et al*. 1994) for low signal-to-noise conditions because it exploits the information of all data points rather than only the data points at the peak. The 2*f* signals were calibrated by matching the measured 2*f* signal to the directly measured absorbance at $\phi = 1.07$, ~850 ppm CO, for this case. During the calibration measurements, a 10% fluctuation of the 2*f* single-sweep measurement was observed, which was likely due to fluctuations in the input C_2H_4 flow to the burner. For a 20-sweep average, the total uncertainty of the calibration measurement was estimated to be about ±7%, including the ±5% uncertainty of the direct absorption measurement.

Since the CO concentration was determined from the signal peak height through a calibration procedure, the deviation of gas-mixture temperature and composition from the calibration conditions needs to be compensated as explained in the chapter 2. This deviation affects the linestrength and the Doppler linewidth through temperature and the collisional linewidth through temperature and mixture composition. Physically, the effect of linewidth variation on the peak-to-valley height of the 2*f* signal is two-fold through both the linecenter absorbance and modulation index (see Eq. (2.29)). The temperature dependence of the linestrength and Doppler broadening can be obtained from Eq. (2.16) (also see Figure 4.4) and Eq. (2.10), respectively. The collisional-broadening coefficients and their temperature dependences of CO for various perturbing species have been extensively investigated both experimentally and theoretically (Bouanich and Brodbeck 1973; Hartmann *et al.*1988; Rosasco *et al.* 1989; Varghese and Hanson 1981). The collision-broadening coefficients and their corresponding temperature exponents for the R(15) transition used in our correction calculations are tabulated in Table 4.3. For absorption with a general Voigt lineshape, there is no simple explicit equation to relate the 2*f* signal to the Doppler linewidth and the collisional linewidth. Therefore, numerical calculation of Eq. (2.22) was performed to correct the effect of linewidth variation. For our exhaust-duct measurements, the largest correction was 8.2% at the leanest condition (ϕ = 0.63).

Figure 4.11 presents the measured CO concentrations recorded using wavelength-modulation spectroscopy techniques. For 2*f* measurements, the signal-to-noise ratio was generally ~100 and the interference from the nearby H_2O line was less than 1%. The uncertainty associated with the correction for gas composition and temperature variations was estimated to be less than ±2%. Thus the calibration procedure was the dominant source of uncertainty (±7%). At very lean conditions, the flame becomes unstable and eventually blows out. This flame instability is manifested in the variation of CO concentrations (inset of Figure 4.11) that were recorded using wavelength-modulation spectroscopy with 100-Hz measurement repetition rate. No averaging was used in this measurement. The flow residence time of the experimental setup was characterized to be 2.8 s by measuring the response time of CO concentrations to a step change of the equivalence ratio (figure 4.12). Because of this relatively large flow residence time, only the low-frequency (<1 Hz) variation was revealed.

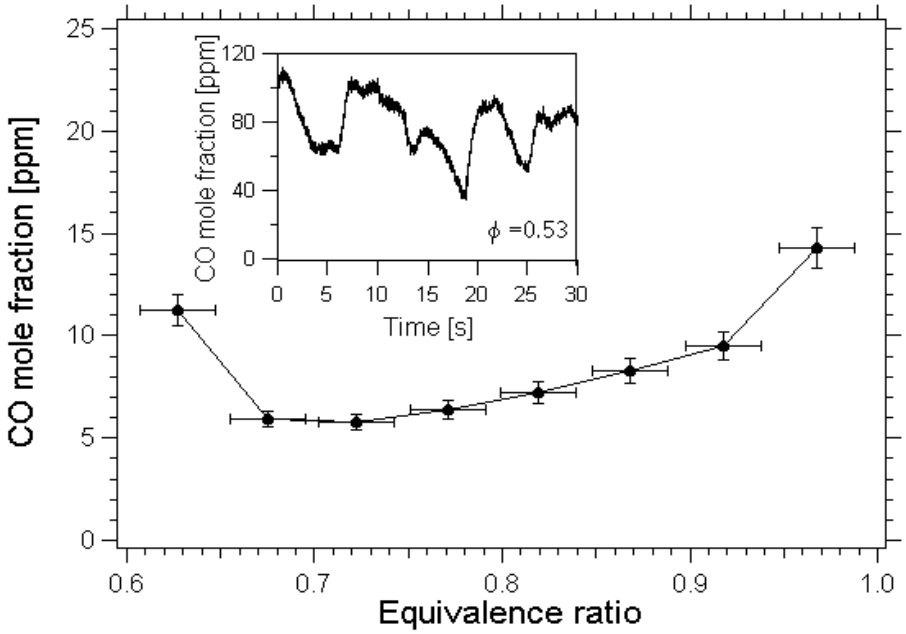

Figure 4.11 Measured CO concentrations in the exhaust duct using wavelength-modulation spectroscopy (2*f*) techniques (2.5-Hz measurement repetition rate). The inset shows the time variation of CO concentration (ϕ=0.53) recorded with 100-Hz measurement repetition rate.

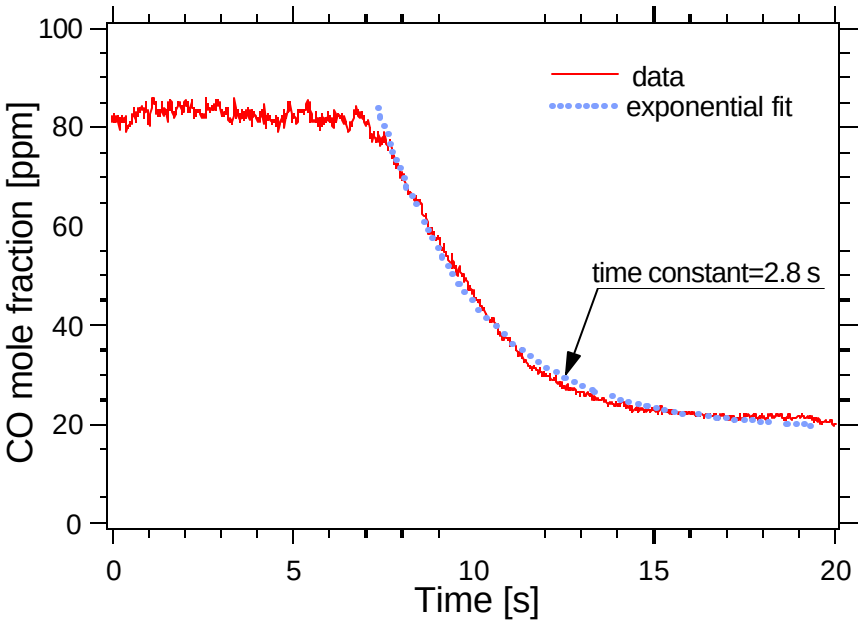

Figure 4.12 Time evolution of the CO concentration subject to a step variation of equivalence ratio.

One interesting observation was that a C_2H_4 feature was detected (Figure 4.13) when the burner operated in the near-blowout condition. At this operating condition, many small flamelets rather than a flat flame were visually observed near the burner surface and these flamelets did not cover the burner surface near the burner edge. This spatial nonuniformity as well as lower flame temperatures likely causes the much larger leakage of C_2H_4 fuel than in the normal operation conditions.

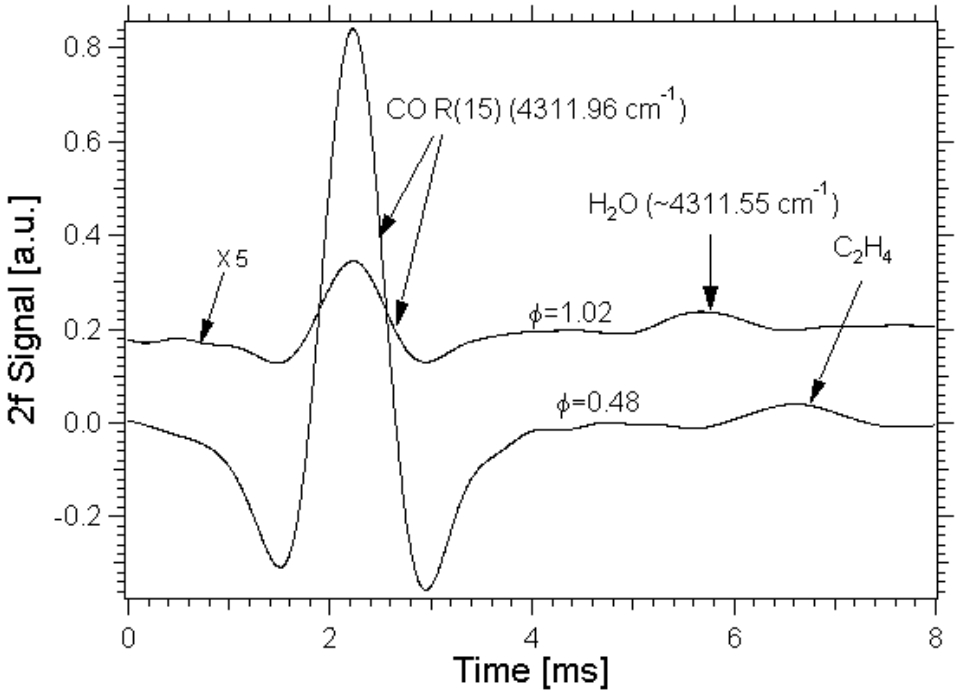

Figure 4.13 A C_2H_4 feature was observed in the measured 2*f* trace recorded in the exhaust duct at near-blowout condition (ϕ=0.48). The trace recorded at ϕ=1.02 condition (amplified by 5 and shifted in DC level) was used to provide the reference frequency frame.

4.6 Measurements in the flame

Figure 4.14 presents measured radial temperature profiles in the immediate post-flame zone (1.5 cm above the burner surface) at three different equivalence ratios (0.82, 1.02, and 1.33). The biggest core region with relatively uniform temperature was observed for the richest flame. The largest temperature fluctuation occurred at the interface of the shroud and combustion sections as expected.

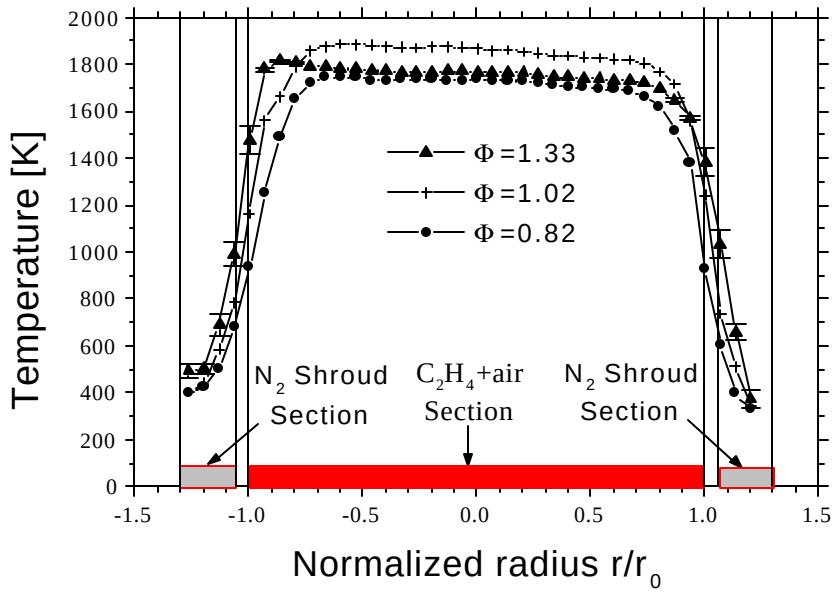

Figure 4.14 Radial thermocouple-temperature (uncorrected) profiles measured 1.5 cm above the burner surface for various equivalence ratios.

Figure 4.15 presents a 50-sweep-averaged lineshape (0.1-s total measurement time) of the CO R(30) transition recorded 1.5 cm above the burner surface at an equivalence ratio of 0.83. Since absorption spectroscopy yields an integrated line-of-sight measurement, the effect of flame nonuniformity (temperature (Figure 4.14) and CO concentration) near burner edges has to be considered. Because the goal of this work is to demonstrate the capability of *in situ* CO measurements in high-temperature combustion environments, no particular effort was taken to reduce this nonuniformity. This cool-edge effect has been studied previously (Schoenung and Hanson 1981) by using an extractive probe and a thermocouple to measure the transverse CO concentration and temperature profiles. To find CO concentrations in the relative uniform core region, an "effective" path length L_{eff} can be introduced to account for the edge effect:

$$\left(X_{co}S\right)_{core} P L_{eff} \equiv \int_0^L X_{co}(x) PS(x) dx. \qquad (4.3)$$

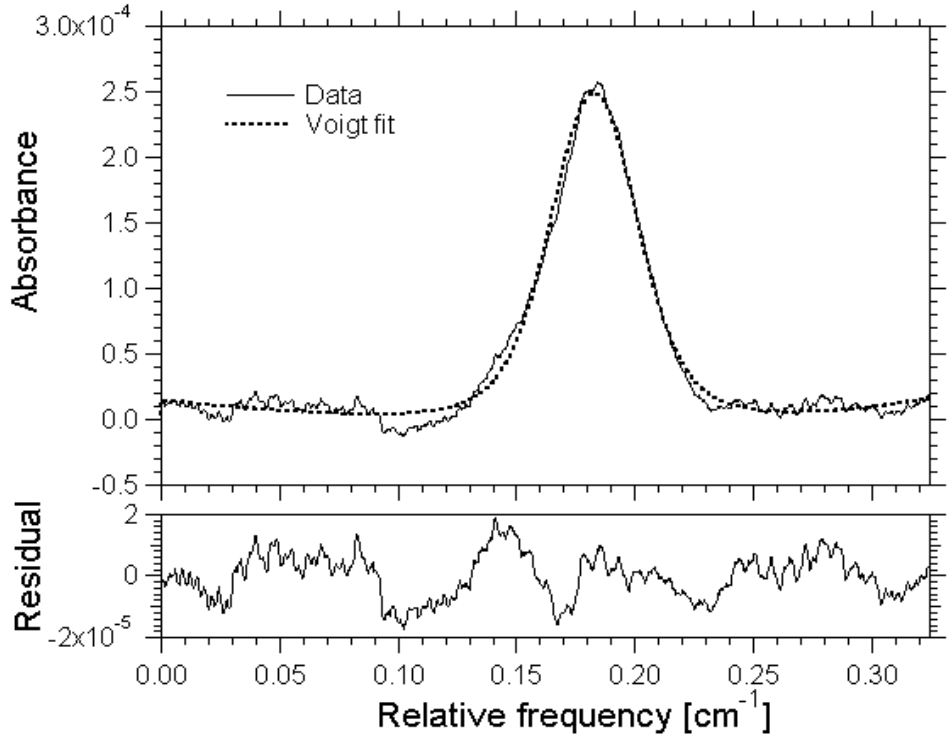

Figure 4.15 Measured CO lineshape (R(30) transition, 50-sweep average) recorded 1.5 cm above an atmospheric-pressure flat-flame burner (ϕ=0.83, X_{CO}=366 ppm, T_{core}=1820 K, P=1 atm, L=11.4 cm).

Combining Eq. (2.19) and Eq. (4.3), the CO concentration in the core region can be expressed as:

$$(X_{co})_{core} = \frac{\int_{\nu} [-\ln(T(\nu))] d\nu}{PS_{core}\left(\frac{L_{eff}}{L}\right)L}. \qquad (4.4)$$

The numerator integral was obtained by fitting the recorded lineshape with a Voigt profile (Figure 4.15). For fuel-rich flames, the cool edges lead to lower equilibrium levels of CO while for fuel-lean flames the CO levels peak at the edges because of low temperatures which slow the oxidation of CO (low OH concentration and reaction rate, equilibrium may not be achieved). Thus, the ratio of L_{eff} to the physical burner dimension, L, is smaller than unity for fuel-rich flames while larger than unity for fuel-lean flames. This ratio varies very slowly for fuel-rich flames while sharply for fuel-lean flames (Schoenung and Hanson, 1981). Radiation-corrected thermocouple temperature recorded in the core region was used to calculate the S_{core}.

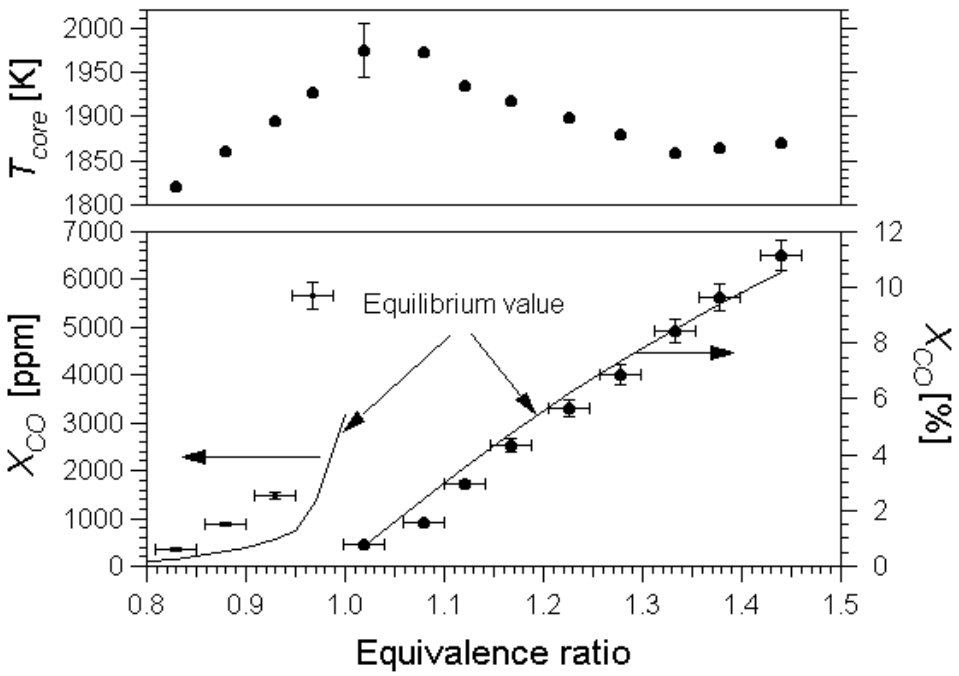

Figure 4.16 Measured CO concentration and radiation-corrected thermocouple temperature recorded 1.5 cm above an atmospheric-pressure premixed (C_2H_4-air) flat-flame burner as a function of equivalence ratio.

Measured CO concentrations and radiation-corrected thermocouple temperatures of the core region are shown in Figure 4.16 for a range of equivalence ratios (ϕ = 0.83–1.44). The ratio L_{eff}/L in Eq. (4.4) for all data points in the fuel-rich flames was chosen to be 0.72 to normalize the data point at ϕ=1.35 to the theoretical equilibrium value. The radiation-corrected thermocouple temperatures ranged from 1820 to 1975 K. The largest temperature correction was 98 K at the equivalence ratio 1.02. The estimated uncertainty of this correction, ±30 K, was primarily due to uncertainties in Nusselt number, mixture thermal conductivity and bead emissivity. Because of the small temperature sensitivity of the linestrength of the R(30) transition (Figure 4.4), the uncertainty of measured concentrations was smaller than ±2% due to this temperature uncertainty. The measured CO concentration agreed well with predicted equilibrium values. Since the ratio L_{eff}/L in the fuel-lean flames varies sharply with equivalence ratio, it was simply set to unity here. The measured CO concentrations in the fuel-lean flames were higher than equilibrium predictions because of the cool edge effect and possibly the superequilibrium condition.

This high-temperature *in situ* sensor is well suited for combustion control. Since the time delay between the sensor and actuators is very short due to the close location of the sensor to the flame, quick and stable feedback control can be realized. Another important potential application is motor-vehicle-engine diagnostics such as dynamic exhaust gas analysis with single-cycle time resolution. In the U.S., motor-vehicle exhaust contributes about 60 percent of national total CO emissions, while in cities as much as 95 percent of CO emissions may emanate from motor-vehicle exhaust (US EPA Office of Air & Radiation). The requirements for cleaner air will continue to push the motor-vehicle industry to reduce exhaust emissions. The *in situ* capability, high sensitivity, and fast time response of our sensor may be valuable in research and development by motor-vehicle manufacturers to meet more stringent regulations in the future.

Although not shown in figure 4.16, some measurements were also made in the very lean flames until the flame became visibly unstable. Even for the measurement at the lowest equivalence ratio 0.62, a clear CO absorption feature was observed, together with some interference features. However, in order to obtain quantitative results, longer beam path and detailed study of the H_2O and CO_2 spectra in this region are required. The H_2O spectra predicted by the HITEMP database cannot explain the observed interference. The fuel C_2H_4 also strongly absorbs in this wavelength range (Brock *et al.* 1994). Because of the close location of the laser beam to the burner surface, some C_2H_4 may not have reacted and likely contributed to the observed interference. However, this possible interference by C_2H_4 absorption is much less fundamental than H_2O or CO_2 absorption. Some of the interference may also originate from tuning through strong H_2O and CO_2 lines by the laser side modes. Further investigation is required to resolve this issue in order to extend the detectivity to below one hundred ppm for other applications such as gas turbine diagnostics. Two lasers were able to get access to the R(30) transition and were used to do the above preliminary study. The first stopped lasing after measurements in the fuel-rich region. The second was then used to do the measurements in the fuel-lean conditions. Unfortunately, before we could implement a relative systematic study on the abovementioned issues, the single-mode operating region drifted away from the R(30) transition.

4.7 Discussions

Both H_2O and CO_2 have a transmission window ranging from 2.1 μm to 2.4 μm (figure 4.1). In addition, diode lasers within this wavelength range can be operated near room temperatures. Therefore, this wavelength range is particularly attractive for absorption gas sensing. Some very important species, e.g., ethylene (C_2H_4) and ammonia (NH_3), have relatively strong transition in

this wavelength range. Diode-laser absorption sensing of ammonia is of particular interest. Since ammonia is very sticky and a significant amount may be lost during the sampling process, the *in situ* measurement capability offered by diode-laser absorption sensing is very attractive. Absorption sensing of ammonia has been actively investigated near 1.5 μm (e.g., Modugno and Corsi 1999). However, due to the strong interference of H_2O and CO_2 there, it is relatively difficult to achieve sensitivity at ppm level. In contrast, many ammonia transitions near 2.2 μm are isolated from H_2O and CO_2 interference (figure 4.17), and thus 2.2-μm absorption sensing of ammonia is very attractive and promising. Professor Tittel's group in Rice University is currently pursuing this approach (private contact). The 2.2-μm diode laser they have is still of FP structure and operates multimode, but it has much better reliability than ours.

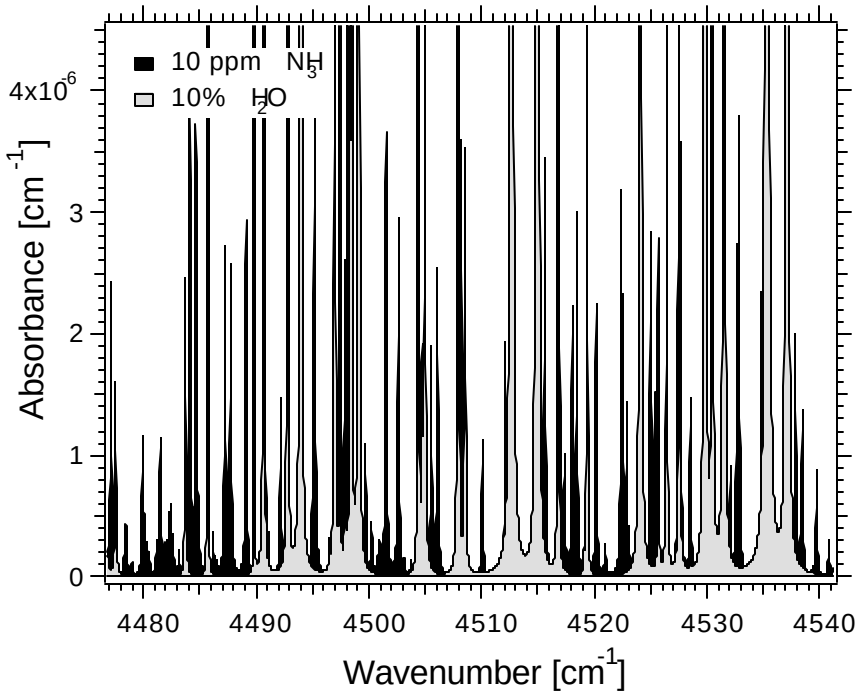

Figure 4.17 Calculated spectra of H_2O (10%) and NH_3 (10 ppm) at 500 K, 1 atm based on HITRAN96 parameters. CO_2 interference is negligible.

Room-temperature GaSb-based VCSELs operating near 2.2 μm have been successfully demonstrated (Baranov *et al.* 1998). For VCSELs, single-mode operation can be achieved by restriction of the lateral dimension, unlike edge emitters, which require much more extensive processing to obtain the grating structures. Furthermore, the small active volume of VCSELs allows much smaller injection current than edge emitters. Finally, it is relatively straightforward

to obtain the high-reflectivity DBRs in this wavelength range with the AlAsSb-GaSb quarterwave stacks. Therefore, VCSEL structures may be the best way to obtain low-cost single-mode lasers in this wavelength range for high-resolution absorption sensors.

Chapter 5. *On-road Remote Sensing of CO in Vehicle Exhaust*

In the last chapter a CO exhaust sensor using the R(15) transition of the first-overtone band was demonstrated to have a sensitivity of 0.1 ppm-m even with a relatively low modulation frequency (33 kHz). This sensor qualifies for emission compliance monitoring of stationary sources such as municipal waste combustors. The New Source Performance Standards (NSPS) regulates a maximum CO emission between 50 and 150 ppm, depending on specific combustor configuration. The sensitivity is even sufficient for ambient-air quality monitoring, since the most stringent regulation by National Ambient Air Quality Standards (NAAQS) allows a maximum CO concentration of 9 ppm over an 8-hour averaging time. Finally, with the sensitivity demonstrated, the sensor can also be used for on-road remote sensing of CO in vehicle exhaust, the largest CO source. This chapter investigates the feasibility of this last application.

5.1 Motivation

In the USA transportation sources account for more than 70% of the total CO emissions nationally, while in cities as much as 95 percent of CO emissions may emanate from automobile exhaust (US EPA Office of Air & Radiation). The long atmospheric lifetime of CO (~1 month) allows transport to spread these emissions. Although the 38% reduction of ambient CO concentration between 1988 and 1997 reflects the considerable reduction in emission from automobiles, the improvements are not nearly as large as had been anticipated and some serious defects have been identified in current vehicle inspection and maintenance (I/M) programs (Calvert *et al.* 1993). Because approximately 50% CO is emitted by 10% of the vehicle fleet, on-road remote sensing devices (RSD) are considered to be an especially attractive I/M tool to supplement current I/M programs and to focus resources on gross polluters (Calvert *et al.* 1993; Cadle *et al.* 1999; Bishop *et al.* 1993). In addition, RSD can improve vehicle emission inventories (Cadle *et al.*1998, 1999), which air pollution control agencies use to identify the most cost-effective control measures, to determine control program effectiveness, and to predict future air quality through use of simulation models. Data from RSD can also be used to assess the real rather than computer-modeled effectiveness of control measures (Bishop *et al.*1993). Therefore, RSD is an important part of strategies implemented by the USA's Environmental Protection Agency (EPA) and states to reduce emissions from motor vehicles (U.S. EPA Office of Mobile Sources 1993).

Infrared-absorption sensors have the potential for real-time remote sensing of CO emissions from vehicles. Non-dispersive infrared (NDIR) analyzers have been fielded with an accuracy of ±1% CO in the vehicle exhaust, sufficient to identify gross CO emitters where threshold concentrations are typically set to several percent (Bishop *et al.*1989; Cadle *et al.*1994; Stephens and Cadle 1991). However, the NDIR detection limit is not sufficient to quantify the low emission levels of most vehicles. Before catalytic converters reach operating temperature, even clean vehicles may emit several percent CO, and the current NDIR measurement strategies must carefully choose monitoring locations to minimize the number of these cold-start vehicles in the monitored fleet. Tunable diode laser absorption spectroscopy (TDLAS) sensors developed in the last chapter have much larger dynamic range, faster time response, and potentially the high sensitivity required to characterize even the cleanest combustion-powered vehicles. In addition, these sensors have the potential to identify cold-start vehicles.

As shown in figure 4.1 and discussed in section 4.1, sensors using transitions of the second-overtone band near 1.55 μm suffer strong interference from H_2O and CO_2. The weak linestrength, together with the interference, limits the detection limit of commercial TDLAS on-road remote CO sensors using a second-overtone transition to ±0.25% CO (MD-Lasertech LTD). TDLAS instruments using strong transitions in the fundamental band have been demonstrated for open-path CO measurements (Ku *et al.* 1975) and on-road remote sensing of NO (Nelson *et al.* 1998; Jimenez *et al.* 1999). Although these instruments have much better performance than the NDIR devices, the lead-salt diode lasers used in these instruments are relatively difficult to use as they require cryogenic cooling and generally operate multi-mode.

Last chapter demonstrated sensitive *in situ* CO detection using first-overtone transitions to probe the exhaust of a laboratory flame. A detection limit of ~0.1 ppm-m with a measurement repetition rate of 2.5 Hz has been demonstrated. In this chapter the potential of applying this new CO-sensing strategy to on-road remote sensing of vehicle exhausts is examined. The influence of the large temperature range of vehicle exhausts has been neglected in previous work on remote sensing. This thesis explores a temperature-insensitive strategy for CO remote sensing. The temperature influence is further exploited to suggest a screening strategy for cold-start vehicles.

5.2 Measurement principle

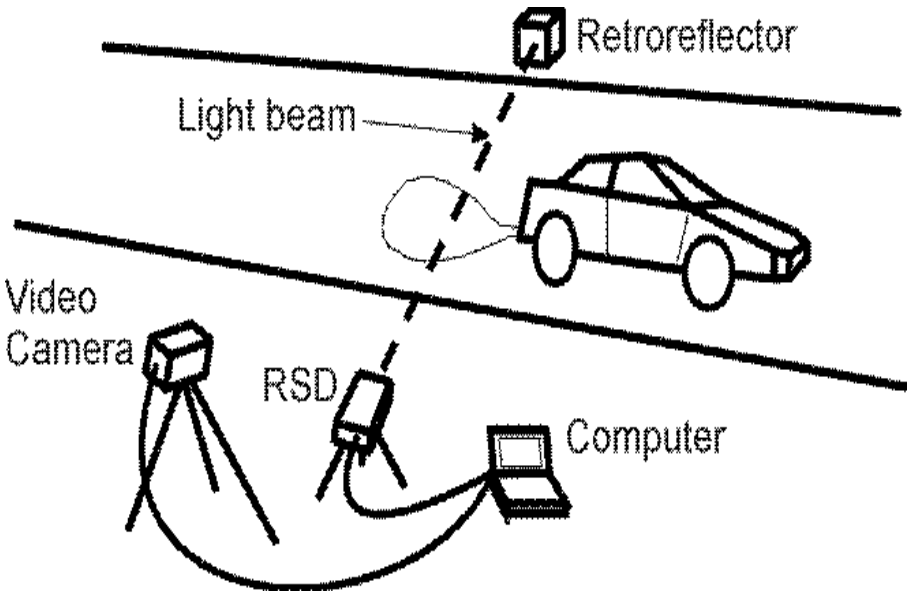

Figure 5.1. Schematic diagram of on-road remote sensing of vehicle exhaust.

Absorption of light resonant with CO or CO_2 transitions is measured for a laser beam continuously directed across a roadway to either a detector or a retroreflector (figure 5.1). A retroreflector simplifies the alignment in the field and reduces the complications of beam steering arising from turbulence. When the laser wavelength is tuned through the resonance, the attenuation of laser intensity is proportional to the column density of absorption species. The CO/CO_2 ratio rather than the absolute column density of CO is measured for the remote sensing of CO in vehicle exhausts. The use of CO_2 as a reference allows quantitative measurements of CO without knowing how much the exhaust has mixed with ambient air. Typically the column densities of CO and CO_2 are measured for half to one second after a passing vehicle triggers the sensor to yield an average CO/CO_2 ratio. This average ratio is then converted to the CO concentration in the vehicle exhaust if the fuel composition is known. This ratio is sufficient to determine the fuel-specific emission index:

CO (g/gallon)=Fuel Density (g/gallon)×Carbon weight fraction (g-C/g-fuel)×Q/[1+(1+*c*)Q]×
28/12 (g-CO/g-C),

where Q is the measured CO/CO_2 ratio, *c* is a statistical constant to consider carbons in unburned hydrocarbons. By simultaneously capturing video images of vehicles' license plates, the measurements are linked to each individual vehicle. If divided by a statistical fuel economy (mile/gallon) based on the vehicle's year of production, make and model (Stephens and Cadle

1991), this fuel-specific emission index is converted to the commonly used gram-per-mile emission index for mobile sources. However, the gram-per-gallon emission index, which is independent of roadway grade, is considered a more stable basis for modeling than the gram-per-mile emission index (Pierson *et al.* 1996). Emission data from these one-second measurements can yield an accurate inventory of emissions and identify highly-emitting vehicles with extremely low errors of commission and modest errors of omission (Stephens *et al.* 1996).

The wavelength-modulation spectroscopy (WMS) technique is preferred for on-road remote sensing because of its high sensitivity, robustness, and simplicity. The well-structured absorption spectra of CO and CO_2 at atmospheric pressure are well suited for WMS. Infrared emission from hot exhausts and scattering by particulate matter were identified as problems in previous on-road measurements with NDIR devices (Stephens and Cadle 1991) and these problems are avoided by using WMS. With these NDIR devices, wide-band radiation at 4.6 and 4.3 μm was used to measure column densities of CO and CO_2, respectively; and a 3.9-μm light beam was employed to track the light-intensity fluctuations from the light source, beam steering, and particulate scattering. Although this can be an effective strategy, wavelength-dependent scattering can introduce errors. However, with WMS second-harmonic ($2f$) detection techniques, the effects of light-intensity fluctuations and slow drift of optical alignment can be easily compensated by dividing the $2f$ signal by the "dc" component of the same transmitted signal (see chapter 2). With this self-compensation, the instrument can also be rendered nearly free of in-field calibration. In addition, the essentially monochromatic laser radiation used for WMS allows infrared radiation from hot exhausts and other sources to be blocked by spectrally narrow bandpass filters.

5.3. Spectral interference from other species

For accurate measurements, the probed spectral features should be relatively strong and isolated from spectral interferences by other species present in the probed air column. Most spectral interferences in the wavelength region of CO first overtone band are due to water vapor. Several other species such as NH_3, CH_4, and C_2H_4 existing in vehicle exhausts also absorb in this wavelength region, but their concentrations are generally much smaller than the concentration of CO and their linestrengths are comparable or lower than those of strong transitions of CO. Therefore, these species do not pose serious interference problems.

The temperature and composition of an exhaust plume varies from those of the hot combustion exhaust to those approaching ambient air as dispersion proceeds. Good candidate transitions

should be free from interference at all conditions. As illustrated in figure 4.2, at 500 K and 1 atmosphere, free of interference from H_2O with relatively strong linestrengths are P(8) (not shown), R(4), R(6), R(10), R(11), R(15), R(19), and R(20). The survey spectra of CO (5 ppm) and H_2O (5%, corresponding to 80% relative humidity at 310 K) at 300 K and 1 atmosphere are similarly calculated to simulate the ambient air condition with almost the largest ambient H_2O content. The same transitions are also free from H_2O interference at this condition and thus are good candidates for CO measurements.

5.4. Temperature and composition effects

For WMS measurements of vehicle exhaust, a Lorentzian absorption lineshape can be assumed. Therefore, the column density (XL) of CO or CO_2 (expressed as [CO] or [CO_2] in this chapter), is inferred explicitly from (see chapter 2):

$$XL \propto \frac{P_{2f}\,\Delta\nu}{I_0 S}\left[\frac{2}{m^2}\left(\frac{2+m^2}{(1+m^2)^{1/2}}-2\right)\right]^{-1}, \tag{5.1}$$

where P_{2f} is the measured peak $2f$ signal at the linecenter ν_0; I_0 is the incident laser intensity; S [$cm^{-2}atm^{-1}$] and $\Delta\nu$ [cm^{-1}] are the linestrength and collisional linewidth (HWHM) of the probed transition, respectively; and m is the modulation index. Therefore, the measured column density depends on the transition linestrength and linewidth, both of which vary with temperature. The collision-broadened linewidth also depends on the composition of exhaust plume.

Vehicle-exhaust temperatures vary significantly depending on vehicle model and operating conditions such as load and speed. Relatively high exhaust temperatures (~700 K) were reported for a normal-load vehicle at a speed of 40 miles per hour (Nebel 1964). All previous remote-sensing measurements assume vehicle exhausts quickly disperse in the air and cool down to ambient temperature and thus neglect the temperature effect. However, we expect that remote sensors will be required to measure exhaust emissions under some important real-world driving conditions, such as in traffic jams and at stop signs, to improve emission inventories, so neglecting temperature effects may lead to significant errors under these conditions. For one-second concentration measurements, the temperature is generally nonuniform along the path of the laser beam through exhaust plumes and thus the normal approach of using the linestrength at the path-averaged temperature measured by two-line absorption thermometry to determine the column density is not appropriate here. In addition, the generally nonuniform and unknown

plume composition also poses problems for the utilization of WMS techniques which generally need accurate linewidth information to infer the column density.

A new approach that matches the temperature and composition dependences of CO and CO_2 measurements and thus obtains temperature- and composition-independent measurements of the CO/CO_2 ratio is proposed here. By selecting the absorption transitions for CO and CO_2 measurements as described below, the CO/CO_2 ratio can be accurately determined to within ±3% in the temperature range 300-700 K.

First we consider the influence of temperature on the inferred CO/CO_2 ratio through linestrength for a differential plume section of uniform temperature T in the laser beam path. The measured CO column density with transition k, $[CO]_{meas}$, of this section is related to the true column density $[CO]$ by

$$[CO]_{meas} = [CO] S_k(T) / S_k(T_{ref}), \tag{5.2}$$

when the linestrength ($S_k(T_{ref})$) at a reference temperature (300 K in this chapter) rather than the true linestrength ($S_k(T)$) is used in equation (5.1) to infer the column density. Assuming that the column density of CO_2 is measured by two CO_2 transitions i and j, and a linear combination of the two measured CO_2 column densities, $[CO_2]_i$ and $[CO_2]_j$, is used to yield a final measured column density, we have

$$[CO_2]_{meas} = a[CO_2]_i + b[CO_2]_j = [CO_2]\left[a S_i(T)/S_i(T_{ref}) + b S_j(T)/S_j(T_{ref})\right], \tag{5.3}$$

where $[CO_2]$ is the true column density, a and b are constants (not necessary positive) satisfying $a + b = 1$. Therefore, the measured CO/CO_2 ratio is

$$\frac{[CO]_{meas}}{[CO_2]_{meas}} = \frac{[CO]}{[CO_2]}\left[\frac{S_k(T)/S_k(T_{ref})}{a S_i(T)/S_i(T_{ref}) + b S_j(T)/S_j(T_{ref})}\right] = \frac{[CO]}{[CO_2]} F(T) \tag{5.4}$$

If the transitions i, j, k for CO_2 and CO measurements and the constants a and b can be chosen so that the term (called temperature factor, $F(T)$, in this chapter) within the bracket is unity for any temperature T within the typical exhaust-gas temperature range, the measured $[CO]/[CO_2]$ ratio for this differential section will represent the true ratio. Because of the arbitrariness of the differential section, the ratio of path-integrated column densities will also be the true one.

Figure 5.2 shows the temperature dependences of linestrengths of several CO first overtone transitions free from H_2O interference in the typical temperature range of exhaust gas. The linestrength of the R(15) transition has the smallest temperature sensitivity and has been

experimentally verified to be free from H_2O interference (see chapter 4). Therefore, the R(15) transition is well suited for the CO measurement. CO_2 transitions will be chosen to match the temperature variation of the linestrength of the CO R(15) transition.

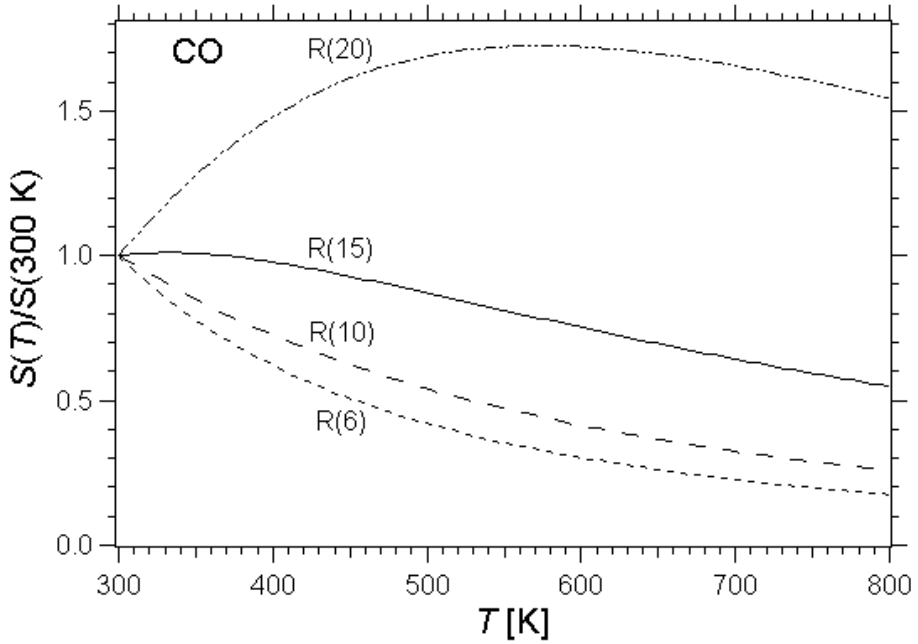

Figure 5.2 Temperature dependence of the normalized linestrengths of several CO transitions (2v band) free from H_2O interference.

Recently available 2-μm room-temperature distributed feedback (DFB) diode lasers can provide both a high signal-to-noise ratio and convenience of operation by accessing the strong $v_1+2v_2+v_3$ band and have been demonstrated successfully in our laboratory for combustion diagnostics (Webber *et al.* 2000). In this wavelength range, the interference from H_2O transitions in the exhaust-plume temperature range is also small. In addition, these lasers offer the possibility of multiplexing with 2.3-μm lasers for measurements of CO in a single-mode optical fiber. However, the following calculation can be used to choose CO_2 transitions in any band (e.g., 1.6 μm, 2 μm, and 4.3 μm). Since the upper states of these CO_2 rovibrational transitions are rarely populated in the temperature range considered here, the normalized linestrengths of CO_2 transitions depend only on their lower-state rotational quantum numbers (J¢¢) and thus CO_2-transition numberings i and j in equation (5.4) simply correspond to J¢¢.

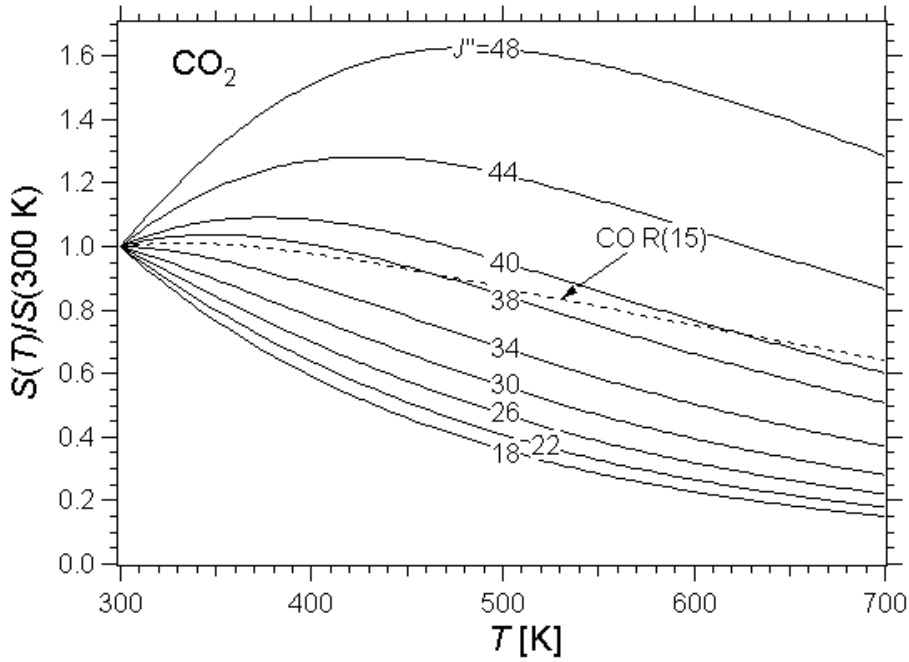

Figure 5.3 Temperature dependence of the normalized linestrengths of the CO R(15) transition and some CO_2 transitions.

Figure 5.3 presents the calculated temperature dependence of some CO_2 transitions. HITRAN96 parameters for the lower-state energy and the partition function were used in the calculation. If only one CO_2 transition is used (the case of b=0 in equation (5.4)), the temperature characteristic of R(40) or P(40) transitions best matches that of CO R(15) (to within ~10%) in the temperature range 300-700 K, while R(38) or P(38) matches best (to within ~3%) in the temperature range 300-500 K. If two CO_2 transitions are used, better performance can be obtained and the selection of CO_2 transitions is very flexible. This flexibility allows possible selection of the CO_2 transition pair considering other important factors such as H_2O interference and laser availability. Figure 5.4 presents the temperature factors for the best single transition ($J"$ =38 or 40) and several two-transition configurations. For each CO_2 transition pair, the linear combination constants a and b in equation (5.4) are chosen to minimize the temperature effect. With judicious choice of the transition pair and linear combination constants for CO_2 measurements, the temperature factor remains within ±3% of unity in the temperature range 300-700 K.

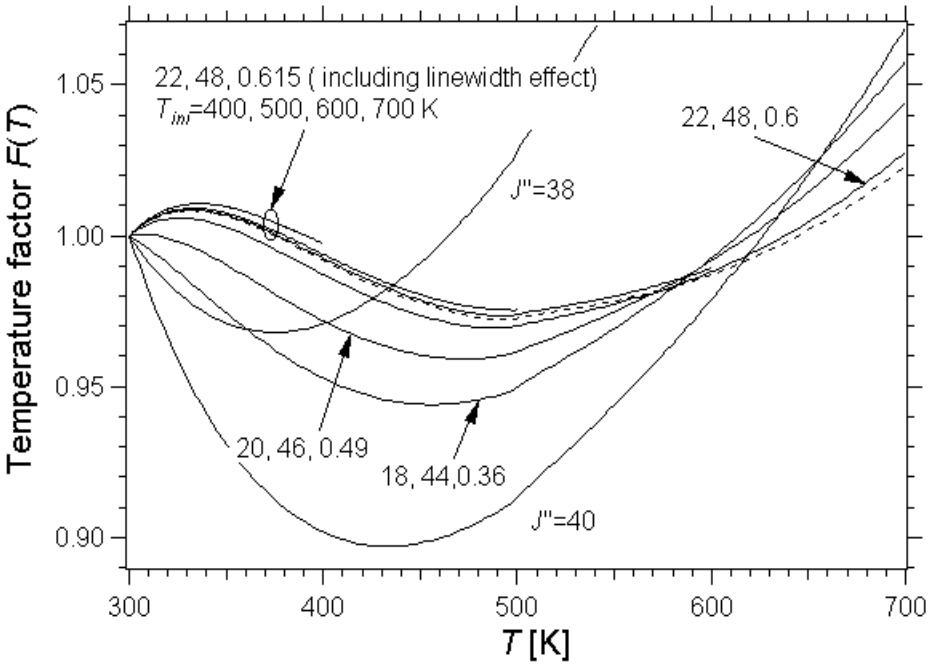

Figure 5.4 Calculated temperature factors for the best single-transition (J''=38 or 40) and some two-transition CO_2-measurement combinations. The sets of numbers are i, j, a in equation (5.4) or (5.5), where i, j are simply the lower-state rotational quantum numbers for the CO_2 transition pair, and a is chosen to minimize the temperature effect. Linewidth effects are only considered in the (22,48, 0.615) case with different initial exhaust-gas temperatures (T_{ini}).

The discussion has thus far neglected the influence of the linewidth on measurements of the CO/CO_2 ratio. The linewidth variation with the temperature and composition is analyzed in the following. The total collisional linewidth may be obtained by summing the broadening contributions from all components in the exhaust plume and a simple power law can be used to calculate the linewidth as a function of temperature (see chapter 2). If the modulation indices for all three transitions are set to the same value at the reference temperature, their influences on the inferred CO/CO_2 ratio through the variation of linewidth are negligible. Thus, the measured ratio of column densities is

$$\frac{[CO]_{meas}}{[CO_2]_{meas}} = \frac{[CO]}{[CO_2]}\left[\frac{[S_k(T)/S_k(T_{ref})][\Delta\nu_k(T_{ref})/\Delta\nu_k(T)]}{a[S_i(T)/S_i(T_{ref})][\Delta\nu_i(T_{ref})/\Delta\nu_i(T)]+b[S_j(T)/S_j(T_{ref})][\Delta\nu_j(T_{ref})/\Delta\nu_j(T)]}\right]. \quad (5.5)$$

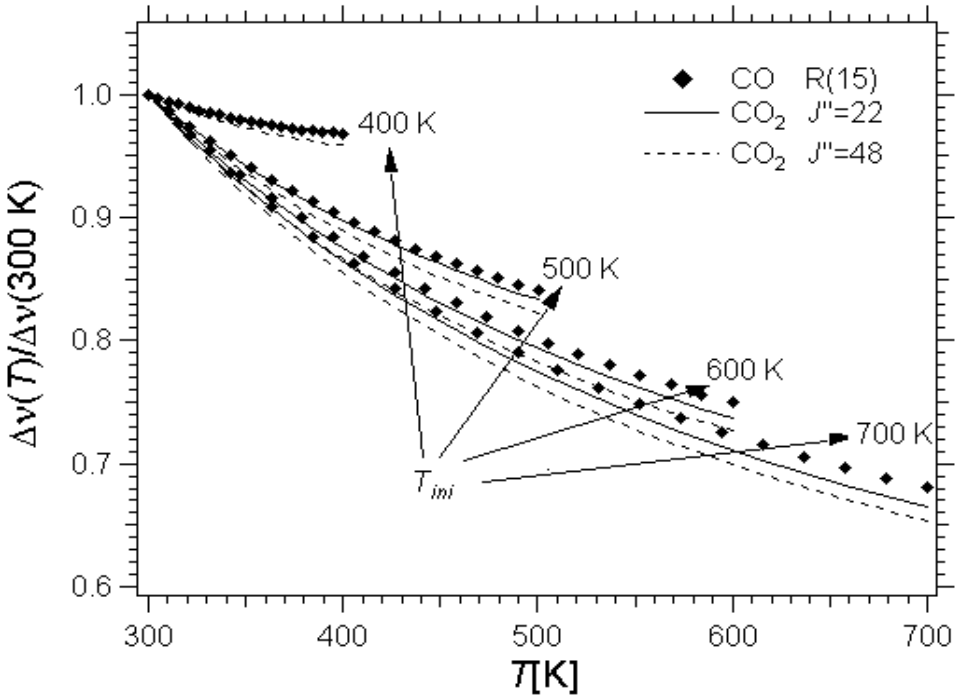

Figure 5.5 Calculated normalized collisional linewidths of the CO R(15) transition and CO_2 transitions (J''=22, 48) with different initial exhaust-gas temperatures (T_{ini}).

Since the exhaust-plume temperature and composition are changed mainly through turbulent mixing, mass and energy conservations are employed to correlate the variations of composition and temperature during the dispersion of a differential plume parcel:

$$C_{plume} M_{plume} d T_{plume} + C_{air} (T_{plume} - T_{air}) d M_{plume} = 0 , \qquad (5.6)$$

where T_{plume} is the temperature of exhaust parcel; T_{air} (300 K is assumed in the calculation) is the temperature of ambient air; M_{plume} is the mass of the exhaust parcel; C_{plume} and C_{air} are the specific heat capacities of the exhaust parcel and air, respectively; and dT_{plume} and dM_{plume} are the differential temperature and mass variations of the exhaust plume parcel, respectively. Using typical values for the composition of air (1.3% H_2O, corresponding to 50% humidity at 295 K) and of the initial exhaust (13% H_2O, 13% CO_2, and 74% N_2), the evolution of the plume-parcel composition during mixing is calculated as a function of temperature (from the initial exhaust temperature to 300 K). The evolution of collisional linewidths during dispersion is then calculated with known broadening coefficients and their temperature dependences for CO (see chapter 2) and CO_2 (Rosenmann *et al.* 1988). Figure 5.5 presents calculated normalized collisional linewidths for the R(15) transition of CO and two transitions of CO_2 (J''=22,48; other transitions have similar characteristics) with different initial exhaust temperatures. These normalized collisional linewidths have almost the same temperature and composition dependence, and thus

advantageously reduce the influence of the linewidth on measurements of the CO/CO_2 ratio and allow utilization of the WMS technique. Even with the linewidth dependence, the temperature factor, $F(T)$, for the line pair of (J″=22, J″=48) is consistently within ±3% of desired unity for different initial exhaust temperatures, as shown in figure 5.4.

5.5. Absorption thermometry for screening cold-start vehicles

Simultaneous measurements of operational parameters such as speed, acceleration and exhaust-gas temperature could minimize false identification of gross polluters (Walsh *et al.* 1996). Speed and acceleration measurements have previously been incorporated into remote sensing (MD-Lasertech Ltd; Sjodin and Lenner 1995; Sjodin *et al.* 1997). Because of the difficulty of measuring exhaust-gas temperature remotely, the current strategy implemented to avoid labeling cold-start vehicles as gross polluters is to avoid or reduce the number of cold-start vehicles in the fleet to be measured by choosing "good" sites. This is a serious limitation on current RSD.

The temperature effect on column-density measurements discussed in section 5.4 is not always deleterious and may be exploited to measure the initial exhaust-gas temperature. With a known design of the vehicle exhaust system, the measured temperature can be converted to the catalytic-converter temperature for screening or identifying cold-start vehicles. A vehicle moves only 1.8 centimeters per millisecond even at a speed of 40 miles per hour, and the mixing of exhaust with air is small over short distance scale. Therefore, the initial exhaust-gas temperature can be obtained if the gas temperature can be measured within several milliseconds. Such time response has been previously demonstrated for diode-laser-based two-line H_2O-absorption temperature measurements in combustion environments (at a 10-kHz measurement rate with scanned-wavelength (Furlong *et al.* 1999) and at a 2-MHz measurement rate with fixed-wavelength (Sanders *et al.* 2000a) schemes). However, H_2O-absorption thermometry is not appropriate in this circumstance because of the large background concentration of H_2O in ambient air. Therefore, two-line CO_2-absorption thermometry of the initial exhaust temperature is proposed to exploit the temperature dependence of the column densities derived from the two CO_2 measurements,

$$\frac{[CO_2]_j}{[CO_2]_i} = \frac{S_j(T)/S_j(T_{ref})}{S_i(T)/S_i(T_{ref})}. \tag{5.7}$$

Figure 5.6 shows the ratio of the line pairs from figure 5.4. These ratios are very strong functions of temperature and thus good temperature sensitivity can be obtained. The effect of linewidth on the ratio is less than 5% and negligible for this purpose.

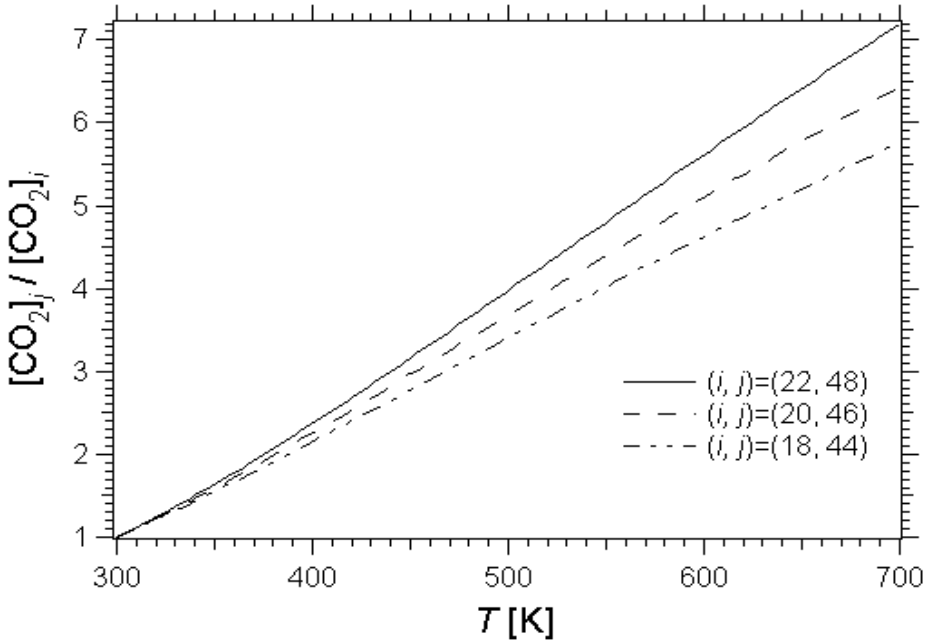

Figure 5.6 Ratio of measured CO_2 column densities (see equation (5.7)) with different transition pairs as a function of temperature, T_{ref}=300 K

In summary, we can determine the initial exhaust-gas temperature to screen cold-start vehicles as well as the CO/CO_2 ratio from a combination of a two-line CO_2 sensor and a one-line CO sensor. Our laboratory has previously demonstrated such wavelength-multiplexed sensors combining several laser beams at different wavelengths together along the same path to measure multiple gas concentrations and temperature simultaneously (Webber *et al.* 2000; Furlong *et al.* 1999; Sanders *et al.* 2000a).

5.6 Laboratory demonstration measurements

On-road remote sensors of vehicle exhaust require a much faster measurement repetition rate than that required for stationary source monitors, since vehicles may move at high speed and exhaust plume evolves quickly. A laboratory demonstration measurement was made with the same setup as shown in figure 4.9, except at a measurement repletion rate of 100 Hz. This repetition rate was limited by the relatively slow modulation frequency (33 kHz). Figure 5.7 presents the measured CO effluent from a fluctuating flame with an equivalence ratio of 0.53. One representative lineshape was shown in the inset. The variation in CO effluent with time follows the flame instabilities for this very lean

condition. The detection sensitivity of CO is estimated to be ~1 ppm-m. Although the scanned-mean-frequency technique was used in the demonstration measurement to check signal quality such as etalon noise, a fixed-mean-frequency scheme can increase the measurement repetition rate to the chosen detection bandwidth (~1.5 kHz in this case) without sacrificing the signal-to-noise ratio. Therefore, the fixed-mean-frequency scheme is preferred for in-field measurements. If a fraction of the laser beam is directed to a reference cell filled with CO, the laser mean frequency can be locked to the linecenter using the third harmonic component of the transmitted signal as a feedback signal to the temperature or current controllers of the diode laser. This reference-cell measurement can also provide secondary calibration and system self-checking of the system.

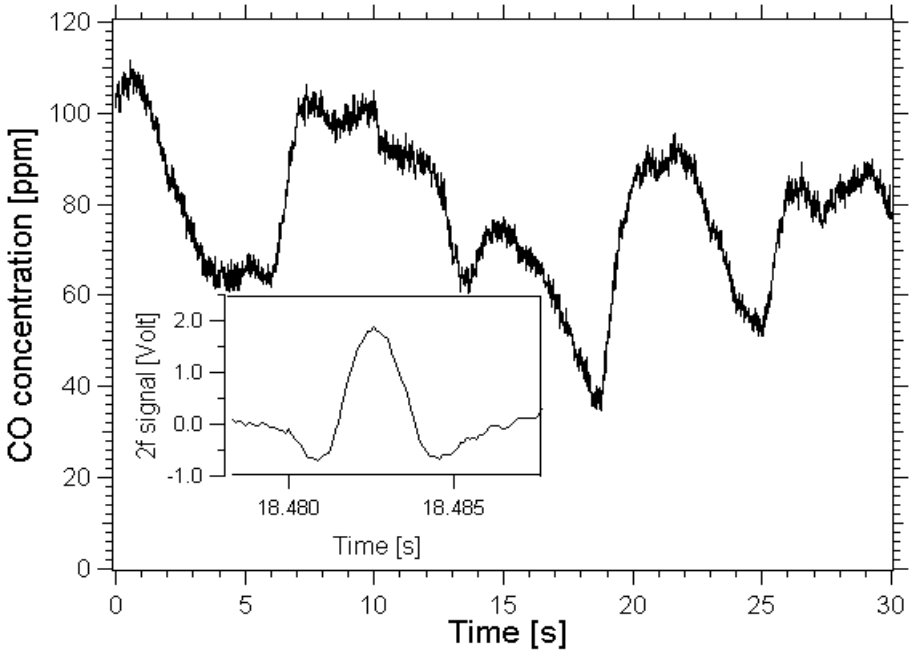

Figure 5.7 Measured CO effluent (1.5-kHz detection bandwidth, 100-Hz measurement repetition rate) in the exhaust duct (470 K) at an equivalence ratio of 0.53. The inset shows one representative measured lineshape.

Unfortunately, the laser stopped lasing when I was preparing for real measurements of vehicle exhausts. It would have been more valuable and convincing if new laser sources with good reliability could be obtained to demonstrate the real measurements.

5.7 Discussion

The sensitivity of ~1 ppm m with 1.5-KHz detection bandwidth demonstrated in the laboratory corresponds to a sensitivity of 20-ppm CO in the exhaust if the laser beam is optimally aligned to tailpipes with an assumed diameter of ~5 cm. In the demonstration measurements, the modulation frequency is 33 kHz, which is limited by the bandwidth of the detector and lock-in amplifier. If the modulation frequency is increased to ~10 MHz with commercially available large-bandwidth components, the sensitivity can be improved by about one order of magnitude (Silver 1992) to 2-ppm CO. Table 5.1 lists the California CO emission standards (g/mile) for 2001 and subsequent models of passenger cars. The most stringent CO-emission standard (except for zero-emission vehicles) is 1 g/mile for SULEV, which corresponds to ~500 ppm CO, assuming a fuel economy of 30 mile/gallon. Therefore, a 2.3-μm absorption sensor, which has a detection limit 2-3 orders of magnitude better than that of the current RSD, is expected to be able to characterize even the cleanest combustion-powered vehicles.

Table 5.1. California CO emission standards (g/mile) for 2001 and subsequent model passenger cars (California Environmental Protection Agency Air Resources Board 1999).

Emission standards		Time period	Durability Vehicle Basis (miles)			
			50,000	100,000	120,000	150,000 (optional)
LEV I	TLEV	2001-2003	3.4	4.2		
	LEV	2001-2006	3.4	4.2		
	ULEV	2001-2006	1.7	2.1		
LEV II	LEV	2004-	3.4		4.2	4.2
	ULEV	2004-	1.7		2.1	2.1
	SULEV	2004-			1.0	1.0

TLEV: transitional low-emission vehicle; LEV: low-emission vehicles; ULEV: ultra-low-emission vehicles; SULEV: super-ultra-low-emission vehicles.

The measurements of initial exhaust-gas temperature may impose strict requirements on the alignment of the laser beam across tailpipes. One possible configuration is a main sensor unit with several probes located some distance apart along a roadway. These probes can be installed at different heights so that at least one laser beam is aligned reasonably well with the tailpipe in order to obtain the initial exhaust temperature. In addition, this distributed sensor makes repeated concentration measurements, which are essential in order to accurately identify high emitters (Sjodin *et al.* 1997) and to identify highly variable emitters prevalent among the newer

technology vehicles with defective emissions control systems (Bishop and Stedman 1996). The main sensor unit contains diode lasers, signal-processing electronics and a data-reduction computer. Fiber optics can be used to transport multiplexed monitoring laser beams to and from all probes, as has been demonstrated elsewhere (Schiff *et al.* 1996). With this configuration, the multiple concentrations and the highest gas temperature acquired by all these probes can give an accurate evaluation of vehicles' emission status.

Table 5.2 Summary of the differences between the new and the traditional sensing strategies

	New Strategy	Traditional Strategy
Temperature	Unknown and non-uniform	Known or uniform
Concentration	Varying, non-uniform	Fixed, uniform
Maintenance	Easy, cheap	Difficult, expensive
Time response	Quick	Slow

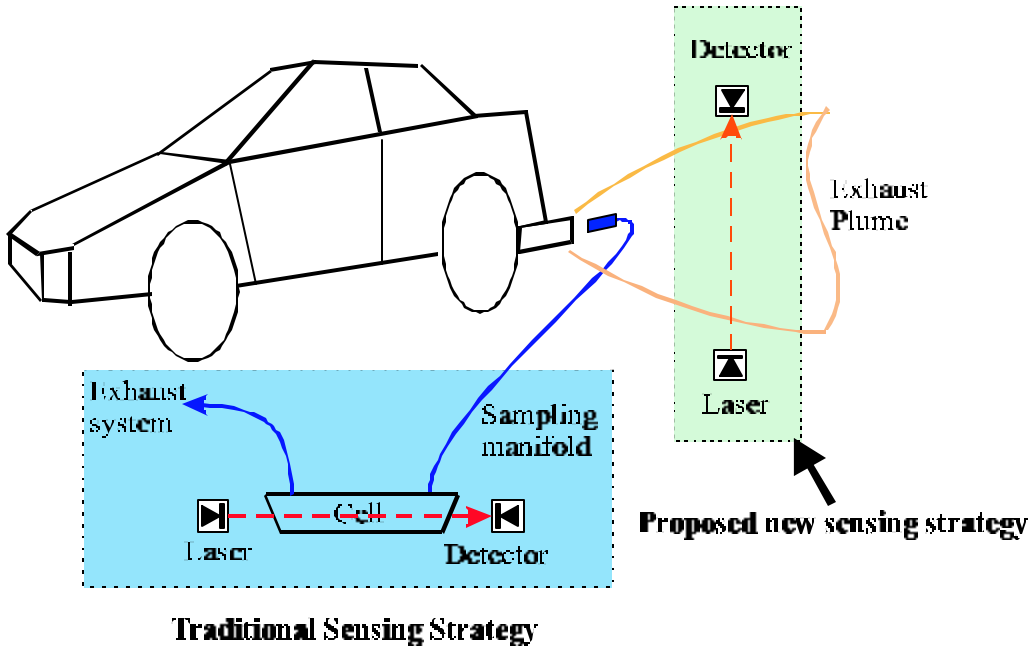

Figure 5.8 Schematic illustrating the traditional and the proposed new sensing strategies.

Sensors using the temperature- and composition-insensitive strategy developed in this chapter may also be applied to the remote sensing of aircraft exhausts in airports, since the effects of temperature can be large and standard RSDs may give erroneous measurements. However, the

application domain of this proposed sensing strategy is not limited to monitoring mobile vehicles. It can also be applied to monitoring many stationary sources. Traditionally, absorption sensors require either uniform temperature or known temperature profile along the beam path to calculate the transition linestrength. They also require uniform concentration profile along the beam path. More often than not, these uniformity requirements cannot be satisfied, and thus sampling gas into a gas cell with an extractive probe is often necessary to obtain these uniformities. However, this inevitably increases the system complexity and maintenance difficulty, and reduces time response. The new strategy proposed in this chapter eliminates these constraints, and can thus be applied to develop *in situ* sensing systems with fast time response, easy usage and little maintenance. Table 5.2 summarizes these differences between the traditional and the proposed strategies. Smog check is one potential application field where the proposed new strategy may reduce the checking time from tens of minutes to several seconds (figure 5.8). In fast-paced modern life, the advantage of significant time saving is especially attractive.

Chapter 6. *High-pressure Oxygen Sensing with VCSELs*

Though VCSELs have been applied to gas sensing and specifically oxygen sensing (Weldon *et al.* 1997; Zappe *et al.* 2000) previously, the goal of that work was limited to simply replacing edge-emitting lasers with cheaper laser sources. In this chapter, the characteristics and their mechanisms of some 760-nm VCSELs are investigated and compared to conventional edge-emitting lasers. Then discussion is focused on the fast and large wavelength tunability of these VCSELs to explore a new application domain impossible with conventional edge-emitting lasers: scanning-wavelength scheme for high-pressure oxygen measurements.

6.1 Motivation

Many industrial combustion processes such as electrical power generation and aeropropulsion systems operate at pressures well above atmospheric pressure. Sensors monitoring oxygen concentrations for these processes play important roles as diagnostic tools in fundamental research and as part of active control systems. Zirconia sensors (Wort 1977) have been traditionally used to measure oxygen concentrations in these hostile environments. However, the potentially fast time response, the path-averaged measurements, and the non-intrusive nature of semiconductor-laser diagnostics can offer some advantages in many applications.

Oxygen measurements using A-band transitions near 760 nm have been demonstrated with a variety of semiconductor diode lasers: Fabry-Perot (FP) (Kroll *et al.* 1987; Philippe and Hanson 1993), short external cavity (Bruce and Cassidy 1990), widely-tunable external cavity (ECDL) (Nguyen *et al.* 1994), distributed feedback (DFB) (Martinelli *et al.* 1996; Weldon *et al.* 1997), and vertical cavity surface-emitting lasers (VCSELs) (Weldon *et al.* 1997; Zappe *et al.* 2000; Silver and Kane 1999). To the best of our knowledge, no semiconductor-laser-based techniques have been used to measure oxygen in high-pressure ($\geq$ 5 bar) environments prior to this work despite the significance of such measurements for many industrial processes.

Both scanned- and fixed-wavelength absorption techniques have been used in semiconductor-laser gas property sensors (Baer *et al.* 1996). In the fixed-wavelength scheme the laser wavelength is typically fixed at an absorption linecenter. The fixed-wavelength scheme suffers from two complications: non-resonant attenuation and the need for accurate lineshape information. Many industrial combustors contain solid- and liquid-phase aerosols such as soot and fuel droplets, which attenuate the light by scattering and absorption. In addition, the

transmission of optical windows may be variable due to fouling or thermal and mechanical stresses. Furthermore, the refractive-index gradient existing in combustion environments may cause beam steering. Multiple non-resonant (i.e., away from the probed gas-transition frequency) lasers are normally required to track these non-resonant attenuations and permit meaningful fixed-wavelength measurements of the resonant gas absorption (Sanders *et al*. 2000b). Some assumptions on the spectral dispersion of aerosol extinction and window transmission are also necessary to account for the wavelength offset between resonant and non-resonant lasers. The second complication, namely that gas absorption is dependent on transition lineshape, recognizes that the lineshape function varies with pressure, temperature and gas composition. Accurate knowledge of these parameters and their effects on transition lineshape is therefore necessary.

The scanned-wavelength scheme can remove both of these complications by rapidly tuning the laser wavelength over a sufficiently large range. A correct baseline representing zero gas absorption can be inferred from the spectral variation of the resonant gas absorption in this scanned wavelength range. Non-resonant lasers and assumptions on the spectral dispersion of non-resonant attenuations are no longer required. In addition, accurate lineshape data is obtained directly from the measurements. Thus, the scanned-wavelength scheme offers significant advantages over the fixed-wavelength scheme, especially in hostile and/or multi-phase environments.

Due to the limited current-tuning frequency range (typically <2 cm^{-1}) of conventional edge-emitting diode lasers (DBR, DFB or FP), the scanned-wavelength strategy with such devices is limited to atmospheric pressure at room temperature or a few atmospheres at elevated temperatures. Although widely-tunable ECDLs have been used for gas sensing studies and offer many advantages owing to their large wavelength tuning ranges, they are generally limited to laboratory research tools because of high laser cost and stringent maintenance requirements. In addition, the tuning rate is inherently slow since ECDLs realize large-range wavelength tuning using mechanical components. Many companies and research institutes are actively developing a new generation of ECDLs using either edge-emitting lasers or VCSELs as gain media. Although the devices of some companies, e.g., New Focus and Iolon, still rely on mechanically tuning a grating, new designs emphasizing miniaturization and robustness are pursued. Some devices, e.g., Blue Sky Research's Programmable ITU Lasers, use fast miniature electro-optical components to realize extremely fast tuning (microseconds to scan over ~100-nm range). For some other devices, e.g., Bandwidth9's tunable VCSELs, the entire miniature external-cavity lasers including

gain media and the tuning element (figure 6.1) are monolithicly integrated. These new-generation ECDLs will be cheaper, more reliable, of much smaller size (some devices can even be put into a standard Butterfly package), and have much faster tuning speed. These new ECDLs will change our previous perception of ECDLs and enable a new horizon of applications impossible before. Some of these new-generation ECDLs are currently shipped as samples and expected to be commercially available next year.

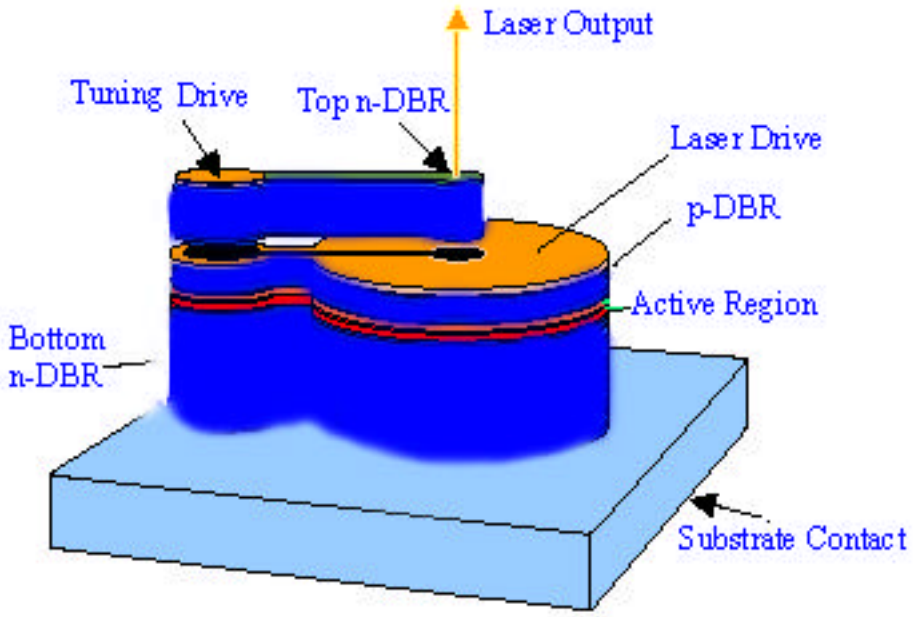

Figure 6.1 Tunable VCSEL developed by Bandwidth9 (www.bw9.com). Tuning is achieved by moving the cantilever up or down to change the laser cavity length.

As discussed in chapter 3, due to their unique topology, VCSELs have some distinct advantages over the conventional edge-emitting lasers, such as low current threshold operation, high two-dimensional packing density, wafer-scale testing capability, single-longitudinal-mode operation, a circular output beam and small divergence angle highly desirable for fiber coupling. In particular, the significantly lower manufacturing cost than that of DFBs may allow wide deployment of VCSEL-based sensors monitoring various industrial processes.

Some VCSELs also provide a large current-tuning frequency range (>30 cm^{-1}), which results from their small cavity volume and the strong resistive heating due to their large series resistance associated with the distributed Bragg Reflector (DBR) mirrors (see equation (3.36)). This large current-tuning range of optical frequency was considered as a negative factor for gas detection at

low pressures because of the corresponding large laser phase noise compared to the small transition linewidth at low pressures (Weldon *et al.* 1997). However, this same laser characteristic is exploited here in a positive way to enable a new class of scanned-wavelength absorption sensors for high-pressure combustion environments where gas transitions have very large linewidth and thus the effect of laser phase noise is negligible.

The characteristics of some VCSELs suitable for gas property sensing at high pressures will be presented first. Then this thesis exploits the large and fast current tunability of these VCSELs to demonstrate the first application of VCSELs in high-pressure gas detection using both direct-absorption and wavelength-modulation spectroscopy (WMS) techniques.

6.2 Laser characteristics

6.2.1 *L-I* and *V-I*

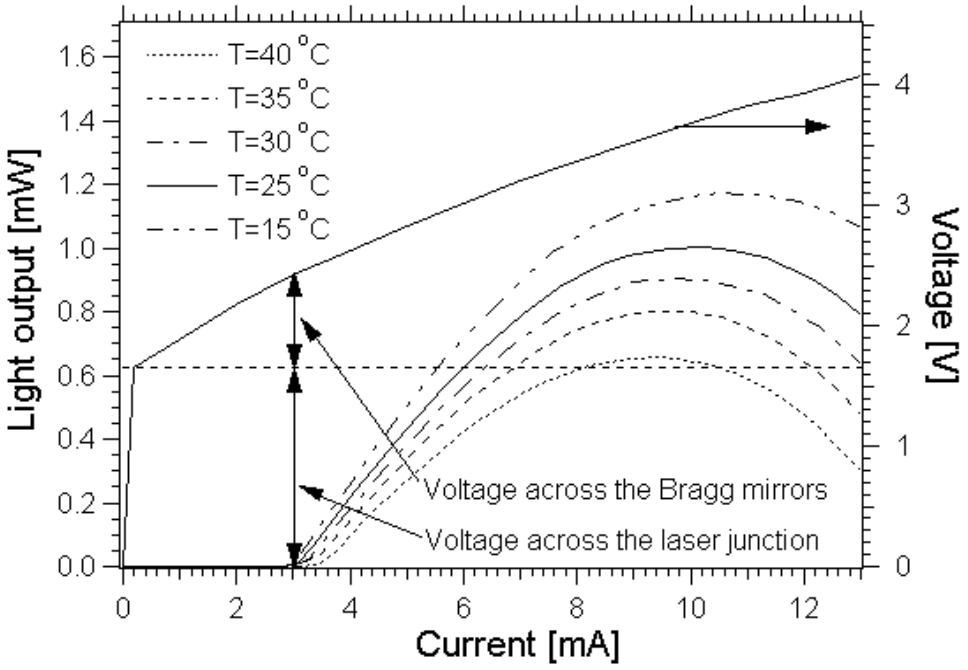

Figure 6.2 Light output versus current (*L-I*) characteristics at different heat-sink temperatures and operation voltage versus current (*V-I*) characteristics at a heat-sink temperature of 25 °C for a 760-nm VCSEL.

The output power versus injection current (*L-I*) characteristics of a quantum-well AlGaAs/GaAs VCSEL (CSEM760, Centre Suisse d'Electronique et de Microtechnique, Switzerland) were

measured at different heat-sink temperatures (figure 6.2). Also shown is the operation voltage versus current (*V-I*) at a heat-sink temperature of 25 °C. The laser has two distinct voltage drops: the voltage across the laser diode junction and the voltage across the series resistors associated with the two DBR mirrors. The voltage across the diode junction is approximately $h\nu/e$ (~1.63 V for 760-nm lasers), where $h\nu$ is the laser emission photon energy and e the electronic charge. Therefore, the effective series resistance of the two Bragg mirrors near threshold is: $R_{th} = (V_{th} - h\nu/e)/I_{th} \cong 260$ ohms, much larger than the a few ohms typical of edge-emitting lasers. This large resistance originates from the steep energy barriers at the heterojunctions of DBRs. This resistance is especially large for P-type DBRs, since it is very difficult for holes to climb up these barriers due to the holes' large effective mass. Combined with the small cavity volume of VCSELs, this large series resistance generates very large heat density and thus may lead to very high temperatures of the laser cavity.

Both the gain profile and the Fabry-Perot mode position red shift with increasing temperature. However, since the temperature coefficient of the band-gap energy is much larger than that of the effective refractive index, the gain-profile peak shifts with temperature much faster than the Fabry-Perot mode position, and thus the Fabry-Perot mode position deviates from the gain-profile peak at large injection current. In addition, the gain profile broadens and the peak gain reduces significantly at high temperatures. When this loss of gain with increasing temperature is larger than the increase of gain with increasing current, the output power starts to roll over (Hasnain *et al.* 1991) as shown in figure 6.2.

6.2.2 Wavelength tuning

Like edge-emitting lasers, the wavelength of a VCSEL can be tuned by varying either injection current or heat-sink temperature. However, due to the large resistive heating and small cavity volume of the VCSEL described above, the wavelength-tuning range and frequency response are significantly larger and faster than those of edge-emitting lasers.

Figure 6.3 shows the quasi-static current- and temperature-tuning characteristics of a VCSEL measured with a wavemeter. The temperature tuning rate is ~-0.93 cm^{-1}/K (0.055 nm/K). The current tuning rate varies from –4.5 cm^{-1}/mA (0.26 nm/mA) near threshold to -9.6 cm^{-1}/mA (0.56 nm/mA) at a current of 13 mA. A quadratic relationship (Hasnain *et al.* 1991) can be used to describe the current dependence of optical at 25 °C: $\nu \cong 13164 - 2.61I - 0.253I^2$, where ν is the optical frequency in cm^{-1} and I is the current in mA. The laser-cavity temperature should be the

same as the heat-sink temperature at zero injection current, and thus the Fabry-Perot mode frequency at 25 °C was estimated to be 13164 cm^{-1} from the above quadratic relationship. The smallest laser frequency measured was 13072.5 cm^{-1} at 13-mA current and 40 °C heat-sink temperature. As discussed in section 3.5, the static or quasi-static current-tuning rate is solely due to the thermal effect. Therefore, the cavity temperature corresponding to this frequency can be estimated from the measured temperature-tuning rate of -0.93 cm^{-1}/K: T=25+(13164-13072.5)/0.93=123 °C, demonstrating that very high laser-cavity temperature can be reached in VCSELs by resistive heating.

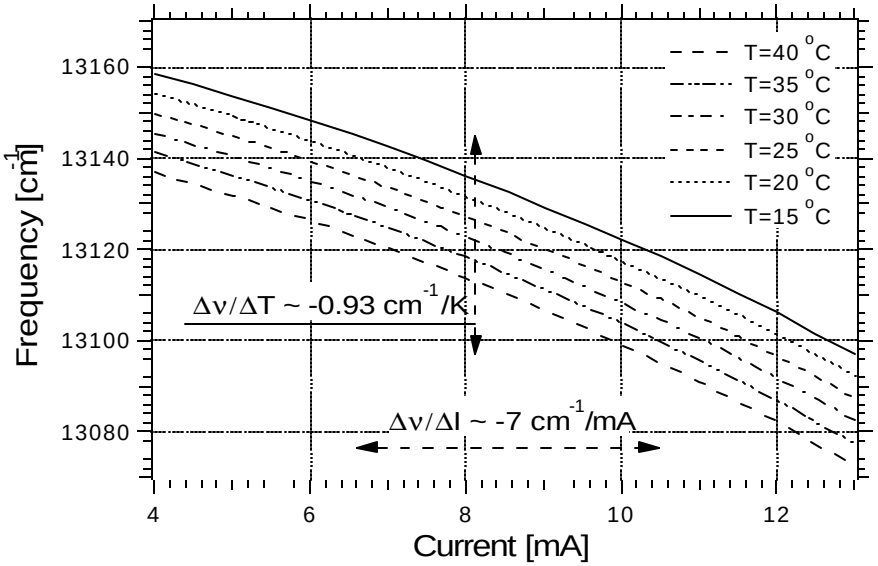

Figure 6.3 Quasi-static optical-frequency tuning by varying injection current and heat-sink temperature.

Figure 6.4 shows the current-tuning range of optical frequency as a function of tuning frequency, characterized with a 3-mm-thick sapphire etalon having a free spectral range (FSR) of 0.95 cm^{-1}. For these measurements the laser operated at a bias current of 8 mA and with a 6-mA peak-to-peak-amplitude ramp modulation. In the frequency range considered, the wavelength blue shift through the increase of free carrier number density is negligible compared to the temperature-rise-induced wavelength red shift. The frequency response of the current tuning thus characterizes the VCSEL's thermal response (equation (3.36)) and gives a thermal time constant of several microseconds, much faster than the typical several hundred microseconds characteristic of edge-emitting lasers. This small thermal time constant is due to the small cavity volume of the VCSEL. The inset of figure 6.4 presents a specific etalon trace corresponding to a 10-kHz ramp

modulation; an optical-frequency tuning range larger than 30 cm^{-1} was achieved. From the time required to cool the laser after the sharp decrease of current, the thermal time constant of this VCSEL was also estimated to be several microseconds.

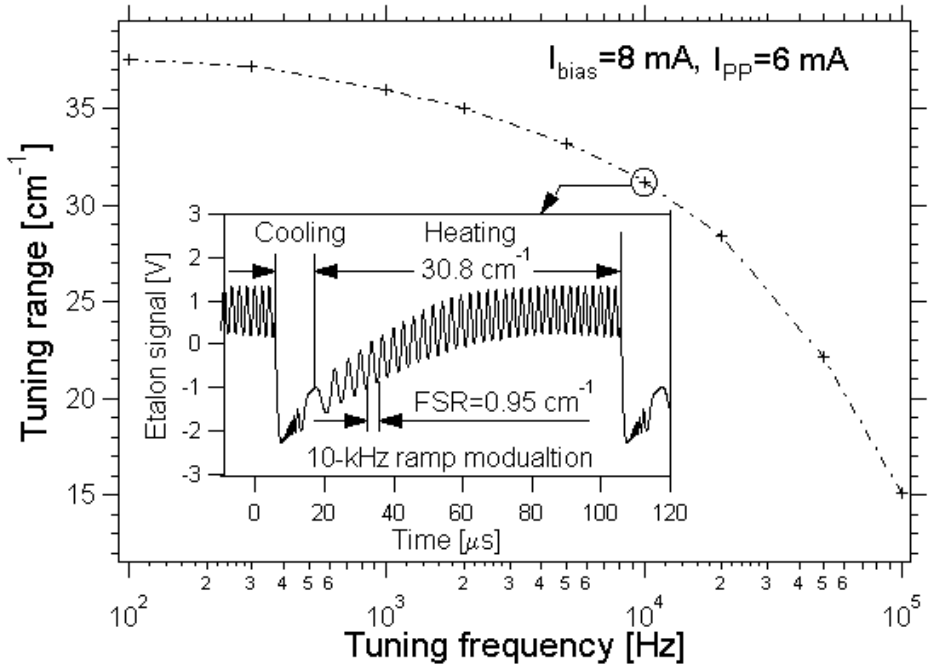

Figure 6.4 The optical-frequency tuning range as a function of ramp-current modulation frequency characterized by an etalon. The inset shows one specific etalon trace obtained at a modulation frequency of 10 kHz.

6.2.3 Transverse mode

Unlike edge-emitting lasers, the effective cavity length of VCSELs is typically one wavelength or several wavelengths for the extended-cavity case, and hence the longitudinal mode spacing is so large that single longitudinal mode operation is ensured. However, due to the relatively large lateral dimension of VCSELs, higher-order transverse modes may appear. The VCSELs used here, with a 5-μm-diameter optical aperture, effectively suppress higher-order transverse modes when the injection current is smaller than 7.5 mA. At higher current, a higher-order transverse mode was observed at a wavelength of ~0.35-nm to the blue of the fundamental mode. Figure 6.5 presents the ratio of the power of this higher-order mode to the total power characterized using a monochromator. At a heat-sink temperature of 15 ^{o}C, the higher-order transverse mode may contain more than 25% of the total output power at high current levels. It is believed that self-focusing induced by the spatial hole burning of carrier and thermal lensing cause the spatial width

of the fundamental mode to decrease. This shrinkage of fundamental mode size limits the fundamental mode power and leads to the appearance of higher-order modes (Wilson et al. 1994; Zhao and McInerney 1996).

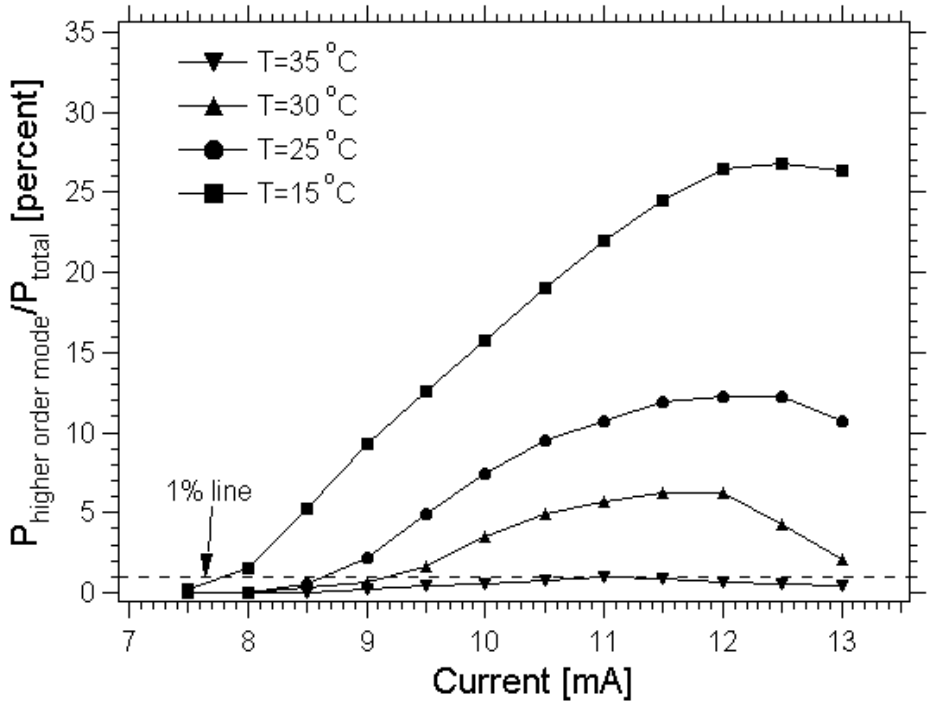

Figure 6.5 Higher-order transverse modes appear at high pumping levels (>7.5 mA) and can be suppressed by increasing heat-sink temperature.

As shown in figure 6.5, increasing the heat-sink temperature suppresses the higher-order modes. With the heat-sink temperature higher than 35 °C, the VCSEL tested always has better than 20-dB side-mode suppression. Thus, at high heat-sink temperatures, the laser can be tuned over a larger current range while maintaining single-mode operation. This side-mode suppression may be explained by the lower gain at higher temperatures described above. In addition, higher temperature may increase the carrier diffusion coefficient and thus reduce the spatial hole burning effect. However, this suppression of higher-order modes comes at the cost of sacrificing the output power. Significant achievements have been made recently in the high-power single-mode operation of VCSELs, and this remains an active research field. Currently, ~5 mW represents the best laboratory-demonstrated single-mode output power (Choquette 2000).

6.2.4 Intensity noise

The commonly used figure of merit for laser excess noise is the relative intensity noise (RIN), defined as the ratio of the square of laser power fluctuation per unit bandwidth to the square of laser power (Appendix A). Although there have been many studies on the RIN of VCSELs, they are focused on high frequency regions, driven by high-speed applications such as telecommunication and optical interconnection. RIN characteristics in the low frequency region relevant to high-pressure spectroscopic measurements are presented here.

Figure 6.6 shows the RIN versus output power with different heat-sink temperatures at 50 kHz. The injection current was varied from 4 mA to 13 mA for each temperature, and the laser intensity noise was characterized using a lock-in amplifier (SR830, Stanford Research Systems). The RIN of the tested AlGaAs VCSEL is comparable to that reported for DFB AlGaAs lasers (Martinelli *et al*. 1996) and is approximately inversely proportional to the laser power cubed. Thus, large output power is desired to achieve low laser intensity noise. The RIN of the VCSEL was the lowest at a heat-sink temperature of 15 ^{o}C and a current of 11 mA despite the fact that large higher-order mode power was observed at this operating condition (figure 6.5). However, the excess noise of each lasing mode may be significantly higher than the noise of total power (Law and Agrawal 1997) because of the strong anti-correlation between the two modes, i.e., intensity fluctuations of one mode are cancelled by fluctuations of the other mode resulting in low noise when detecting the total laser power. For the absorption-spectroscopy sensors considered here using spectral features narrower than the mode frequency spacing, it is the excess noise of each mode that determines the sensor performance. Therefore, this multimode operation regime should be avoided. The inset of figure 6.6 presents the RIN as a function of frequency (f) recorded with single-mode operation at a bias current of 10 mA and a heat-sink temperature of 40 ^{o}C. The RIN decreases roughly as $1/f$.

The polarization orientation of VCSELs is not as stable as that of edge-emitting lasers due to the circular symmetry of VCSELs. This polarization fluctuation is likely to increase the apparent laser intensity noise (Mukaihara *et al*. 1995) and thus may reduce the sensor performance for sensor designs using polarization-sensitive components, such as the isolators frequently used in laser absorption sensors to prevent optical feedback into laser cavities. Some asymmetries of geometry, strain, or crystalline orientation have been introduced into recent VCSEL designs so that stable polarization orientation has been consistently achieved.

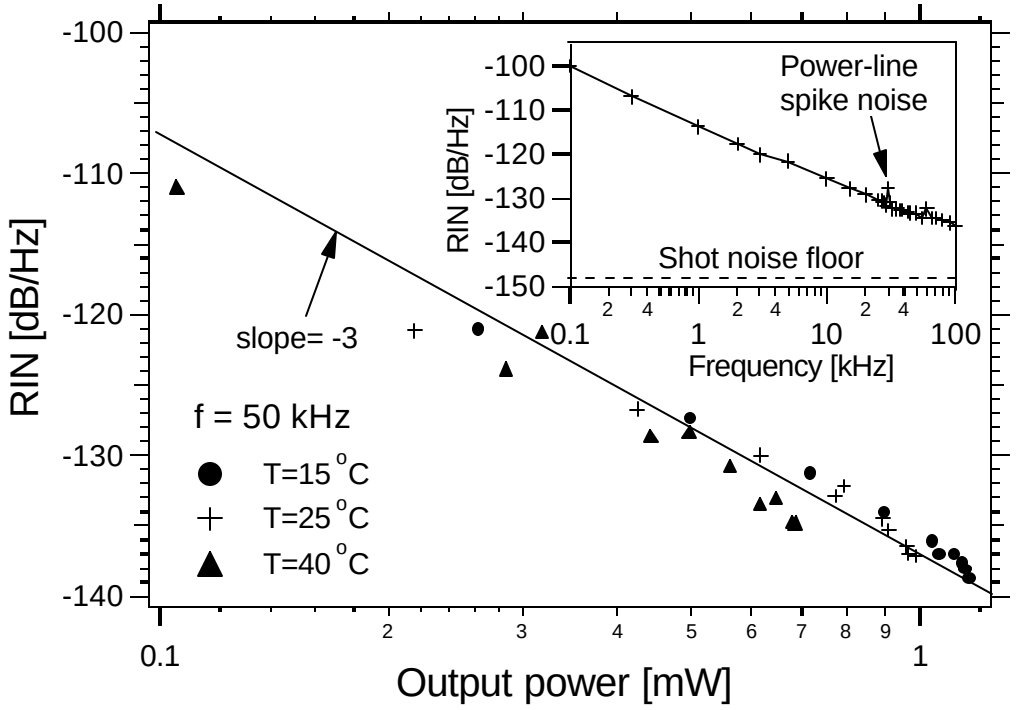

Figure 6.6 Measured laser relative intensity noise (RIN) as a function of output power. The inset shows RIN versus frequency characteristic recorded at a bias current of 10 mA and a heat-sink temperature of 40 °C.

6.3 Demonstration measurements in a gas cell

Figure 6.7 illustrates the experimental setup for high-pressure oxygen measurements. An antireflection-coated lens was used to collimate the laser beam from a VCSEL. This collimated laser beam was directed through a 55-cm wedged-window cell containing dry air and was then detected by a silicon detector with an integrated amplifier. The laser beam outside the gas cell was enclosed in nitrogen-purged boxes to eliminate atmospheric-oxygen absorption. A battery-powered low-noise current source drove the VCSEL. A ramp modulation of 50 Hz or 500 Hz was used to scan the laser frequency over oxygen features for WMS or direct-absorption measurements, respectively. For WMS measurements, a 50-kHz sinusoidal modulation of peak amplitude ~0.31 cm^{-1} was superimposed on the 50-Hz ramp modulation. A lock-in amplifier with a time constant of 100 μs was used to detect the second harmonic ($2f$) signal. For direct-absorption measurements, a 0.1-μF capacitor was connected across the diode laser to further reduce the current noise. Assuming the VCSEL has a 200-ohm dynamic resistance, the bandwidth was thus limited to approximately 10 kHz. The laser heat-sink temperature was not actively controlled in the experiment. The requirement for the case-temperature stability of VCSELs is much less stringent than that of edge-emitting lasers, because the wavelength drift induced by

temperature drift is very small compared to VCSELs' current-tuning wavelength range. Thus temperature controllers typically used in diode laser sensors may be spared to further reduce the cost of VCSEL-based sensors.

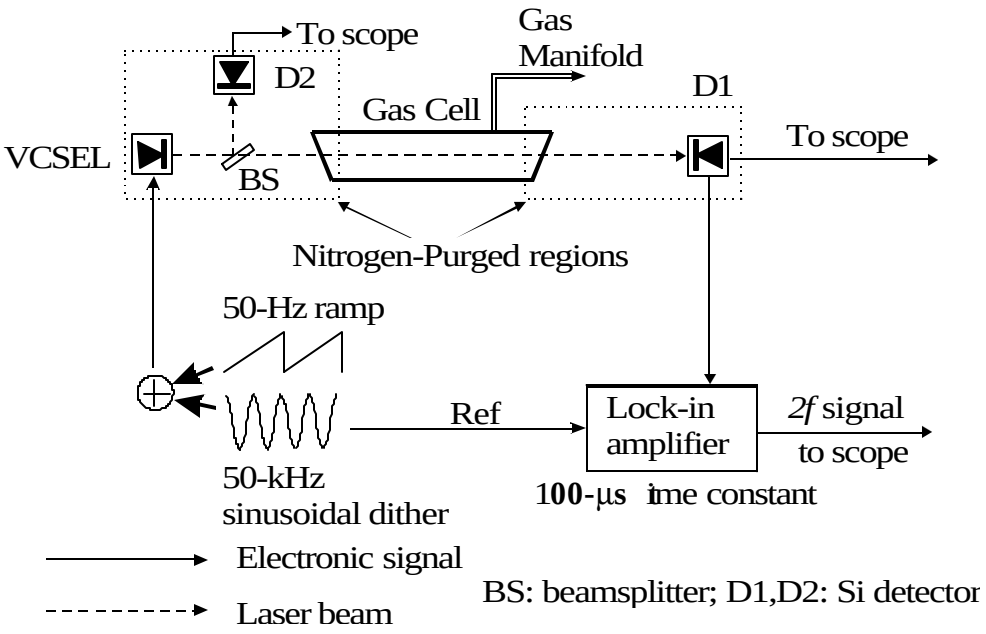

Figure 6.7 The experimental setup for high-pressure oxygen measurements. The reference beam was only used for direct-absorption measurements.

6.3.1 Direct-absorption measurements

Diode-laser absorption sensing is based on absorption of laser radiation as the beam propagates from the source to a detector. The fractional transmission, $T(\nu)$, of a monochromatic laser source through a gas medium of length L (cm) has been discussed in chapter 2. Although only gas-cell measurements were made in this experiment, aerosol extinction and beam steering are included here because our final goal is to apply this sensor to hostile combustion environments. Therefore, the expression of this fractional transmission is extended here to include these effects:

$$T(\nu) = \left(\frac{I(\nu)}{I_0(\nu)} \right) = \exp[-k_g(\nu)L] \exp[-k_a(\nu)L] T_w(\nu) B(\nu), \qquad (6.1)$$

where I and I_o are the transmitted and incident laser intensities, and the four terms in the right hand side represent gas absorption, aerosol extinction, optical-window transmission, and beam steering effect, respectively. k_a [cm^{-1}] is the extinction coefficient of aerosol in the probed medium. The product k_gL is the spectral absorbance of gas absorption. Taking the natural logarithm of Eq. (6.1), we obtain

$$\ln\left(\frac{I_0(\nu)}{I(\nu)}\right) = XPL\sum_{i=1}^{N} S_i(T)\Phi_i(\nu) + k_a(\nu)L - \ln T_w(\nu) - \ln B(\nu) \qquad (6.2)$$

Because of the spectral dispersion of the optical constants of aerosol, optical window and probed gas media, aerosol extinction, window transmission and beam steering are fundamentally weak functions of optical frequency. With the scanned-wavelength scheme, this spectral dispersion effect is negligible in the scanned spectral range of several tens of wavenumbers. However, these non-resonant attenuations are also functions of time, due to the time-dependent aerosol morphology and number density, fouling and stresses of optical windows, and refractive index gradient (Petersen *et al.* 1997). These time functions are finally manifest as functions of optical frequency as the laser frequency varies with time through injection current tuning. To reduce these time-varying effects, the laser frequency should be scanned much faster than the characteristic frequencies of these non-resonant attenuations so that they vary slowly with optical frequency during one scanning period. Thus all of the non-resonant attenuation can be practically represented by a first-order or at most second-order polynomial of optical frequency. This simplification is enabled by the rapid tunability of VCSELs. Eq. (6.2) then becomes

$$\ln\left(\frac{I_0(\nu)}{I(\nu)}\right) = XPL\sum_{i=1}^{N} S_i(T)\Phi_i(\nu) + P_2(\nu)\ , \qquad (6.3)$$

where the second-order polynomial $P_2(\nu)$ represents the sum of non-resonant attenuations dependent on specific physical settings.

The oxygen transition doublets are well separated (>8 cm^{-1}) in the tail of the *P* branch (these transitions have relatively strong absorption at elevated temperatures in combustion environments). Regions far from these doublets have negligible oxygen absorption for pressures up to ~10 bar at room temperature or 30-40 bar at combustion temperatures. The incident laser intensity $I_0(\nu)$ may be obtained by fitting a polynomial to the negligible-absorption regions of the transmitted laser signal (as shown in figure 2.2), and thus the need for a reference beam can be avoided in this approach. One advantage of this approach is that the polynomial term in Eq. (6.3) representing non-resonant attenuation is implicitly removed by this procedure to obtain the incident laser intensity $I_0(\nu)$. This relatively simple approach should be employed practically wherever possible, unless the common-mode noise rejection capability of the dual-beam scheme described below is desirable.

However, at even higher pressures or for other species (e.g., H_2O) with dense transitions, the collision broadening of transitions may be sufficiently large that negligible-gas-absorption spectral regions cannot be obtained within the scan range. Therefore, the simple approach described above cannot be used in these circumstances. Here, for the first time a strategy is developed to deal with this general case. Relatively dense transitions in the R branch were purposely chosen to measure oxygen. In this case, a beamsplitter was used to monitor the incident laser intensity (figure 6.7). It is not necessary to match the signal intensities of two arms. The splitting ratio is compensated by the polynomial term in Eq. (6.3) and thus the reference beam intensity is simply referred to as incident laser intensity $I_0(\nu)$. The measured value $ln[I_0(\nu)/I(\nu)]$ is called quasi-absorbance in this paper. Note that the quasi-absorbance is meaningful even if it is negative; the gas properties are obtained from the shape rather than the absolute magnitude of the measured quasi-absorbance (see details below). However, the shape of a signal trace is distorted when the signal is detected by a detection system with a bandwidth narrower than the signal bandwidth. Therefore, it is necessary to match the detection bandwidths of two arms to obtain equivalent trace distortions by small detection bandwidths. By this way, we can obtain distortion-free absorption spectra even with small detection bandwidth intentionally used to reduce signal noise. Since it is not easy to realize this with analog electronic components, we used large-bandwidth detectors (~10 MHz), oversampled both signals (2 MHz) and then limited their bandwidth by passing the detector signals through identical digital filters (100 kHz). A slight mismatch can also be compensated by the polynomial term in Eq. (6.3).

The true gas absorbance is then extracted from the measured quasi-absorbance by least-squares fitting the measured quasi-absorbance to the right-hand-side expression of Eq. (6.3). As typically performed in the simpler case as shown in figure 2.2, the laser frequency should be scanned sufficiently far (i.e., scanned frequency range >> transition linewidth, enabled by VCSELs' wide tunability) to distinguish resonant and non-resonant terms in Eq. (6.3). The fundamental difference between this scanned-wavelength scheme and fixed-wavelength schemes is the use of the spectral variation of gas resonant absorption to distinguish it from the non-resonant attenuation. The shape or relative values of the quasi-absorbance over a spectral range rather than the absolute values give the true gas absorption. The information contained in this continuous spectral scan allows fitting to the gas resonant absorption, and is thus more robust in hostile environments than the fixed-wavelength strategies which only acquire extinction information at several discrete laser wavelengths.

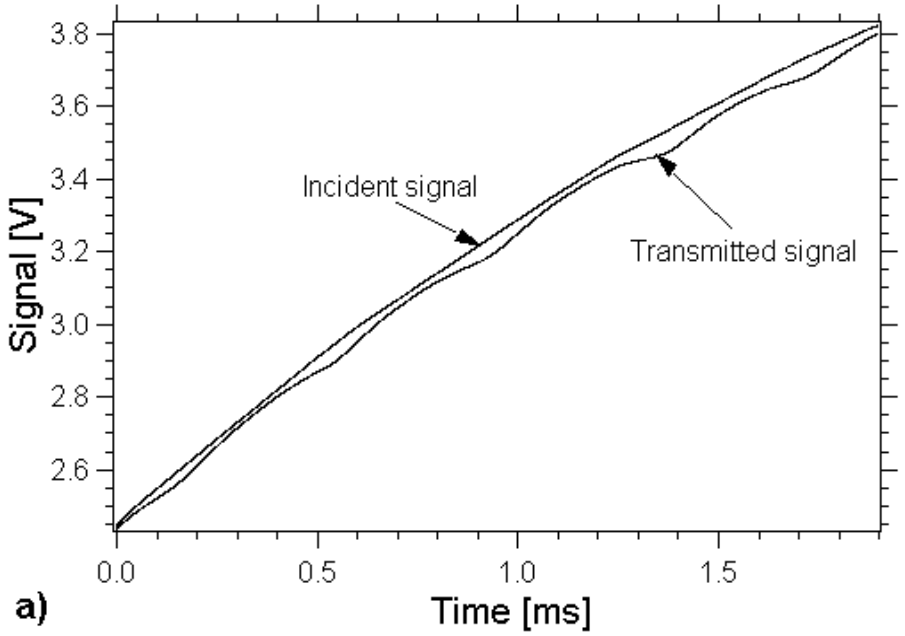

Figure 6.8a 50-sweep-averaged examples (~10-cm^{-1} frequency tuning) of transmitted and incident laser intensities recorded at a pressure of 10.9 bar and a temperature of 293 K.

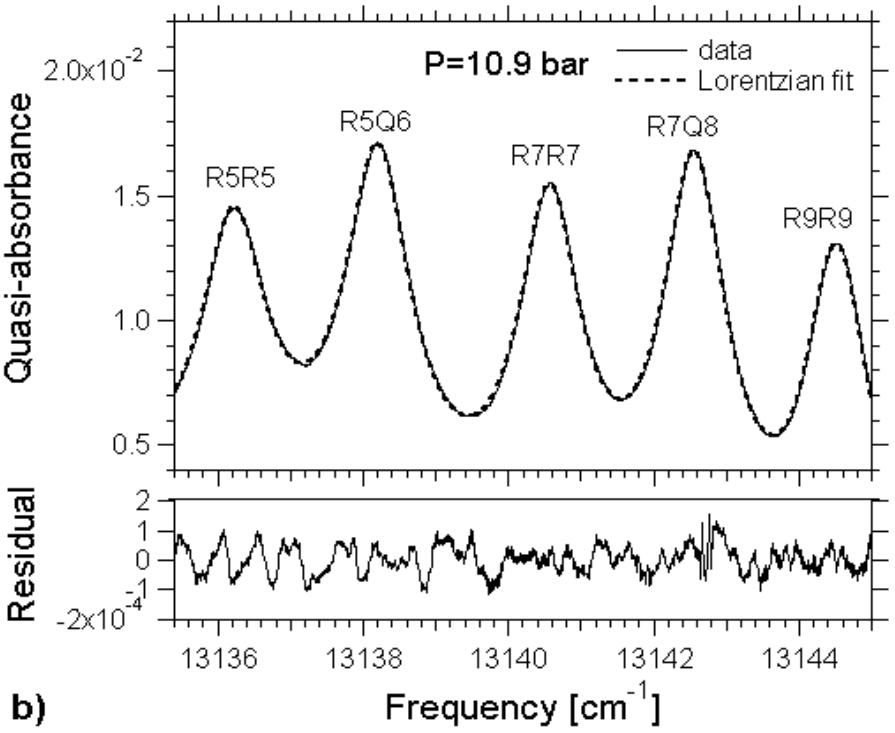

Figure 6.8b The top panel shows the reduced quasi-absorbance and a least-squares multi-transition Lorentzian fit. The bottom panel gives the fitting residual.

Figure 6.8a shows 50-sweep-averaged examples (~10-cm^{-1} frequency tuning) of incident and transmitted laser intensities recorded at a cell pressure of 10.9 bar and a temperature of 293 K. They gave the quasi-absorbance, $ln[I_0(\nu)/I(\nu)]$, shown in the top panel of figure 6.8b. The data trace in figure 6.8b was fit to the expression on the right side of Eq. (6.3) using the nonlinear Levenberg-Marquardt method. For high-pressure measurements made here, the lineshape is sufficiently described by a Lorentzian profile (Eq. 2.4). The three polynomial coefficients in the $P_2(\nu)$, the linestrength, collision width and shift for the five transitions (totally 18 parameters) were optimized in the fitting procedure to minimize the residual. The frequency scale was determined by correlating the measured peak positions recorded at 0.1 bar to known transition positions (Brown and Plymate 2000). The small fitting residual given in the bottom panel indicates the good quality of the fit. Table 6.1 lists the best-fit linestrengths and broadening coefficients of the R5Q6 ($\Delta N\ N''\ \Delta J\ J''$ notation), R7R7 and R7Q8 transitions. The accurate oxygen mole fraction in the dry air was unknown; a 21% oxygen mole fraction was assumed to calculate the linestrengths. The uncertainties of the measured linestrengths were thus not given. All measured parameters were within ±3% of those reported by Brown and Plymate (2000), indicating the effectiveness of this scanned-wavelength strategy for high-pressure measurements. For real applications, the same measurement technique can be used to obtain oxygen mole fraction, using known linestrengths at a known gas temperature.

Table 6.1. Linestrengths and broadening coefficients of the R5Q6, R7R7 and R7Q8 transitions in the oxygen A band at 293 K. The value in parentheses is the uncertainty in percent. The N_2- and self-broadening coefficients reported by Brown and Plymate (2000) were used to calculate corresponding air broadening coefficients in this table. A temperature dependence coefficient of 0.73 reported by Brown and Plymate (2000) was used to convert its broadening coefficients at 296 K to 293 K for comparison.

Oxygen A-band transitions	Linestrength S_i [10^{-4} cm^{-2}/bar]		Broadening Coefficient g_i [cm^{-1}/bar]	
	Ref*	Measured	Ref*	Measured
R5Q6	2.00 (1.0)	2.03	0.0507 (1.4)	0.0513 (1.0)
R7R7	1.82 (0.6)	1.83	0.0486 (0.9)	0.0486 (1.0)
R7Q8	2.19 (0.6)	2.16	0.0485 (0.9)	0.0492 (1.0)

Ref*: Brown and Plymate (2000)

An etalon noise with a free spectral range (FSR) of ~3.2 cm^{-1} and a peak amplitude of ~1×10^{-3} was observed in the traces of incident laser intensity. The ~3.2-cm^{-1} FSR corresponds to a ~1.5-

mm length scale, roughly the distance from the laser to the window of laser mount. Improvements in laser packaging such as antireflection coating or wedged window might eliminate this etalon. However, the influence of this etalon was effectively eliminated by the common-mode noise suppression capability of the dual-beam measurement scheme.

6.3.2 WMS 2*f* measurements

Because of the small linestrengths of the magnetic-dipole transitions of the oxygen A band, modulation spectroscopy techniques (wavelength modulation or frequency modulation) have generally been used to enhance the detection sensitivity. However, for the high-pressure measurements considered here, the large linewidth of the collisionally broadened transition prohibits frequency modulation, and thus the appropriate modulation scheme is wavelength-modulation spectroscopy. We therefore demonstrate WMS 2*f* measurements of high-pressure oxygen to establish sensors for the low oxygen absorption expected in many practical systems of interest.

Although the current tuning of optical frequency through variation of carrier number density can be very fast, its tuning amplitude is very limited. Only thermal tuning can modulate the laser wavelength sufficiently far for high-pressure measurements. Thus the modulation frequency is limited by the thermal time constant of VCSELs used (~100 kHz in our case as shown in figure 6.4).

Figure 6.9 presents several single-sweep 2*f* traces of the oxygen doublet R7R7 and R7Q8 recorded at pressures ranging from 3.4 to 10.5 bar. The laser power variation resulting from the ramp modulation was corrected for these 2*f* traces to provide the true relative signal intensities of the two oxygen transitions. The peak amplitude of the wavelength modulation is ~0.31 cm^{-1}. The modulation index (defined by Eq. (2.26)) decreased from to 1.85 to 0.61 with increasing pressures. The reduction of 2*f* signal amplitude with increasing pressure was mainly due to this decrease of modulation index. The relatively small modulation amplitude was intended to reduce the effect of the abovementioned ~3.2 cm^{-1} etalon, not limited by the VCSEL's wavelength tunability. The red shift of line positions was the result of a combination of pressure shift and laser-case-temperature drift. The minimum detectable absorbance of $\sim 1\times10^{-4}$ observed corresponds to ~800 ppm-m oxygen detectivity at room temperature, and was limited by etalon noise rather than by laser excess noise.

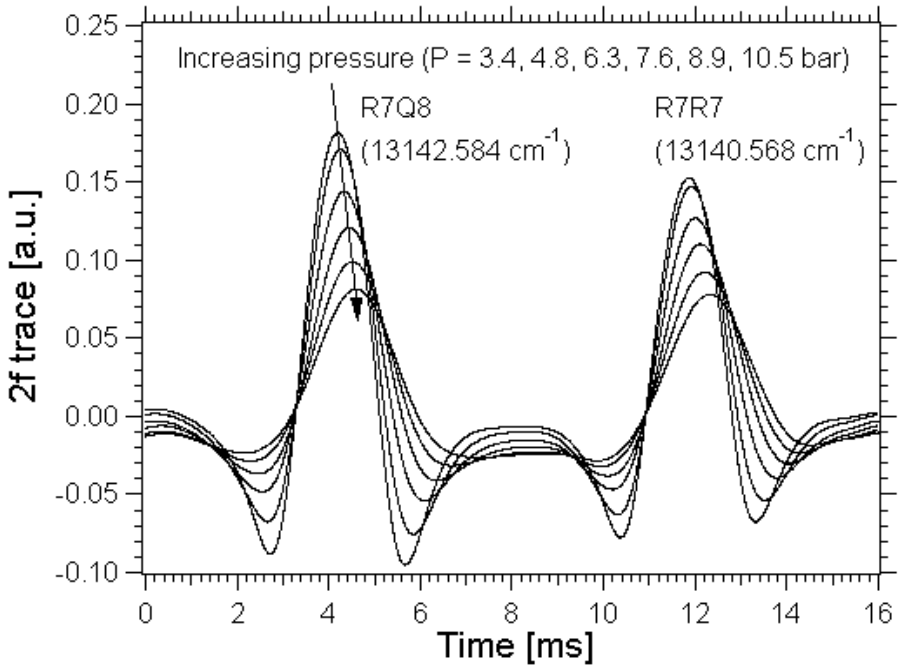

Figure 6.9. Sample single-sweep *2f* traces recorded at different pressures with a constant wavelength modulation (~0.31 cm^{-1} peak amplitude). The laser power variation resulting from the ramp modulation was corrected. The line positions shown are those at zero pressure (Brown and Plymate 2000).

An atmospheric room-air WMS measurement (~5-cm beam path) was made to check the detectivity of a VCSEL-based setup free from etalon noise from the lens and the cell. An off-axis paraboloidal reflector was used to collimate the laser beam to eliminate the etalon noise of amplitude $\sim 1\times10^{-4}$ observed using the antireflection-coated lens. A minimum detectable absorbance of $\sim 4\times10^{-6}$, corresponding to ~30 ppm-m oxygen detectivity at room temperature, was obtained with a 300-μs time constant and 100-sweep averaging (~5-Hz effective bandwidth). This result is comparable to the ~20 ppm-m detectivity reported for edge-emitting lasers (Weldon *et al.* 1997).

The collisional broadening coefficients of oxygen by combustion major products N_2, O_2, CO_2, H_2O are almost the same (Brown and Plymate 2000; Pope *et al.* 2000; Fanjoux *et al.* 1994), and thus the transition linewidth can be approximated as only a function of total pressure and temperature. This attribute may greatly simplify the application of modulation spectroscopy techniques to oxygen detection in combustion environments.

6.4 Discussion

A large current-tuning wavelength range can also be obtained by multi-section distributed Bragg reflector (DBR) lasers. Multi-section DBR lasers use different sections for gain, mode phase shifting and frequency-selective Bragg reflector mirrors, and thus can provide large wavelength tuning range (~ 100 nm) with high side-mode suppression (Coldren and Corzine 1987; Upschulte *et al.* 1999). In addition, very fast tuning can be obtained because the tuning is based on either the carrier effect when a forward current is applied or the electro-optic effect from a reverse bias to the phase-shift and Bragg reflector sections. However, such lasers require complicated manufacturing processes and thus are expensive. In addition, several current drivers may be required to drive different sections.

In contrast, VCSELs typically have low manufacturing cost and are easy to use. VCSELs are also particularly well-suited to continuous wavelength tuning due to their large longitudinal mode spacing. Therefore, mode-hopping behavior simply does not happen. Many groups have demonstrated MEMS-based widely tunable VCSELs (a subgroup of the new-generation ECDLs). For example, a continuous tuning range of 18 nm was reported by the Stanford Professor Harris' research group using a monolithic micromachined deformable membrane top mirror (Larson *et al.* 1996). This approach changes the cavity length by electrically deforming the membrane top mirror rather than by the thermal effect, thus microsecond wavelength switching speed has been demonstrated (Sugihuo *et al.*1998). The recent Bandwidth9's design (figure 6.1) made one significant step further by monolithically growing the tuning cantilever together with the other parts of the laser. This miniature external cavity approach may be especially valuable for longer wavelength lasers, which have relatively poor temperature performance due to the strong Auger recombination process.

The large tuning range of 2-3 nm achieved in this work by current tuning results from the resistive heating of the large series resistance associated with DBR mirrors. However, since this large series resistance is highly undesirable for high-speed applications such as telecommunication, VCSELs fabricated with special mirror design for these applications may have less than 50-ohm series resistance. The readers are cautioned that a large current-tuning frequency range may not be obtained from such VCSELs.

Direct-absorption spectroscopy techniques, as presented above, may have significant potential for other applications such as H_2O-absorption-based combustion diagnostics, which may yield

important parameters such as temperature and H_2O concentration. Fixed-wavelength H_2O-absorption diode-laser sensing has been proposed to monitor high-pressure combustors (Nagali and Hanson 1997) and successfully demonstrated in the diagnostics of pulse detonation engines (Sanders *et al.* 2000b). Nondispersive broadband H_2O-absorption sensing (Seitzman *et al.* 1998) has also been proposed. However, we believe the scanned-wavelength strategy exploiting VCSELs' rapid and wide wavelength tunability will provide better performance in hostile combustion environments and have lower cost.

Chapter 7 *Conclusions and Future Work*

7.1 Summary of 2.3-μm *in situ* CO absorption sensors

The 2.3-μm room-temperature continuous-wave (Al)InGaAsSb/GaSb diode lasers from Sarnoff Corporation and Sensors Unlimited Inc. accessed some transitions of CO first-overtone band ($v' = 2 \leftarrow v'' = 0$). These Fabry-Perot lasers were research-grade prototypes. They had very short lifetime and exhibited mode-hopping behavior. However, some of these devices could operate single mode (~25-dB side mode suppression) under specific current and temperature combinations. With these lasers, *in situ* CO measurements were successfully demonstrated in both the exhaust duct (79 cm above the burner, ~470 K) and the immediate post-flame zone (1.5 cm above the burner, 1820—1975 K) of an atmospheric-pressure, premixed, laminar, C_2H_4-air flat-flame burner.

At the exhaust-duct conditions, many transitions (e.g., R(4), R(6), R(10), R(11), and R(15)) are isolated from water and carbon dioxide interference. Because of its minimum temperature sensitivity and available laser access, the R(15) transition at 4311.96 cm^{-1} was selected for the exhaust-duct measurements. Both direct-absorption and wavelength-modulation spectroscopy techniques were implemented. A detection limit of 1.5 ppm-m was achieved using direct-absorption spectroscopy with a 50-kHz detection bandwidth and a 50-sweep average (0.1-s total measurement time). With wavelength-modulation spectroscopy techniques, a sensitivity of 0.1 ppm-m was achieved with a ~500 Hz detection bandwidth and a 20-sweep average (0.4-s total measurement time). The minimum CO concentration was obtained at a fuel/air equivalence ratio of ~0.7. If the equivalence ratio was lowered further, the average CO concentration became larger, and flame instability was observed. Though the measurements in the exhaust duct were initially designed for combustion emission-compliance monitoring applications, the achieved sensitivity even enables ambient-air quality monitoring and on-road remote sensing of vehicle exhaust. Therefore, some experiments were quickly conceived to demonstrate these applications. However, the laser failed before these experiments could be performed.

The experiment in the immediate post-flame zone was designed for its potential applications in combustion control and engine diagnostics. The interference from H_2O and CO_2 is much more severe at flame temperature. The R(30) transition at 4343.81 cm^{-1} is relatively free of interference according to the HITEMP96 database and thus selected for the experiment. CO concentration was

measured at equivalence ratios ranging from 1.44 to 0.62. The measurements in the fuel-rich flames agreed with theoretical equilibrium predictions. The measured CO concentrations in the fuel-lean flames were larger than the corresponding equilibrium values because of the cool-edge effect and possible superequilibrium conditions. Quantitative measurements were obtained at equivalence ratios down to 0.83 (366-ppm minimum CO concentration) with an only 11-cm beam path. For measurements at equivalence ratios smaller than 0.8, though the CO absorption feature was clearly observed, better understanding of the H_2O and CO_2 spectral interference and improved detectivity are required for confident quantitative results. Unfortunately, the two lasers which could access the R(30) transition both failed; one stopped lasing, and the other's single-mode operation region drifted away from the R(30) transition.

Regardless of their delicate nature and short lifetime, these research-grade lasers exhibited very low noise, which enabled the above encouraging results. These results suggest that this new strategy of *in situ* CO sensing based on 2.3-μm diode lasers is very promising.

7.2 Summary of on-road remote sensing of CO in vehicle exhaust

The potential of 2.3-μm CO absorption sensors for on-road remote sensing of CO in vehicle exhaust is examined. On-road remote sensors of vehicle exhaust require a much higher measurement repetition rate than that required for continuous emission monitoring of stationary sources. Using a WMS technique, a sensitivity of 1 ppm-m which corresponds to 20 ppm sensitivity with optimum alignment to typical 5-cm-diameter tailpipes was demonstrated in the exhaust duct of a laboratory burner with a detection bandwidth of ~1.5 kHz. Though in the demonstration measurement a scanned-mean-frequency scheme was used with a measurement repetition rate of 100 Hz, a fixed-mean frequency scheme can increase the measurement repetition rate to the detection bandwidth, i.e., ~1.5 kHz, without sacrificing the signal-to-noise ratio. This sensitivity is 2-3 orders of magnitude better than existing on-road remote sensors and enables quantitative measurements of CO effluent from even the cleanest combustion-powered vehicles. However, the laser failed before we could apply this sensor to characterizing real vehicle exhaust.

Absorption spectroscopy is a line-of-sight technique that traditionally requires uniform concentration profile and a known or uniform temperature profile along the light beampath. The exhaust concentration and temperature profiles are unknown, non-uniform and quickly varying for on-road remote sensing of vehicle exhaust. The industry standard ratios CO to CO_2 rather than

measures CO itself to eliminate the effect of non-uniform concentration profile. However, the effects of the varying and non-uniform temperature and composition profiles on the remote sensing have not been addressed. Therefore, the influence of the exhaust-gas temperature and composition on the inferred CO concentration was investigated. A novel approach that matches the temperature and composition dependences of CO and CO_2 absorption and thus obtains temperature- and composition-independent measurements of the CO/CO_2 ratio is proposed for the first time. This strategy reduces these effects to ±3% in the typical exhaust temperature range of 300-700 K. Thus, sensitive and remote measurements of vehicular CO effluent are possible without knowing the exact exhaust temperature or composition. This new strategy to eliminate or mitigate the temperature- and composition-dependence can also be applied to many other applications. The temperature influence is further exploited to suggest a two-line CO_2-absorption thermometry method with large temperature sensitivity to identify cold-start vehicles.

7.3 Summary of high-pressure oxygen sensing with VCSELs

Though VCSELs have been used for gas sensing by several groups previously, the goal of the previous work was simply to replace conventional single-mode edge-emitting lasers with less expensive laser sources. This thesis for the first time utilized the fast and large wavelength tunability of some VCSELs by varying the injection current and demonstrated a wavelength-scanning high-pressure oxygen sensor by exploiting this characteristic. The large tuning range (>30 cm^{-1} instead of 1-2 cm^{-1} with conventional edge-emitting lasers) results from the electrical heating associated with the large series resistance of distributed Bragg reflector mirrors. Because of their small cavity volume, VCSELs have a much smaller thermal time constant than conventional edge-emitting lasers. This small thermal time constant enables high tuning frequency (~100 kHz demonstrated in this thesis). Other VCSEL characteristics (e.g., relative intensity noise and transverse mode behavior), which are important to high-resolution absorption spectroscopy, were also investigated in this thesis. It was found these VCSELs have comparable noise performance to conventional single-mode edge-emitting lasers with the same output power. The higher-order transverse modes can be suppressed by setting the laser case temperature to higher than 35 °C, enabling a larger single-transverse-mode tuning range.

Both wavelength-scanning direct-absorption and WMS strategies for high-pressure oxygen sensing were demonstrated here. These new strategies can be easily extended to measuring other species in high-pressure environments, only limited by the laser wavelength availability. The minimum detectable absorbance obtained of $\sim 1\times10^{-4}$ was limited by etalon noise. In an etalon-

free room-air measurement, a minimum detectable absorbance of ~4×10^{-6} was achieved with an effective bandwidth of 5 Hz. This etalon-free sensitivity is sufficient to satisfy most combustion applications such as aeropropulsion gas-turbine diagnostics.

7.4 Future work

The CO measurements in both the exhaust duct and the immediate post-flame zone of a flat-flame burner suggest that absorption sensors based on the 2.3-μm Sb-based diode lasers are an attractive alternative to commercial sensors using the second-overtone transitions near 1.6 μm. The increased sensitivity of the 2.3-μm sensors enable many important applications such as continuous emission monitoring of municipal waster combustors, ambient-air quality monitoring, on-road remote sensing of vehicle exhaust, and engine diagnostics. Demonstration measurements of these applications will be of much interest. Since CO is both an important air pollutant and a key indicator of combustion efficiency, it will be very valuable to develop a combustion control strategy based on these CO sensors and the relatively mature H_2O-based diagnostics tools. However, new sources of 2.3-μm lasers need to be found.

A novel temperature-insensitive strategy to eliminate or mitigate the requirements of uniform or known temperature profile for diode-laser absorption sensors is proposed here. This strategy can not only be used for the on-road remote sensing of vehicle exhaust, but can also be applied to many other applications such as smog check and quality control in engine assembly lines to improve the time response and to eliminate the sampling manifold. It will be very valuable to demonstrate this new gas-sensing strategy.

Exploiting the fast and broad tunability of some VCSELs, a new wavelength-scanning high-pressure oxygen sensing strategy with its potential application to high-pressure combustors is demonstrated. Further use of this sensor in real high-pressure propulsion or utility combustors will be of great interest.

VCSELs are currently commercially available with some wavelengths between 0.7 μm and 1 μm based on the AlGaAs/GaAs and InGaAs/GaAs material systems. Widely tunable VCSELs around 1.3 μm and 1.5 μm are expected to be commercially available in the near future. This extension of the wavelength range will enable many new gas-sensing strategies, e.g., wavelength-scanning high-pressure water measurements.

Relative Intensity Noise of Diode Lasers

Diode-laser relative intensity noise (RIN) comes from the random carrier and photon recombination and generation processes inherent in each laser. Diode-laser RIN usually limits the best sensitivity that can be achieved with absorption spectroscopy.

A.1 Definition

There are two commonly used definitions of RIN. One is the total relative intensity noise over the whole detection bandwidth:

$$RIN = \frac{\left\langle dP(t)^2 \right\rangle}{P_0^2},$$

or, expressed in dB,

$$RIN = 10\log\left(\frac{\left\langle dP(t)^2 \right\rangle}{P_0^2}\right) \quad \text{(dB)} \tag{A.1}$$

where $\left\langle dP(t)^2 \right\rangle$ is the mean-square optical power fluctuation, P_0 is the average laser power.

The other is the relative intensity noise per unit bandwidth:

$$RIN = \frac{S_{dP}}{P_0^2},$$

or, expressed in dB,

$$RIN = 10\log\left(\frac{S_{dP}}{P_0^2}\right) \quad \text{(dB/Hz)} \tag{A.2}$$

where S_{dP} is the single-sided spectral density of the total noise power. Mathematically, it is defined as

$$\left\langle dP(t)^2 \right\rangle = \int_0^\infty S_{dP}(f)\, df \ .$$

This second definition is more popular, and thus is used below. We will find later that there is actually a subtle difference between the actual measured RIN and this widely used definition.

A.2 Measurement schematic

Figure A.1 shows the block diagram for measuring the RIN. The laser diode is operated in continuous-wave mode. A broadband photodiode is used to detect the optical input. The ac (noise) and dc (average power) parts are separated, individually amplified and measured to give RIN.

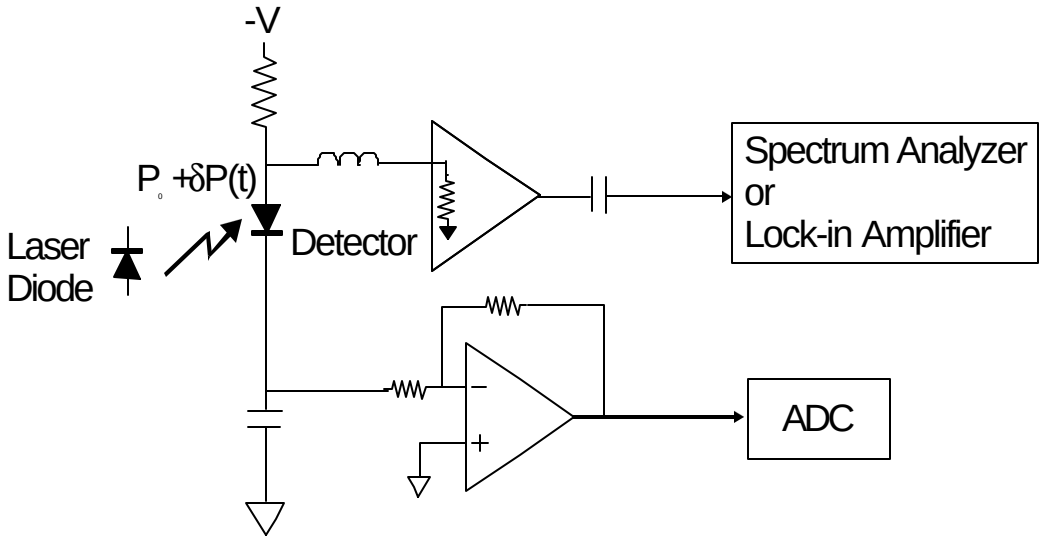

Figure A. 1 Block diagram for RIN measurement.

A.3 Theoretical background

The laser noise can be assumed to originate from the shot noise associated with the discrete random flow of particles into and out of the carrier and photon reservoirs. The Langevin shot noise model can be used to quantify the above shot noise. When we derive the laser dynamics, the current variation is the ac driving source (Eq. (3.18)). By introducing the Langevin noise to the differential rate equations as the ac driving sources for the photon and carrier densities:

$$\frac{d}{dt}\begin{bmatrix} dN \\ dN_p \end{bmatrix} = \begin{bmatrix} -g_{NN} & -g_{NP} \\ g_{PN} & -g_{PP} \end{bmatrix}\begin{bmatrix} dN \\ dN_P \end{bmatrix} + \frac{h_i}{qV}\begin{bmatrix} dI \\ 0 \end{bmatrix}, \tag{A.3}$$

the laser RIN noise can be derived using standard Fourier analysis:

$$RIN = \frac{S_{dP}}{P_0^2} = \frac{2h\nu}{P_0}\left[\frac{a_1 + a_2\omega^2}{\omega_R^4}\left|H(\omega)\right|^2\right] + \frac{2h\nu}{P_0} = RIN' + \frac{2h\nu}{P_0}, \tag{A.4}$$

where a_1 and a_2 are intrinsic parameters of each laser, and ω_R is the laser relaxation frequency. $H(\omega)$ $(= \frac{\omega_R^2}{\omega_R^2 - \omega^2 + j\omega\gamma})$ and γ are the transfer function and the damping factor introduced in chapter 3. The $\frac{2h\nu}{P_0}$ term is the quantum noise or shot noise floor.

During the detection process, some photons are detected and some are not. This random process generates some partition noise. The noise spectral density of the detected photocurrent with the partition noise contribution is:

$$dI_{\det}^2(f) = h_{\det}^2 (q/hn)^2 S_{dP}(f) + 2(1-h_{\det}) q I_{\det}, \tag{A.5}$$

here all spectral densities are single-sided, and $I_{\det} = h_{\det}(q/hn)P_0$. Since the noise is usually measured with a spectrum analyzer, which generally measures the electrical power of the input signal with dBm/Hz as unit, Eq. (A.4) is converted to electrical power by multiplying the load resistance:

$$S_{\det}^2(f) = h_{\det}^2 (q/hn)^2 S_{dP}(f) R_{load} + 2(1-h_{\det}) q I_{\det} R_{load} \tag{A.6}$$

The ac amplifier also adds noise. The performance of the amplifier is usually characterized by noise figure, which is defined as the ratio of the total output noise of the amplifier caused by both the amplifier and the source to the output noise caused by the source alone. Because this ratio depends on the source noise, the source noise is specified to be the available output power (kT, k: Boltzmann constant, T: absolute temperature) of a resistor at 290 K, i.e., -174 dBm/Hz or 4.0×10^{-18} mW/Hz. (Note: this definition of noise figure is widely used, e.g., in commercial noise figure meters; however there are some other versions of definition in the literature).

Therefore, the total noise at the output of the amplifier is

$$S_{total}^2(f) = G^2\left[h_{\det}^2 (q/hn)^2 S_{dP}(f) R_{load} + 2(1-h_{\det}) q I_{\det} R_{load} + NF(4.0E-18) mW/Hz\right] \tag{A.7}$$

where G is the amplifier gain. To measure this noise accurately, this total noise should be comparable to or larger than the detection sensitivity of the spectrum analyzer. That is why the amplifier is used. The maximum amplification is limited by the maximum allowable input of the spectrum analyzer.

The dc part of the measurement gives the amplified average signal:

$$P_{electrical} = G^2\left[I_{\det}^2 R_{load}\right] \tag{A.8}$$

The ratio of Eqns (A.7) and (A.8) is defined as RIN_{system}:

$$RIN_{system} = \frac{S_{dP}(f)}{P_0^2} + (1-h_{\det})\frac{2q}{I_{\det}} + \frac{NF\,(4.0E-18) mW/Hz}{I_{\det}^2 R_{load}} \tag{A.9}$$

Substituting Eq. (A.4), obtain

$$\begin{aligned} RIN_{system} &= RIN' + \frac{2h\nu}{P_0} + (1-\eta_{\det})\frac{2q}{I_{\det}} + \frac{NF(4.0E-18)mW/Hz}{I_{\det}^2 R_{load}} \\ &= RIN' + \frac{2q}{I_{\det}} + \frac{NF(4.0E-18)mW/Hz}{I_{\det}^2 R_{load}} \\ &= RIN' + S_{shot} + S_{thermal} \end{aligned} \tag{A.10}$$

$\frac{2q}{I_{\det}}$ is recognized as the shot noise of the detector current. The last term represents the amplifier thermal noise.

A.4 Measurement procedure

The laser RIN is obtained by first measuring the RIN_{system} and then subtracting the shot and thermal noise terms:

$$RIN_{laser} = RIN_{system} - S_{shot} - S_{thermal} \tag{A.11}$$

The thermal noise is measured by blocking the laser beam to the detector (by this way, the noise of the spectrum analyzer is also eliminated in the final measured RIN_{laser}). The shot noise is calculated from its definition $\frac{2q}{I_{\det}}$.

Here comes a subtle issue about the laser RIN. Comparing Eq. (A.11) with Eq. (A.10), we can find that the finally measured RIN_{laser} is actually RIN', i.e., the measured RIN_{laser} is different from the widely used definition $RIN = \frac{S_{dP}}{P_0^2}$. Indeed it is $\frac{S_{dP}}{P_0^2} - \frac{2h\nu}{P_o}$ (see Eq. (A.4)). **Eq.** (A.11) **gives the RIN definition for both RIN measurement and application.** This definition is actually easier to use than that defined in Eq. (A.2), since the optical shot noise $\frac{2h\nu}{P_0}$ is already included in the electrical shot noise $\frac{2q}{I_{\det}}$, which is the sum of the optical shot noise and the detection partition noise.

Bibliography

M.G. Allen, "Diode laser absorption sensors for gas-dynamic and combustion flows," Meas. Sci. Technol. **9**, 545-562 (1998).

B.H. Armstrong, "Spectrum line profiles: the Voigt function," J. Quant. Spectrosc. Radiat. Transfer **7**, 61-88 (1967).

D.S. Baer, V. Nagali, E.R. Furlong, and R.K. Hanson, " Scanned- and fixed-wavelength absorption diagnostics for combustion measurements using multiplexed diode lasers," AIAA Journal **34**, 489-493 (1996).

A.N. Baranov, Y. Rouillard, G. Boissier, P. Grech, S. Gaillard, and C. Alibert, "Sb-based monolithic VCSEL operating near 2.2 μm at room temperature," Electronics Letters **34**, 281-282 (1998).

B.R. Bennett, R.A. Soref, and J.A. Del Alamo, " Carrier-induced change in refractive index of InP, GaAs, and InGaAsP," IEEE J. of Quantum Electronics **26**, 113-122 (1990).

W.W. Bewley, C.L. Felix, I. Vurgaftman, E.H. Aifer, L.J. Olafsen, J.R. Meyer, L. Goldberg, and D.H. Chow, "Mid-infrared vertical-cavity surface-emitting lasers for chemical sensing," Applied Optics **38**, 1502-1505 (1999).

G.A. Bishop, J.R. Starkey, A. Ihlenfeldt, W.J. Williams, and D.H. Stedman, "IR long-path photometry: a remote sensing tool for automobile emissions," Anal. Chem. **61**, 671A-677A (1989).

G.A. Bishop, D.H. Stedman, J.E. Peterson, T.J. Hosick, and P.L. Guenther, "A cost-effectiveness study of carbon monoxide emissions reduction utilizing remote sensing," J. Air Waste Manage. Assoc. **43**, 978-988 (1993).

G.A. Bishop and D.H. Stedman, "Motor vehicle emission variability," J. Air Waste Manage. Assoc. **46**, 667-675 (1996).

G.C. Bjorklund, "Frequency-modulation spectroscopy: a new method for measuring weak absorptions and dispersions," Opt. Lett. **5**, 15-17 (1980).

T. Bleuel, M. Brockhaus, J. Koeth, J. Hofmann, R. Werner, and A.W. Forchel, "GaInAsSb /AlGaAsSb: single-mode DFB lasers for gas sensing in the 2-μm wavelength range," Proc. SPIE **3858**, 119-124 (1999).

J.-P. Bouanich and C. Brodbeck, "Mesure des largeurs et des deplacements des raies de la bande $0 \rightarrow 2$ de CO autoperturbe et perturbe par N_2, O_2, H_2, HCl, NO et CO_2," J. Quant. Spectrosc. Radiat. Transfer **13**, 1-7 (1973)

D. Bradley and K. J. Matthews, "Measurement of high gas temperatures with fine wire thermocouples," J. Mech. Eng. Sci. **10**, 299-305 (1968).

A. Brock, N. Mina-Camilde, C. Manzanares, "Vibrational spectroscopy of C-H bonds of C_2H_4 liquid and C_2H_4 in liquid argon solutions," J. Phys. Chem. **98**, 4800-4808 (1994).

J. Brouwer, B. A. Ault, J. E. Bobrow, and G. S. Samuelsen, "Active control for gas turbine combustors," The Twenty-Third Symposium (International) on Combustion, 1087-1092 (1990).

L.R. Brown and C. Plymate, "Experimental line parameters of the oxygen A band at 760 nm," Journal of molecular spectroscopy **199**, 166-179 (2000).

D.M. Bruce and D.T. Cassidy, "Detection of oxygen using short external cavity GaAs semiconductor diode lasers," Appl. Opt. **29**, 1327-1332 (1990).

S.H. Cadle and R.D. Stephens, "Remote sensing of vehicle exhaust emissions," Environ. Sci. Technol. **28**, 258A-264A (1994).

S.H. Cadle, R.A. Gorse, Jr., T.C. Belian, and D.R. Lawson, "Real-world vehicle emissions: a summary of the seventh coordinating research council on-road vehicle emissions workshop, " J. Air Waste Manage. Assoc. **48**, 174-185 (1998).

S.H. Cadle, R.A. Gorse, Jr., T.C. Belian, and D.R. Lawson, "Real-world vehicle emissions: a summary of the eighth coordinating research council on-road vehicle emissions workshop," J. Air Waste Manage. Assoc. **49**, 242-255 (1999).

California Environmental Protection Agency Air Resources Board, "California exhaust emission standards and test procedures for 2001 and subsequent model passenger cars, light-duty trucks, and medium-duty vehicles," adopted on August 5,1999.

J.G. Calvert, J.B. Heywood, R.F. Sawyer, J.H. Seinfeld, "Achieving acceptable air quality: some reflections on controlling vehicle emissions," Science **261**, 37-45 (1993).

F. Capasso, A. Tredicucci, C. Gmachl, D.L. Sivco, A.L. Hutchinson, A.Y. Cho, "High-performance superlattice quantum-cascade lasers," IEEE J. of Selected Topics in Quantum Electronics **5**, 792-808 (1999).

C. J. Chang-Hasnain, "Tunable VCSEL," IEEE J. of Selected Topics in Quantum Electronics **6**, 978-987 (2000).

H. K. Choi, G. W. Turner, and S. I. Eglash, "High-power GaInAsSb/AlGaAsSb multiple-quantum-well diode lasers emitting at 1.9 μm," IEEE Photon. Technol. Lett. **6**, 7-9 (1994).

K.D. Choquette, "Selectively oxidized VCSELs go single-mode," Laser Focus World **36,** No. 5, 251-254 (2000).

S.L. Chuang, "Physics of optoelectronic devices," (Wiley, New York, 1995).

L.A. Coldren and S.W. Corzine, "Continuously-tunable single-frequency semiconductor lasers," IEEE Journal of Quantum Electronics **QE-23**, 903-908 (1987).

L.A. Coldren, S.W. Corzine, "Diode lasers and photonic integrated circuits," John Wiley & Sons, New York (1995).

L.A. Coldren, E. Hall, S. Nakagawa, "Advances in long-wavelength single-mode VCSELs and packaging approaches for single-mode fiber applications," 51st ECTC (2001).

S.R. Drayson, "Rapid computation of the Voigt profile," J. Quant. Spectrosc. Radiat. Transfer 16, 611-614 (1976).

J. Faist, F. Capasso, D.L. Sivco, C. Sirtori, A.L. Hutchinson, and A.Y. Cho, "Quantum cascade laser," Science **264**, 553-556 (1994).

G. Fanjoux, G. Millot, R. Saint-Loup, and R. Chaux, "Coherent anti-Stokes Raman spectroscopy study of collisional broadening in the O_2-H_2O Q branch," J. Chem. Phys. **101**, 1061-1071 (1994).

S. Fujii, S. Tomiyama, Y. Nogami, M. Shirai, H. Ase, and T. Yokoyama, "Fuzzy combustion control for reducing both CO and NOx from flue gas of refuse incineration furnace," JSME International Journal (Series C) **40**, 279-284 (1997)

E.R. Furlong, R.M. Mihalcea, M.E. Webber, D.S. Baer and R.K. Hanson, "Diode-laser sensors for real-time control of pulsed combustion systems," *AIAA Journal* **37,** 732-737 (1999).

D. Garbuzov, H. Lee, V. Khalfin, R. Martinelli, R. Menna, and J. Connolly, "2.0 – 2.4 μm High-Power Broaden Waveguide SCH-QW InGaAsSb/AlGaAsSb Diode Lasers," CLEO/EUROPE – European Quantum Electronics Conference, Glasgow, Scotland, United Kingdom, paper CWL2 (1998).

D. Garbuzov, R. Menna, M. Maiorov, H. Lee, V. Khalfin, L. Dimarco, D. Capewell, R. Martinelli, G. Belenky, and J. Connolly, "2.3-2.7 μm room temperature CW-operation of InGaAsSb/AlGaAsSb broad-contact and single-mode ridge-waveguide SCH-QW diode lasers," SPIE Proc. **3628**, 124-129 (1999).

C. Gmachl, A. Tredicucci, D.L. Sivco, A.L. Hutchinson, F. Capasso, A.Y. Cho, "Bidirectional semiconductor laser," Science **286**, 749-752 (1999).

M. Guden and J. Piprek, "Material parameters of quaternary III-V semiconductors for multilayer mirrors at 1.55 μm wavelength," Modelling Simul.Mater. Sci. Eng. **4**, 349-357 (1996).

E. Hall, S. Nakagawa, G. Almuneau, J.K. Kim, L.A. Coldren, "Selectively etched undercut apertures in AlAsSb-based VCSELs," IEEE Photon. Technol. Lett. **13**, 97-99 (2001).

J.S. Harris, "Tunable long-wavelength vertical-cavity lasers: the engine of next-generation optical networks," IEEE Journal on Selected Topics in Quantum Electronics **6**,1145-1160 (2000).

J. M. Hartmann, L. Rosenmann, M. Y. Perrin, and J. Taine, "Accurate calculated tabulations of CO line broadening by H_2O, N_2, O_2, and CO_2 in the 200-3000-k temperature range," Appl. Opt. **27**, 3063-3065 (1988).

G. Hasnain, K. Tai, L. Yang, Y. H. Wang, R. J. Fischer, J. D. Wynn, B. Weir, N. K. Dutta, and A. Y. Cho, "Performance of gain-guided surface emitting lasers with semiconductor distributed Bragg reflectors," IEEE Journal of Quantum Electronics **27**, 1377-1385 (1991).

J. Humlicek, "Optimized computation of the Voigt and complex probability functions," J. Quant. Spectrosc. Radiat. Transfer **27**, 437-444 (1982).

J. A. Jahnke, "Continuous emission monitoring," Van Nostrand Reinhold, New York, 31-58 (1993).

J.L. Jimenez, M.D. Koplow, D.D. Nelson, M.S. Zahniser, and S.E. Schmidt, "Characterization of on-road vehicle NO emissions by a TILDAS remotes sensor," J. Air Waste Manage. Assoc. **49**, 463-470 (1999).

J. D. Kilgroe, L. P. Nelson, P. J. Schindler, and W. S. Lanier, "Combustion control of organic emissions from municipal waste combustors," Combust. Sci. and Technol. **74**, 223-244 (1990).

M. Kroll, J.A. McClintock, and O. Ollinger, "Measurement of gaseous oxygen using diode laser spectroscopy," Appl. Phys. Lett. **51**, 1465-1467 (1987).

H. Kroemer, "A proposed class of heterojunction injection lasers," Proceedings Of The IEEE, 1782-1783 (1963).

R.T. Ku, E.D. Hinkley, and J.O. Sample, "Long-path monitoring of atmospheric carbon monoxide with a tunable diode laser system," Appl. Opt. **14**, 854-861 (1975).

G.K. Kuang, G. Bohm, N. Graf, M.Grau, G. Rosel, R. Meyer, and M.-C. Amann, "InGaAs-InGaAlAs-InP 2.21 μm diode lasers grown in MBE," CLEO 2001, paper CML1.

M.C. Larson, A.R. Massengale and J.S. Harris, "Continuously tunable micromachined vertical cavity surface emitting laser with 18 nm wavelength range," Electronics Letters **32**, 330-332(1996).

J.Y. Law and G.P. Agrawal, "Mode-partition noise in vertical-cavity surface-emitting lasers," IEEE Photonics Technology Letters **9**, 437-439 (1997).

M. Maiorov, J. Wang, D. Baer, H. Lee, G. Belenky, R. Hanson, J. Connolly, D. Garbuzov, "New Room Temperature CW InGaAsSb/AlGaAsSb QW Ridge Diode Lasers and Their Application to CO Measurements near 2.3 μm," SPIE Proc. **3855**, 62-70 (1999).

J. S. Major, J. S. Osinski, and D. F. Welch, " 8.5 W CW 2.0 μm InGaAsP laser diodes," Electron. Lett. **29**, 2112-2214 (1993).

R.U. Martinelli, R.J. Menna, P.K. York, D.Z. Garbuzov, H. Lee, J.H. Abeles, N. Morris, J.C. Connolly, S.Y. Narayan, J.S. Vermaak, G.H. Olsen, D.E. Cooper, C.B. Carlisle, H. Riris, A.L. Cook, "Tunable single-frequency III-V semiconductor diode laser with wavelengths from 0.76 to 2.7 μm," SPIE **2834**, 2-16 (1996).

R.M. Mihalcea, D. S. Baer, and R. K. Hanson, "A diode-laser absorption sensor system for combustion emission measurements," Meas. Sci. Technol. **9**, 327-338 (1998).

G.Modugno and C. Corsi, "Water vapour and carbon dioxide interference in the high sensitivity detection of NH3 with semiconductor diode lasers at 1.5 μm," Infrared Physics & Technology **40**, 93-99 (1999).

T. Mukaihara, N. Ohnoki, Y. Hayashi, N. Hatori, F. Koyama, and K. Iga, "Excess intensity noise originated from polarization fluctuation in vertical-cavity surface-emitting lasers," IEEE Photonics Technology Letters **7**, 1113-1115 (1995).

V. Nagali and R.K. Hanson, "Design of a diode-laser sensor to monitor water vapor in high-pressure combustion gases," Appl. Opt. **36**, 9518-9527 (1997).

K. Namjou, S. Cai, E.A. Whittaker, J. Faist, C. Gamchl, F. Capasso, D.L. Sivco, and A.Y. Cho, "Sensitive absorption spectroscopy with a room-temperature distributive-feedback quantum-cascade laser," Opt. Lett. **23**, 219-221 (1998).

G. J. Nebel, "Vehicle emissions," New York, Society of Automotive Engineers. Technical progress series Vol. 6, 269-273 (1964).

D.D. Nelson, M.S. Zahniser, J.B. McManus, C.E. Kolb, J.L. Jimenez, " A tunable diode laser system for the remote sensing of on-road vehicle emissions," Appl. Phys. B **67**, 433-441(1998).

Q.V. Nguyen, R.W. Dibble and T. Day, "High-resolution oxygen absorption spectrum obtained with an external-cavity continuously tunable diode laser," Optics Letters **19**, 2134-2136 (1994).

Q. V. Nguyen, B. L. Edgar, and R. W. Dibble, "Experimental and numerical comparison of extractive and *in situ* laser measurements of non-equilibrium carbon monoxide in lean-premixed natural gas combustion," Combustion and Flame **100**, 395-406 (1995).

X. Ouyang and P.L. Varghese, "Reliable and efficient program for fitting Galatry and Voigt profiles to spectral data on multiple lines," Appl. Opt. **28**, 1538-1545 (1989).

B.A. Paldus, T.G. Spence, R.N. Zare, J.Oomens, F.J.M. Harren, D.H. Parker, C. Gmachl, F. Cappasso, D.L. Sivco, J.N. Baillargeon, A.L. Hutchinson and A.Y. Cho, "Photoacoustic spectroscopy using quantum-cascade lasers," Opt. Lett. **24**, 178-180 (1999).

E.L. Petersen, R.W. Bates, D.F. Davidson, R.K. Hanson, "Laser absorption and infrared emission measurements in a high-pressure shock tube," AIAA 1997-0316, 35th Aerospace Sciences Meeting (Reno, 1997).

K.P. Petrov, L.Goldberg, W.K. Burns, R.F. Curl, and F.K. Tittel, "Detection of CO in air by diode-pumped 4.6-μm difference-frequency generation in quasi-phase-matched LiNbO3," Opt. Lett. **21**, 86-88(1996).

L. C. Philippe and R. K. Hanson, "Laser diode wavelength-modulation spectroscopy for simultaneous measurement of temperature, pressure, and velocity in shock-heated oxygen flows," Appl. Opt. **32**, 6090-6103 (1993).

W.R. Pierson, A.W. Gertler, N.F. Robinson, J.C. Sagebiel, B. Zielinska, G.A. Bishop, D.H. Stedman, R.B. Zweidinger, and W.D. Ray, "Real-world automotive emissions—summary of studies in the Fort McHenry and Tuscarora Mountain tunnels," Atmospheric Environment **30**, 2233-2256 (1996).

S. Pope, P.J. Wolf, and G.P. Perram, "Collision broadening of rotational transitions in the O_2 A band by molecular perturbers," Journal of quantitative spectroscopy & radiative transfer **64**, 363-377 (2000).

M. Razeghi, "Optoelectronic devices based on III-V compound semiconductors which have made a major scientific and technological impact in the past 20 years," IEEE J. on Selected Topics in Quantum Electronics **6**, 1344-1354 (2000).

E.C. Rea, Jr., S. Salimian and R.K. Hanson, "Rapid-tuning frequency-doubled ring dye laser for high-resolution absorption spectroscopy in shock-heated gases," Appl. Opt. **23**, 1691-1694 (1984).

J. Reid and D. Labrie, "Second-harmonic detection with tunable diode lasers—comparison of experiment and theory," Appl. Phys. B **26**, 203-210 (1981).

H. Riris, C. B. Carlisle, R. E. Warren, and D. E. Cooper, "Signal-to-noise enhancement in frequency-modulation spectrometers by digital signal processing," Opt. Lett. **19**, 144-146 (1994).

G. J. Rosasco, L. A. Rahn, W. S. Hurst, R. E. Palmer, S. M. Dohne, "Measurement and prediction of Raman Q-branch line self-broadening coefficients for CO from 400 to 1500 K," J. Chem. Phys. **90**, 4059-4068 (1989).

L. Rosenmann, J.M. Hartmann, M.Y. Perrin, and J. Taine, "Accurate calculated tabulations of IR and Raman CO_2 line broadening by CO_2, H_2O, N_2, O_2 in the 300-2400-K temperature range," Appl. Opt. **27**, 3902-3907 (1988).

L. S. Rothman, C. P. Rinsland, A. Goldman, S. T. Massie, D. P. Edwards, J.-M. Flaud, A. Perrin, C. Camy-Peyret, V. Dana, J.-Y. Mandin, J. Schroeder, A. Mccann, R. R. Gamache, R. B. Wattson, K. Yoshino, K. V. Chance, K. W. Jucks, L. R. Brown, V. Nemtchinov, and P. Varanasi, "The HITRAN molecular spectroscopic database and hawks (HITRAN atmospheric workstation): 1996 edition," J. Quant. Spectrosc. Radiat. Transfer **60**, 665-710 (1998).

S.T. Sanders, T.P. Jenkins, J.A. Baldwin, D.S Baer, and R.K. Hanson, "Diode laser absorption sensor for measurements in pulse detonation engines," AIAA 2000-0358, 38th Aerospace Sciences Conference, Reno, NV, 2000a.

S.T. Sanders, J.A. Baldwin, T.P. Jenkins, D.S. Baer, and R.K. Hanson, "Diode-laser sensor for monitoring multiple combustion parameters in pulse detonation engines," 28th International Symposium on Combustion, paper **4D04**, 2000b.

H.I. Schiff, S.D. Nadler, J. Pisano and G.I. Mackay, "Application of near infrared TDLAS systems to HF measurements in aluminum smelters," SPIE Proceedings **2824**, 198-204 (1996).

S. M. Schoenung and R. K. Hanson, "CO and temperature measurements in a flat flame by laser absorption spectroscopy and probe techniques," Combust. Sci. Technol. **24**, 227-237 (1981).

F. Schreier, "The Voigt and complex error function: a comparison of computational methods," J. Quant. Spectrosc. Radiat. Transfer **48**, 743-762 (1992),

J.M. Seitzman, R. Tamma, and B.T. Scully, "Broadband infrared sensor for active control of high pressure combustor," AIAA 1998-0401, 36th Aerospace Sciences Meeting, Reno (1998).

J. A. Silver, "Frequency-modulation spectroscopy for trace species detection: theory and comparison among experimental methods," Appl. Opt. **31**, 707-717 (1992).

J.A. Silver and D.J. Kane, "Diode laser measurements of concentration and temperature in microgravity combustion," Meas. Sci. Technol. **10**, 845-852 (1999).

A. Sjodin, M. Lenner, "On-road measurements of single vehicle pollutant emissions, speed and acceleration for large fleets of vehicles in different traffic environments," The Science of Total Environment, **169**, 157-165 (1995).

Sjodin, K. Andreasson, M. Wallin, M. Lenner and H. Wilhemsson, "Identification of high-emitting catalyst cars on the road by means of remote sensing," Int. J. of Vehicle Design **18**, 326-339 (1997).

R.V. Steele, "Review and forecast of the laser markets Part II: diode lasers," Laser Focus World, February (2001).

G. Steinle, H.D. Wolf, M. Popp, A. Yu. Egonov, G. Kristen, H. Riechert, "Novel monolithic VCSEL devices for datacom applications," 51st ECTC (2001).

R.D. Stephens and S.H. Cadle, "Remote sensing measurements of carbon monoxide emissions from on-road vehicles," J. Air Waste Manage. Assoc. **41**, 39-46 (1991).

R.D. Stephens, S.H. Cadle, and T.Z. Qian, "Analysis of remote sensing errors of omission, and commission under FTP conditions," J. Air Waste Manage. Assoc. **46**, 510-516 (1996).

F. Sugihwo, M.C. Larson, J.S. Harris, "Micromachined widely tunable vertical cavity laser diodes," J. of Microelectromechanical Systems **7**, 48-55 (1998).

B. L. Upschulte, D. M. Sonnenfroh, M. G. Allen, " Measurements of CO, CO_2, OH and H_2O in room-temperature and combustion gases by use of a broadly current-tuned multisection InGaAsP diode laser," Appl. Opt. **38**, 1506-1512 (1999).

U.S. EPA Office of Air & Radiation, "1997 national air quality: status and trends," (1998). Available on the U.S. EPA website: http://www.epa.gov/oar/aqtrnd97/brochure/co.html.

U.S. EPA Office of Mobile Sources, Remote Sensing: A Supplemental Tool for Vehicle Emission Control, available on the U.S. EPA website: http://www.epa.gov/reg3artd/vehic/15-remot.htm

U.S. Government, Code of Federal Regulations, 40CFR60, Office of the Federal Register, Washington, DC.

U.S. Government, Code of Federal Regulations, 40CFR264/266, Office of the Federal Register, Washington, DC.

U.S. Government, "Method 10: Determination of carbon monoxide emissions from stationary sources," Reference Methods promulgated under Code of Federal Regulations, 40CFR60, Office of the Federal Register, Washington, DC.

P. L. Varghese and R. K. Hanson, "Collision width measurements of CO in combustion gases using a tunable diode laser," J. Quant. Spectrosc. Radiat. Transfer **26**, 339-347 (1981 a).

P. L. Varghese and R. K. Hanson, "Room temperature measurements of collision widths of CO lines broadened by H_2O," J. Mol. Spectrosc, **88**, 234-235 (1981 b).

P.A. Walsh, J.C. Sagebiel, D.R. Lawson, K.T. Knapp, G.A. Bishop, "Comparison of auto emission measurement techniques," The Science of Total Environment, **189/190**, 175-180 (1996).

J. Wang, M. Maiorov, D.S. Baer, D.Z. Garbuzov, J.C. Connolly, and R.K. Hanson, "In situ combustion measurements of CO with diode-laser absorption near 2.3 μm," Appl. Opt. **39**, 5579-5589 (2000).

M. E. Webber, J. Wang, S. T. Sanders, D. S. Baer, R. K. Hanson, "*In situ* combustion measurements of CO, CO_2, H_2O and temperature using diode laser absorption sensors," accepted by Twenty-Eighth Symposium (International) on Combustion (2000).

V. Weldon, J. O'Gorman, J.J. Perez-Camacho, D. McDonald, J. Hegarty, J.C. Connolly, N.A. Morris, R.U. Martinelli, J.H. Abeles, "Laser diode based oxygen sensing: A comparison of VCSEL and DFB laser diodes emitting in the 762 nm region," Infrared Physics & Technology **38**, 325-329 (1997).

E.E. Whiting, "An empirical approximation to the Voigt profile," J. Quant. Spectrosc. Radiat. Transfer **8**, 1379-1384 (1968).

G.C. Wilson, D.M. Kuchta, J.D. Walker, and J.S. Smith, "Spatial hole burning and self-focusing in vertical-cavity surface-emitting laser diodes," Appl. Phys. Lett. **64**, 542-544 (1994).

J.M. Woodall, "III-V compounds and alloys: an update," Science **208**, 908-915(1980)

R.P. Wort, "Automatic boiler combustion control using excess oxygen measurements," Brown Boveri Review **64**, 420-429 (1977).

H.P. Zappe, M. Hess, M. Moser, R. Hovel, K. Gulden, H.-P. Gauggel, and F. Monti di Sopra, "Narrow-linewidth vertical-cavity surface-emitting lasers for oxygen detection," Applied Optics **39**, 2475-2479 (2000).

Y.-G. Zhao and J.G. McInerney, "Transverse-mode control of vertical-cavity surface-emitting lasers," IEEE Journal of Quantum Electronics **32**, 1950-1958 (1996).